Title
Quasi 2D Materials: Raman Nanometrology and Thermal Management Applications

Author
Shahil, Khan Mohammad Farhan

Publication Date
2012

UNIVERSITY OF CALIFORNIA
RIVERSIDE

Quasi 2D Materials: Raman Nanometrology and Thermal Management Applications

A Dissertation submitted in partial satisfaction
of the requirements for the degree of

Doctor of Philosophy

in

Electrical Engineering

by

Khan Mohammad Farhan Shahil

March 2012

Dissertation Committee:
- Dr. Alexander A. Balandin, Chairperson
- Dr. Roger Lake
- Dr. Elaine D. Haberer

The Dissertation of Khan Mohammad Farhan Shahil is approved:

Committee Chairperson

University of California, Riverside

Acknowledgements

I would first like to thank my advisor Dr. Alexander Balandin for his continuous guidance and encouragement in the course of my research. He has helped me grow professionally and has given me proper exposure to the academic and industrial research work in my field. He gave me freedom and opportunities to work on challenging research problems which helped me develop my original research ideas. His interactive guidance, high research standards and work ethics have been invaluable for the project. The distinguished lessons and experiences he has equipped me with will always stay with me throughout my future journey.

I would also thank Dr. Elaine D. Haberer and Dr. Roger Lake for taking the time to serve in my dissertation committee. I also thank them for numerous beneficial discussions that I had with them all along.

I thank MARCO Center on Functional Engineered Nano Architectonics (FENA), Office of Naval Research (ONR), Semiconductor Research Corporation (SRC) and Defense Advanced Research Project Agency (DARPA) for their support.

I would like to thank Dr. Andreas Kerber (GlobalFoundries), Dr. William McMahon (GlobalFoundries) and Dr. Tanya Nigam (GlobalFoundries) for guiding me during my internship at GlobalFoundries. I greatly benefited from the experiments on SRAM reliability.

I would also like to thank all the present and past group members for generating a research-friendly environment at the Nano Device Laboratory. A special thanks to Dr. Muhammad Rahman, Dr. Samia Subrina, Mr. Zahid Hossain, Ms. Jie Yu, Mr. Pradyumna Goli, Dr. Desalegne Teweldebrhan and Dr. Vivek Goyal for making my days at NDL pleasant and memorable. My times were also made memorable by all my friends and people at UC Riverside. I wish them all the best in life.

Last but not the least; I would like to thank my parents, sister, and in-laws for their continuous support. My parents have created the pedestal for me to stand here today. They have been my inspiration and guiding star. And lastly, to my dearest and loving wife, Sonia for her unconditional support and encourage, while pursuing her PhD in Electrical Engineering. This work would not have been possible without the steadfast support and encouragement of therm. This dissertation is dedicated to them.

On top of everything, all praise goes to the Almighty Allah; the most Gracious, the most merciful for blessing me with all good things I have and showing me the enlightened path.

The text of this dissertation, in part or in full, is a reprint of the material as it appears in the following journals:

- K. M. F. Shahil and A. A. Balandin, “Graphene – Multilayer Graphene Nanocomposites as the Highly Efficient Thermal Interface Materials”, *Nano Letters,* DOI: 10.1021/nl203906r (2012). © American Chemical Society, 2012.

- K. M. F. Shahil, M. Z. Hossain, V. Goyal and A. A. Balandin, "Micro-Raman Spectroscopy of Mechanically Exfoliated Few-Quintuple Layers of Bi_2Te_3, Bi_2Se_3 and Sb_2Te_3 Materials*" Journal of Applied Physics (JAP),* (2012). ©American Institute of Physics, 2012.

- K. M. F. Shahil, M. Z. Hossain, D. Teweldebrhan and A. A. Balandin, "Crystal Symmetry Breaking in Few-Quintuple Bi_2Te_3 Films: Applications in Nanometrology of Topological Insulators" *Applied Physics let. (APL)* 96, 16, (2010). ©American Institute of Physics, 2010.

- K. M. F. Shahil, V. Goyal and A. A. Balandin, "Thermal Properties of Graphene: Applications in Thermal Interface Materials", *ECS Transactions (ECST)* **35** (3) 193-199 (2011). © The Electrochemical Society, 2011.

To my parents, sister
and
my wife

ABSTRACT OF THE DISSERTATION

Quasi 2D Materials: Raman Nanometrology and Thermal Management Applications

by

Khan Mohammad Farhan Shahil

Doctor of Philosophy, Graduate Program in Electrical Engineering
University of California, Riverside, March 2012
Professor Alexander A. Balandin, Chairperson

Quasi two-dimensional (2D) materials obtained by the "graphene-like" exfoliation attracted tremendous attention. Such materials revealed unique electronic, thermal and optical properties, which can be potentially used in electronics, thermal management and energy conversion. This dissertation research addresses two separate but synergetic problems: (i) preparation and optical characterization of quasi-2D films of the bismuth-telluride (Bi_2Te_3) family of materials, which demonstrate both thermoelectric and topological insulator properties; and (ii) investigation of thermal properties of composite materials prepared with graphene and few-layer graphene (FLG). The first part of dissertation reports properties of the exfoliated few-quintuple layers of Bi_2Te_3, Bi_2Se_3 and Sb_2Te_3. Both non-resonant and resonant Raman scattering spectra have been investigated. It was found that the crystal symmetry breaking in few-quintuple films results in

appearance of A_{1u}-symmetry Raman peaks, which are not active in the bulk crystals. The scattering spectra measured under the 633-nm wavelength excitation reveals a number of resonant features, which could be used for analysis of the electronic and phonon processes in these materials. The obtained results help to understand the physical mechanisms of Raman scattering in the few-quintuple-thick films and can be used for nanometrology of topological insulator films on various substrates. The second part of the dissertation is dedicated to investigation of properties of composite materials prepared with graphene and FLG. It was found that the optimized mixture of graphene and multilayer graphene – produced by the high-yield inexpensive liquid-phase-exfoliation technique – can lead to an extremely strong enhancement of the cross-plane thermal conductivity K of the composite. The “laser flash” measurements revealed a record-high enhancement of K by 2300 % in the graphene-based polymer at the filler loading fraction f =10 vol. %. It was determined that the relatively high concentration of the single-layer and bilayer graphene flakes (~10-15%) present simultaneously with the thicker multilayers of large lateral size (~ 1 μm) were essential for the observed unusual K enhancement. Our modeling results suggest that graphene – multilayer graphene nanocomposite used as the thermal interface material outperforms those with carbon nanotubes or metal nanoparticles owing to graphene’s aspect ratio and lower Kapitza resistance at the graphene - matrix interface.

Table of Contents

3 Nanostructures: Quasi 2D Materials

4 Experimental Methodology: Raman Nanometrology

5 Results and Discussions: Raman Nanometrology

6 Thermal Properties of Graphene: Future Paradigm for Thermal Interface Material

7 Experimental methodology: Liquid Phase Exfoliation (LPE) method and LASER flash measurement

8 Results and Discussions: Graphene Based Thermal Interface Materials

9 Conclusions

List of Figures

List of Tables

Chapter 1

Introduction

1.1 Motivation

The invention of transistor and the consequent invention of integrated circuits (ICs) opened up an unparalleled scientific and technological growth at the beginning of 20th century. It was first demonstrated by John Bardeen, Walter Houser Brattain, and William Bradford Shockley, Bell Labs in 1947. In acknowledgement of this accomplishment, Shockley, Bardeen, and Brattain were jointly awarded the 1956 Nobel Prize in Physics for their discovery of the transistor effect [1]. The first silicon transistor was produced by Texas Instruments in 1954 [2] followed by first demonstration of Metal Oxide Semiconductor (MOS) transistor by Kahng and Atalla at Bell Labs in 1960 [3]. Today highly automated semiconductor processing methods for silicon field effect transistors (FET) has helped revolutionize the electronic industry to unprecedented levels both technically and economically. The roadmap of the semiconductor industry has continuously projected better performance by shrinking transistor gate length, increase in number of transistors per wafer, wafer size growth, and reduction in defect density. A long-term trend in the history of computing hardware, proposed by Gordon E. Moore, predicts doubling of transistor counts in every two years. Especially in the last decade, the aggressive downscaling of the device size has yielded enormous gain in terms of computing power, portability and device density. Figure 1.1 shows number of transistors on a chip from year 1970 to 2012.

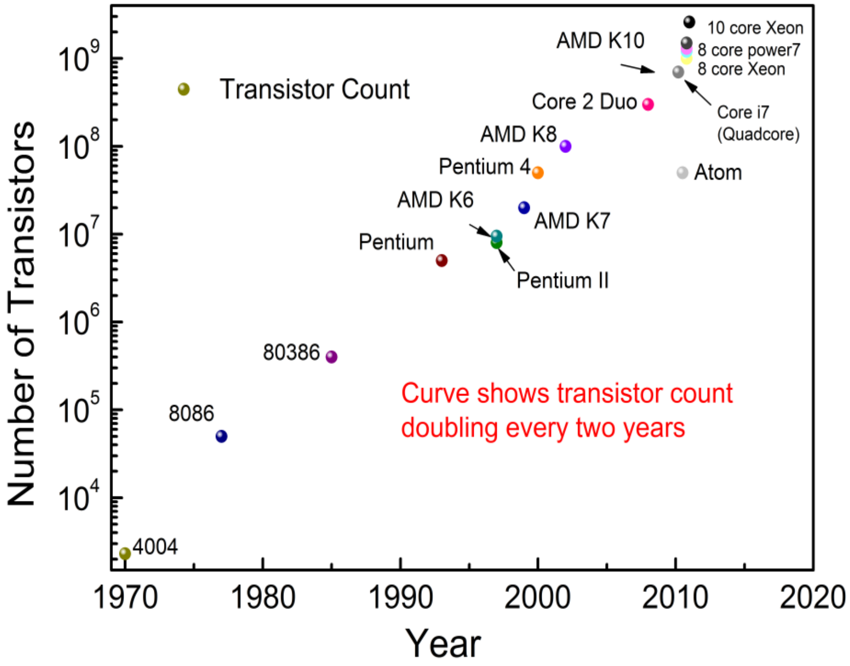

Figure 1.1: Scaling trend showing number of transistors on a chip between the years 1970 and 2011. Data is from publications by AMD and Intel Corporation.

In addition with the enormous gain in terms of computing power, the “aggressive downscaling” has been associated with some other major challenges related to energy consumption, dissipation, and waste. Specifically power dissipation issues have recently become one of its greatest challenges for integrated electronics. Power dissipation limits the performance of electronics from handheld devices (~10^{-3} W) to massive data centers (~10^{9} W), all primarily based on silicon micro/nanotechnology [4]. Such challenges are also prominent at the individual micro- processor (CPU) level, where increasing operating frequency beyond a few GHz recently stopped when typical dissipated power reached 100 W/cm^2 (see Fig. 1.2), which is roughly equivalent to that of nuclear reactor. By comparison, the power density on the surface of the sun is approximately 6000 W/cm^2 [5].

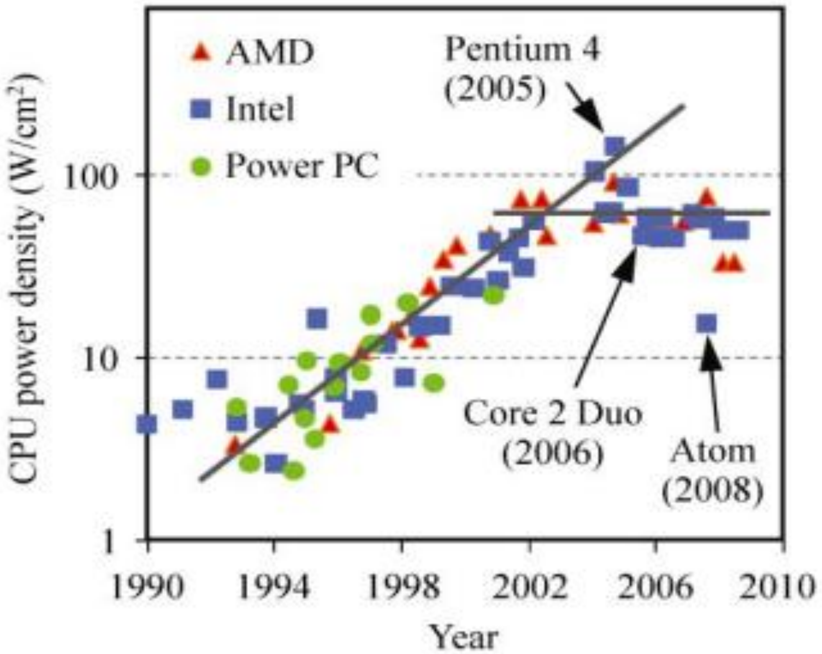

Figure 1.2: Near-exponential increase of CPU power density in recent decades has flattened with the introduction of multi-core CPUs (solid lines show approximate trends), Reprinted with permission from Ref. [4], © 2006 Springer.

Figure 1.2 shows an exponential trend of the increasing power densities. This high power density increases various thermal challenges that have negative impacts in areas from massive database servers to new applications like wearable devices, medical instrumentation, or portable electronics.

Moreover variations in the activity of the transistors for different functional units create high heat flux up to 1000 W/cm^2 i.e., “hot spots” only a couple of hundred micrometers in diameter that can be 10ºC–40ºC hotter than the rest of the chip [6]. Most of the conventional cooling techniques can be used to cool the whole chip. Since thermal design requirements are mostly driven by peak temperatures, reducing or eliminating hot spots could alleviate the design requirements for the whole package.

At this point, it is worthwhile to mention that all these thermal management issues must be taken into account from material level rather than design level such as putting big cooling fan or increasing ventilation. In order to increase heat dissipation, one effective way could be to use materials having high thermal conductivity. In nanoscale regime, thermal conductivity could be affected by random thermal vibration of atoms in material. When one area of the sample is hot, the interaction between neighboring atoms causes the random vibrations to propagate in the material. In order to analyze the random thermal vibrations of atoms in a solid, research on eigen-modes of the collective vibrations (i.e., phonons) could be helpful. It is more intuitive to explain how different phonons are transported. Acoustic and optical phonons refer to the case where neighboring atoms oscillate in phase or out of phase, respectively. In the latter case, an atomic dipole is formed that could interact with photons, thus the name optical phonon. Electron transport in devices often generates optical phonons. On the other hand, heat in semiconductor materials is mostly carried by acoustic phonons. So efficient heat transport depends upon the transmissibility, reflectivity and scattering of phonons through the interface which is governed by the phonon dispersion mismatch, difference in phonon density of states of the two materials across the interface.

When the device feature size is comparable to the phonon mean free path, several technological reasons are responsible for lowering the thermal conductivity which elevates heat dissipation problem. For example, the transistor gate length is 25 nm in current technology node (22 nm). Also there are structures which are already much smaller than MFP. The SOI layer is in the order of 10-40nm, the gate oxide thickness is ~1 nm and super lattices size is 1.5nm. On the other hand, MPF in bulk crystalline Si is 43 nm - 300 nm [7] at RT. For such a low feature size, in addition to the Umklapp 3-phonon scattering and Rayleigh scattering; phonon boundary/rough interface scattering emerges as a dominant phonon scattering mechanism. The phonons get scattered from the rough boundaries and interfaces and this phonon scattering contributes to thermal resistance. Also due to the spatial confinement of phonons in low-dimensional structures, such as thin films or nanowires, embedded within materials having different elastic properties, acoustic phonon dispersion gets modified which splits the acoustic phonon branches into quasi-optic phonon branches. The group velocity of the phonon at such frequencies is much smaller than of those in bulk branches. All these additional phonon scattering terms reduce thermal conductivity as much as 50 % than that of bulk value and result in a bottleneck for heat removal. So phonon engineering could be an efficient way to improve material's intrinsic thermal conductivity consequently maintaining a uniform heat transport.

Furthermore the localized regions of high power densities (i.e., hotspots) are outcome of intense electron-phonon coupling due to the hot-electrons in non-equilibrium with the lattice. The hot-electrons undergoes deformation potential scattering. The elastic scattering process results in the heating of lattice. So it is obvious that with an improvement in material properties, hot spots of tens of micrometers in diameter with heat fluxes in excess of 1000 W/cm^2 could be cooled down by 20ºC–30ºC [4]. Heat and current spreading in the three-dimensional electrode configuration could be another means to remove high-power hot spots in IC chips.

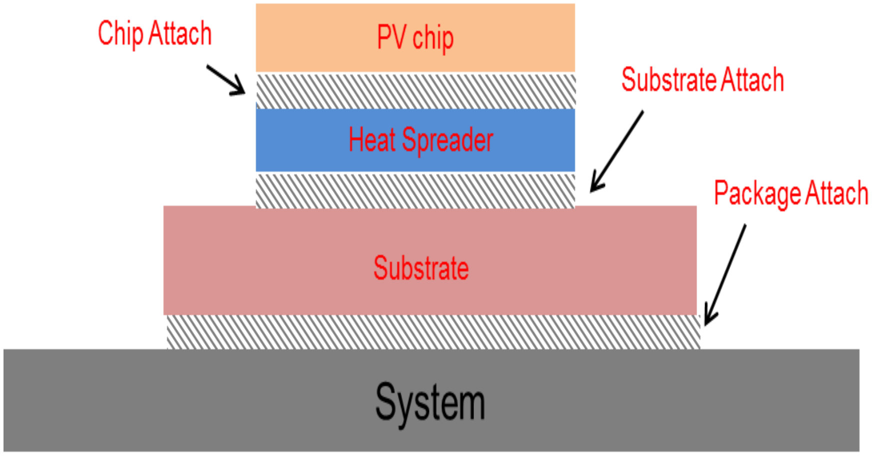

Figure 1.3: Schematic diagram of a Photovoltaic (PV) cell packaging assembly stack up.

The needs for efficient thermal management are not limited to electronics; it has become an important issue for other energy conversion devices such as solar cells (e.g. photovoltaics) and optoelectronics (e.g. LEDs)]. One of the key power generation technologies in the current “green” revolution is solar photovoltaic cell (PV).

This unit directly converts solar energy into useful amounts of electrical energy in an increasingly economically-efficient manner. A PV cell can be constructed from various materials including crystalline silicon or conjugated polymers [8, 9]. Figure 1.3 shows a schematic of typical PV cell chip sitting on material that acts as a heat spreader and/or an interface that absorbs mechanical stresses due to mismatched coefficients of thermal expansion between the chip and the substrate. The chip through the substrate is considered a package. Current technology produces solar cell that are approximately 15% efficient in converting absorbed light into electricity [10]. As the SPVC cell absorbs light from the sun and converts it into electricity it also absorbs heat that results in a temperature rise. About 70% of the solar energy is converted to the heat. The heat must be efficiently removed from the cell to prevent degradation of performance or damage of the cell. The effect of temperature on power produced degrades linearly at 0.23 W/°C from 25°C to 70°C for a mono-crystalline silicon PV [8]. This corresponds to a 20% reduction in produced power due to thermal build up. Other studies have identified a 0.5% efficiency loss per °C increase in cell temperature [11] Since the highest temperatures of solar PV panels recorded are about 70 º C [12], this efficiency loss can be very noticeable. A lowering of cell temperature by 15 ºC at 1sun will boost 6% in output power [10]. For this reason, the average efficiency of a PV array was actually higher in the winter months due to lower temperatures but total electrical power produced remained higher in the summer due to longer duration of solar irradiance [12]. One method of cooling the PV cell is to use a heat spreader to spread the heat generated in the cell and then either passively or actively cool the cell by a heat sink or an exchanger, respectively. This suggests that thermal management of the PV cell is critical to the performance of the semiconductor and assembly particularly when the assembly is used in areas with high ambient temperatures. Further improvements in PV cell performance and reliability will be greatly influenced by thermal considerations. And having a way of validating thermal management designs will play a big part in future PV cell technology advances.

Hence efficient heat transport stimulates the search for more efficient thermal interface materials (TIMs) which are considered as fundamental components for thermal management applications. The function of TIMs is to fill the voids and grooves created by imperfect surface finish of two mating surfaces, thus forcing air out and improving surface contact and the conduction pathway across the interface The commonly used conventional TIMs are based on polymers or greases filled with the thermally conductive particles such as silver or silica, which require high volume fractions of the filler material (up to ~70%) to achieve thermal conductivity of about 1 – 5 W/mK of the composite [13-16]. The needs for improved TIMs in electronic chips and high-power density photonics motivated research of a possible use of carbon materials as fillers for TIMs. A number of TIMs containing carbon based allotropes such as graphite, carbon black, synthetic diamond, fullerenes, carbon nanotubes (CNTs), graphite nanoplatelets (GNPs) and graphene oxide (GO) nanoparticles (GONs) have been examined [13-18]. Among the carbon allotropies, CNTs have excellent intrinsic thermal conductivity comparable to that of graphene. At the same time, their use in TIMs faced a number of difficulties. The cost of CNTs continues to be too high for industrial applications. It is difficult to achieve the high filling fractions of CNTs and alignment, which would allow one to fully utilize their thermal conductivity. The large thermal boundary resistance (TBR) of CNTs also presents a problem for TIMs. Grephene [19] benefits include extremely high intrinsic thermal conductivity [20-22], planar geometry, stronger coupling to the matrix materials (i.e. lower TBR) and lower cost. All these exotic properties make graphene as a prospective candidate of next generation thermal interface materials.

Another promising approach has recently been to look at incorporating materials with low dimensionalities that exhibit extraordinary properties into the chip design to help improve the device ability to perform effectively such as less scatting, high mobility, less heat generation. Today nanotechnology, in which dimensions are measured in billionths of a meter, are the foundations for a fast-growing approach to energy saving and thermal management. Research in this topic is opening new fields of development and applications in different academic disciplines such as materials science (nanostructured materials), medicine, biotechnology, manufacturing, computing, information technology and communications. With nanotechnology, a large set of materials and improved products rely on the change in the physical properties when the feature sizes are shrunk. Nanoparticles, for example, take advantage of their dramatically increased surface area to volume ratio. Their optical properties, e.g. fluorescence, become a function of the particle diameter. When brought into a bulk material, nanoparticles can strongly influence the mechanical properties of the material, like stiffness or elasticity. So nanostructured materials will enable a weight reduction accompanied by an increase in stability and an improved functionality with lower power consumption.

So for application of nanotechnology into various thermal management and device applications researchers always kept on searching of new nanostructured materials. New material brings new opportunities to reexamine the old problem as the new one. The same chemical compound can exhibit dramatically different electrical, optical and thermal properties depending on whether it is arranged in a 0D, 1D, 2D or 3D crystal structure. Quasi-0D (e.g., cage molecules), quasi-1D (e.g., nanotubes, nanowires) and of course, 3D crystalline objects have already been studied well both theoretically and experimentally. The main applications of 2D materials are in electronic semiconductor devices and optical coatings. Heat conduction in single crystal semiconducting and superconducting films is of great interest. Also for 2D materials, interfacial effects attribute to the difference in bulk and film thermal properties.

However two dimensional (2D) materials is conspicuously absent among experimentally known crystals. There are some layered materials like graphite, bismuth telluride, bismuth selenide, $NbSe_2$, MoS_2 have strong in-plane bonds but weak van der Walls coupling force between the layers. Because of this layered structure and weak coupling forces among the layers, it has long been tempting to try splitting such materials into individual atomic planes, although it remained unclear whether free-standing atomic layers could exist in principle as thin films become thermodynamically unstable (decompose or segregate) below a certain thickness. Finally The mechanical exfoliation of graphene by Novoselov *et al.* [19] and discovery of its unique thermal [20-22], electrical [23-24] and optical [25] properties stimulated major interest to the 2D materials. These are among the thinnest objects one can even imagine. Scattering in this material is low and thus allows high mobility and observation of quantum hall effect (QHE). The unique band structure (linear dispersion curve) near the Dirac point of graphene has given this old effect a new twist. It was recently demonstrated that, Graphene like mechanical exfoliation can also isolate Bi_2Te_3/Bi_2Se_3 crystals into its building blocks Te-Bi-Te-Bi-Te atomic five folds with the thickness of ~1 nm [26-29]. 2D bismuth telluride is predicted to have surface states while insulating gap at the bulk. Successful application of these quasi 2D materials depends on characterization technique and accurate process of determining atomic planes and their quality.

Research in the field of quasi 2D materials is still in its infancy and this thesis examines only the very beginnings of what will likely to be an important material of the future nanoelectronic applications.

1.2 Overview

This dissertation aims to develop a novel microscopic picture of phonon engineered quasi 2D materials. It studies the characterization and further applications of a set new nanostructured quasi 2D materials. The dissertation discusses a novel nenometrology/characterization technique of quasi 2D Bismuth telluride types of materials using Raman spectroscopy. This study further extends detail analysis of various new interesting features of these materials. Next it discusses an important possible application of the leading 2D materials i.e., graphene in thermal management solutions.

The manuscript begins with the discussion of phonon engineering in nanostructures and new prospective quasi 2D nanostructured materials in chapter 2 and chapter 3 respectively. Chapter 4 discusses the experimental methodology. It describes the theory related to the experimental technique used, the experimental setup and the sample preparation procedure for conducting measurements. In chapter 5, experimental results of Raman spectroscopy of a set of quasi 2D bismuth telluride based materials are presented. Theoretical explanations in support of our experimental findings are provided as well. Chapter 6 describes the thermal property of Graphene followed by a brief discussion on thermal interface materials. In chapter 7, experimental methodology of preparation of thermal interface material with Graphene nanostructured materials is presented. The detailed experimental and theoretical results on thermal conductivity enhancement with Graphene based TIMs are presented in chapter 8. Finally, chapter 9 summarizes the concluding remarks of this dissertation.

References

[1] *"The Nobel Prize in Physics 1956"*. Nobelprize.org. 15 Jan 2012, http://www.nobelprize.org/nobel_prizes/physics/laureates/1956/

[2] J. Chelikowski, *Introduction: Silicon in all its Forms*, Silicon: evolution and future of a technology (Editors: P. Siffert, E. F. Krimmel), p.1, Springer (2004).

[3] W. Heywang, K. H. Zaininger, *Silicon: The Semiconductor Material*, Silicon: evolution and future of a technology (Editors: P. Siffert, E. F. Krimmel), p.36, Springer (2004).

[4] E. Pop, *Nano Research* **3**, 147-169 (2010).

[5] E. Pop, S. Sinha and K. E. Goodson, *Proc. IEEE*, **94** 1587–1601 (2006).

[6] A. Shakouri, *Proceedings of the IEEE*, **94**, 8 (2006).

[7] D. M. Gruen, *Annu. Rev. Mater. Sci*. **29**, 211, (1999).

[8] E. Van Dyk, E. Meyer, A. Leitch and B. Scott, *South African Journal of Science* **96**(4), 198-200 (2000).

[9] S. Schuller, P. Schilinsky, J. Hauch and C. Brabec, *Applied Physics A* **79**, 37-40 (2004).

[10] X. C. Tong, *Advanced Materials for Thermal Management of Electronic Packaging*, 1st edition, Springer Series in Advanced Microelectronics, vol-30 (2011).

[11] B.J. Brinkworth and M. Sandberg. *Solar Energy* **80**, 89-103, (2006).

[12] G. Notton, C. Cristofari, M. Mattei and P. Poggi, *Applied Thermal Engineering* **25**, 2854-2877(2005).

[13] J. Liu, B. Michel, M. Rencz, C. Tantolin, C. Sarno, R. Miessner, K. V. Schuett, X. Tang, S. Demoustier, A. Ziaei, *EDA Publishing Therminic*, Rome, Italy, 156, Sep. (2008).

[14] F. Sarvar, D. C. Whalley and P. P. Conway, *Proceeds. Electronics System Integration Technology Conference* (IEEE 1-4244-0553), **2**, 1292-1302 (2006).

[15] R. S. Prasher, J.-Y. Chang, I. Sauciuc, S. Narasimhan, D. Chau, G. Chrysler, A. Myers, S. Prstic and C. Hu, *Intel Technology Journal*, **9**, 285 – 296 (2005).

[16] J. Felba, *Thermally conductive nanocomposites, in Nano-Bio-Electronic, Photonic and MEMS Packaging* (Springer Science, 2010; DOI 10.1007/978), Editors C.P. Wong, K.-S. Moon and Y. Li, 277 – 314 (2010).

[17] P. Kim, L. Shi, A. Majumdar, and P. L. McEuen, *Phys. Rev. Lett.* **87**, 215502, 4 (2001).

[18] E. Pop, D. Mann, Q. Wang, K. Goodson and H. Dai, *Nano Lett.* **6**, 1, 96-100 (2006).

[19] K. S. Novoselov, A. K. Geim, S. V. Morozov, D. Jiang, Y. Zhang,S.V. Dubonos, I. V. Grigorieva and A. A. Firsov, *Science* **306**, 666 (2004).

[20] A. A. Balandin, S. Ghosh, W. Bao, I. Calizo, D. Teweldebrhan, F. Miao and C. N. Lau, *Nano Letters* **8**, 902 (2008).

[21] S. Ghosh, I. Calizo, D. Teweldebrhan, E. P. Pokatilov, D. Nika, A. Balandin, W. Bao, F. Miao, and C. N. Lau, *Appl. Phys. Lett.* **92**, 151911(2008).

[22] D.L. Nika, S. Ghosh, E.P. Pokatilov, A.A. Balandin, *Appl. Phys. Lett.*, **94**, 203103 (2009); D.L. Nika, E. P. Pokatilov, A. S. Askerov and A. A. Balandin, *Physical Review B* **79**, 155413 (2009).

[23] K.S. Novoselov, A.K. Geim, S.V. Morozov, D. Jiang, M.I. Katsnelson, I.V. Grigorieva, S.V. Dubonos and A. A. Firsov, *Nature* **438**, 197-200 (2005).

[24] Y. Zhang, J. W. Tan, H. L. Stormer and P. Kim, *Nature* **438**, 201-204 (2005).

[25] R. R. Nair, P. Blake, A. N. Grigorenko, K. S. Novoselov, T.J. Booth, T. Stauber, N. M.R. Peres, and A. K. Geim, *Science* **320**, 1308 (2008).

[26] D. Teweldebrhan, V. Goyal and A. A. Balandin, Nano Lett. 10, 1209 (2010). D. Teweldebrhan, V. Goyal, M. Rahman and A. A. Balandin, *Appl. Phys. Lett.* **96**, 053107 (2010).

[27] K. M. F. Shahil, M. Z. Hossain, D. Teweldebrhan, and A. A. Balandin, *Appl.Phys. Lett.* **96**, 153103 (2010).

[28] M. Z. Hossain, S. L. Rumyantsev, D. Teweldebrhan, K. M. F. Shahil, M. Shur, A. A. Balandin, *Physica Status Solidi (A), Applications and Materials* **208**, 1, 144-146 (2011).

[29] M. Z. Hossain, S. L. Rumyantsev, K. M. F. Shahil, D. Teweldebrhan, M. Shur, A. A. Balandin, *ACS Nano* **5** (4), 2657-2663 (2011).

Chapter 2

Phonon Engineering in Nanostructures and Raman Spectroscopy

2.1 Introduction

Phonons are quantized modes of vibration occurring in a rigid crystal lattice, such as the atomic lattice of a solid. The physics of phonon transport at small length scales is increasingly important for basic research in nano-electronics, optoelectronics, nano mechanics, and thermoelectric. Such understanding is also critical for larger-scale device technologies that are pushing the limits of thermal engineering. The knowledge of engineering phonon dispersion in nanostructures has the potential to be as powerful as the idea of the band-gap engineering for electrons, which is now utilized in a variety of devices.

2.2 Background of Phonon Engineering

The lattice contribution to the heat capacity of solids approaches to zero as temperature approaches zero [1]. This explains that the lattice vibrations are quantized. A quantum of this vibrational energy is the elementary excitation called “phonon” whose occupation number obeys Bose-Einstein statistics [2]; in analogy with the photon, which is a quantum of energy in an electromagnetic wave. The displacement of one or more atoms from their equilibrium positions will give rise to a set of vibration waves propagating through the lattice. The amplitude of the wave is given by the displacement of the atoms from their equilibrium positions. If the atom is displaced from its equilibrium position, it oscillates about its equilibrium position because of the bonding forces between the atoms which tend to push it back. Since the lattice waves propagate in a periodic medium they have properties much like those of Bloch waves. There are six types of elastic waves – three acoustic modes, and three optical modes. Acoustic modes are like sound waves as adjacent atoms are displaced in the same direction. Of the three acoustic modes, one is longitudinal (LA) in which atoms are displaced in the direction of wave propagation and other two are transverse (TA) in which atoms are displaced in transverse direction. In optical modes, the adjacent atoms are displaced out of phase. When electrons are scattered by optical phonons and remain within same valley, only small wave vectors are involved and the dispersion can be approximated as:

$$\omega(\beta) = \omega_0 , \tag{2.1}$$

where ω_0 is a constant.

Optical phonons strongly influence optical properties of semiconductors while acoustic phonons are dominant heat carriers in insulators and technologically important semiconductors.

Inelastic scattering of X-rays and neurons by the crystals, accompanied with energy and momentum changes corresponding to the emission or absorption of one or more phonons. Phonon dispersion curves in crystals along high-symmetry directions of the Brillouin zone can be measured quite precisely by inelastic neutron scattering and more recently by high resolution inelastic x-ray scattering [3].

Phonons manifest themselves in all properties of materials; phonons limit electrical conductivity; spatial confinement of phonons in nanostructures can strongly affect the phonon spectrum and modify phonon properties such as phonon group velocity, polarization, density of states and electron - phonon interaction. Thus, nanostructures offer a new way of controlling phonon transport and electron - phonon interaction via tuning phonon dispersion relation, i.e. phonon engineering. Phonon interaction modes can be emphasized or attenuated by modifying the geometry, materials, and temperature. For example, thermal conductivity in bulk materials at room temperature is dominated by phonon-phonon and phonon-impurity interactions. As structures shrink to the nanoscale, confinement effects can change the dispersion relation that dictates available phonon modes [4]. Introducing material interfaces can also drastically affect phonon transport due to effects stemming from mismatched dispersion relations and the atomic structure of the interfaces [5]. As for light, periodic structures have been shown to introduce phonon band gaps, or forbidden frequencies, as well as the ability to redirect low-frequency surface phonons in a low-loss fashion. So the study of phonon transport in nanoscale structures is important for understanding and using nanoscale and nanostructured materials in diverse applications.

2.3 Raman Spectroscopy: Literature Review

2.3.1 Historical Background and Theoretical Formalism

Raman spectroscopy is a spectroscopic technique used to study vibrational, rotational, and other low-frequency modes in a system. It is based on the inelastic scattering of light by elementary excitations, usually from a laser in the visible, near infrared, or near ultraviolet range. The laser light interacts with molecular vibrations, phonons or other excitations in the system, resulting in the energy of the laser photons being shifted up or down. The shift in energy gives information about the vibrational modes in the system.

Raman Spectroscopy is an effective and non-destructive technique for characterizing semiconductors in a variety of forms such as device, bulk, thin film, or nanostructure. It is relatively fast, requires no sample preparation, and can measure very small samples. Although observed independently by Landsberg and Mandelstam from C. V. Raman [6] in 1928, Raman was credited with and eventually awarded the Nobel Prize in Physics in 1930 for discovering the Raman Effect. He found that a photon from incident light was annihilated while, simultaneously, a scattered photon is created. Raman scattering occurs because of an interaction between incident light and a material which leads to the annihilation or creation of a phonon. In crystals, atoms vibrate about their equilibrium positions affecting energy transport in the material. Because of these lattice vibrations, quantized lattice waves propagate in the crystal. The lattice loses or gains energy $\hbar\omega$ where $\hbar$ is Planck’s constant and ω is the characteristic phonon frequency. Because the lattice is losing or gaining energy, there will be a corresponding increase or decrease in the frequency ω_s of scattered photon, $\omega_s = \omega_i \pm \omega$. If the frequency of the scattered photon is less than the frequency of the incident photon, a quantum of energy is added to the sample. This is referred to as a Stokes process. If the frequency of the scattered photon is greater than the frequency of the laser’s photon, a phonon is annihilated from the sample and it is called an anti-Stokes process.

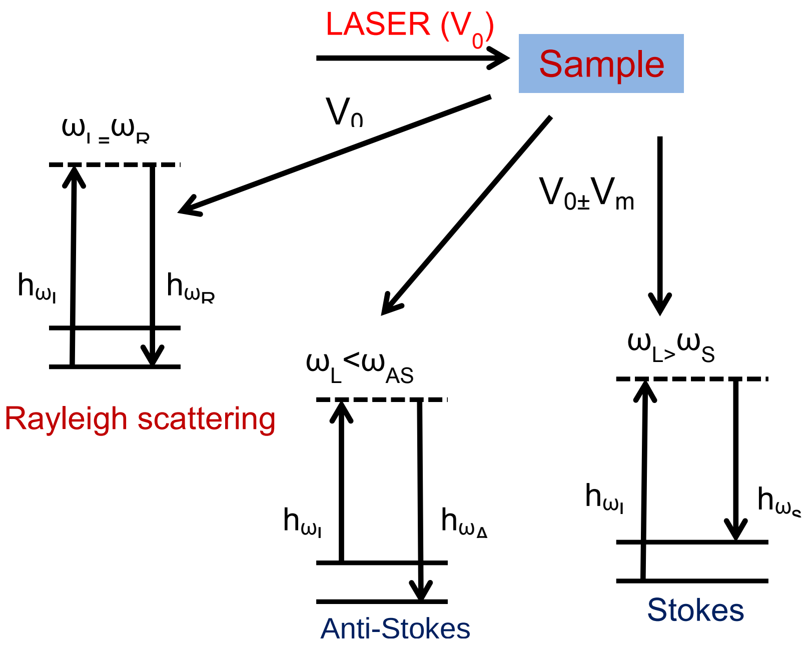

Figure 2.1: Schematic diagram showing Rayleigh, Stokes and anti-stokes scattering processes.

Rayleigh scattering occurs when the incident photon and the scattered photon are the same frequency. This relationship between Rayleigh, Stokes, and anti-Stokes process is illustrated in Figure 2.1.

A Stokes process can also be thought of as the photon shifting to a longer wavelength (lower energy) and an anti-Stokes process as shifting to a shorter wavelength (higher energy). In any case, the incident photon excites an electron into a higher virtual energy level followed by the electron transitioning back down to a lower vibrational energy level (Stokes) or to the ground state (anti-Stokes) emitting a photon. At thermal equilibrium, the intensity of the anti-Stokes peak is heavily temperature dependent because an anti-Stokes process only arises when the medium is not in the ground state. From the Boltzmann distribution, we know that the excited state has fewer electrons than the ground state. Therefore, the anti-Stokes spectrum can provide a means of monitoring sample temperature, as increased temperature provides additional energy in which to excite the electron into a higher energy. In addition to temperature monitoring, Raman spectroscopy can be used to assess crystal quality, alloy composition, carrier concentration and scattering time, ion-damage and annealing effects, and strain in semiconductors. Analogous to its electronic counterpart, the dispersion relation for phonons relates vibrational frequency (or energy), ω (or $\hbar\omega$), to the wave vector q which has values corresponding to the Brillouin zone (BZ). Therefore the wave vector's maximum value is $\frac{\pi}{a}$ where a the material's lattice is constant. For a lattice constant of ~3°A, a typical value for wave vector can be 10^{8} cm^{-1}. A phonon mode is represented by a point on a dispersion curve while the branches represent the various polarizations.

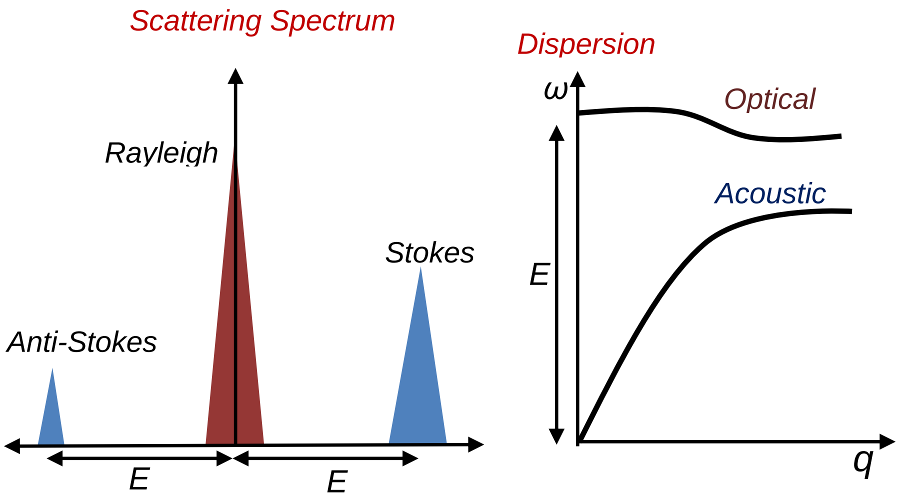

Figure 2.2: Relation of a Raman spectrum to phonon dispersion.

Photon wave vectors can be calculated $q_{photon} = 2\pi nk$, where n is the refractive index and k is the wave number. Since the wave vectors of photons are small, on the order of 10^5 cm^{-1}, compared to the size of the BZ, on the order of 10^8 cm^{-1}, Raman spectroscopy data of bulk crystalline materials gives the frequency for the phonons close to q = 0 (BZ center) on the phonon dispersion curve. Therefore each band in a Raman spectrum represents the BZ center energy of an optical phonon branch in the dispersion relation as shown in Fig. 2.2. On the other hand, in low-dimensional structures this q = 0 Raman selection rule is relaxed and Raman scattering away from the BZ center is allowed.

A Raman spectrum consists of a plot of intensity (count of photons) versus Raman shift (cm^{-1}). The Raman shift represents the frequency (or energy) difference between the incident photon and the scattered photon. Peaks in the Raman spectra arise due to inelastic scattering of photons, giving us information on the vibrational modes of the atoms in the unit cell i.e. BZ center optical phonon modes. Although optical phonons typically have a small group velocity they can scatter with acoustic phonons particularly at high temperatures and decrease thermal conductivity. The optical phonons also affect a material's electrical conductivity and optical characteristics. In nanostructures, the phonon means free path can be larger than the characteristic length giving rise to boundary scattering.

Bands appear in the Raman spectrum if vibrational modes of the atom induce a net change in its polarizability which is a measure of how easily an electrical charge can be displaced in the atom. Loosely held electrons will produce a larger change in polarizability resulting in a relatively intense Raman band. It results from the fact that when a sinusoidal electromagnetic field (light) falls on a material, there is an induced sinusoidal polarization. With the material at a finite temperature, the thermally excited atomic displacements associated with phonons will cause the material's electric susceptibility to oscillate. The resulting induced polarization vector will have two sinusoidal components representing the Stokes and anti-Stokes scattered light. The time-averaged power given off by the induced polarization vector is used to calculate the intensity of the Raman scattered light.

The details of the derivation for the expression for Raman scattered intensity are quite complex and this relation is simply stated for Stokes scattered light as [3]

$$I_s \infty \left| e_1 \cdot \left(\frac{\delta \chi}{\delta Q} \right)_0 Q(\omega_0) . e_s \right|^2 \tag{2.2}$$

where e_s is the polarization of the scattered radiation, Q is the vibration amplitude, and ω is the plane wave frequency. The Raman intensity as function of the incoming photon frequency is given by [7]

$$I_s(\omega) \infty \left| \omega_s^4 \varepsilon_s T \varepsilon_i \right| \sum_{\alpha,\beta} \frac{1}{(E_\alpha - \hbar\omega_i)(E_\beta - \hbar\omega_s)} \tag{2.3}$$

where ω_i is the incident photon frequency, ω_s is the scattered photon frequency, E_α and E_β are intermediate state energies, T is the Raman tensor, i is the incident polarization vector, and s is the scattered polarization vector. The summation in (2.3) occurs over all possible intermediate states i.e. Bloch states forming conduction and valence bands, exciton states, and impurity states in the bandgap.

Several approaches can be taken to analysis the Raman Spectra. Frequently the background of Raman spectra will be sloped or increasing. To facilitate spectra comparison, it is common to plot a spectrum's first derivative which flattens the background. A second derivative can be taken where the center of a symmetric positive peak will become the center of a negative peak. This removes the sloping background. Another method in analyzing Raman spectra is normalization. It adjusts the intensity of different spectra so they are on similar ranges. This is done by first subtracting the minimum intensity at every frequency so the baseline is zeroed. Then the intensity of the strongest common band is taken and all spectra are divided by this intensity. Therefore at that frequency, the intensity would be 1.0. To compare spectra without a common band, normalization can be performed by making the area under the spectrum equal to 1.0.

2.3.2 Selection Rules in Raman Spectroscopy

The selection rules that govern Raman scattering constitute one of the main features distinguishing it from IR spectroscopy where vibrational spectroscopy of simple molecular systems is concerned. The selection rules can be understood by the following discussion.

$$E_{Si} \alpha P_i \alpha \left(\frac{d\alpha_{ij}}{dq_n} \right) E_{0j} \tag{2.4}$$

E_{Si} is the electric field vector of the scattered light. The equation 2.4 shows that the incoming and outgoing electric fields (E_{0j} and E_{Si}) are related, for a given vibrational mode n, by the Raman tensor an which is defined in (2.5); if the element with subscripts i, j is non-zero, then Raman scattering is possible between (E_{0j} and E_{Si}). It is helpful to write out explicitly the tensor equation relating the incoming and outgoing light waves.

$$\left(E_{sx,}\ E_{sy,}\ E_{sz,} \right) = \begin{pmatrix} \alpha_{xx} & \alpha_{xy} & \alpha_{xz} \\ \alpha_{yx} & \alpha_{yy} & \alpha_{yz} \\ \alpha_{zx} & \alpha_{zy} & \alpha_{zz} \end{pmatrix} \begin{pmatrix} E_{0x} \\ E_{0y} \\ E_{0z} \end{pmatrix} \tag{2.5}$$

Group theory allows one to determine the symmetry species of the vibrational modes and also which elements of the Raman tensor are non-zero. Raman tensors are tabulated in many books (e.g., [3]). In order that this discussion is not too abstract, we shall now consider in elementary terms how different vibrational modes of simple molecules may be IR-active or Raman-active. The direction in which x and y axes are defined is arbitrary. Without detailed group theoretical analysis, we will simply state that the vibrations of the unit cell can in this case be classified into various symmetry types including two with conventional labels A_{1g} and Eg. The Raman tensors for these are as follows:

$$A_{1g} \approx \begin{pmatrix} a & 0 & 0 \\ 0 & a & 0 \\ 0 & 0 & b \end{pmatrix} E_g \approx \begin{pmatrix} c & 0 & d \\ 0 & c & 0 \\ d & 0 & b \end{pmatrix} or \begin{pmatrix} c & 0 & 0 \\ 0 & -c & d \\ 0 & d & 0 \end{pmatrix} \qquad (2.6)$$

By referring to equation (2.4), then, we expect Raman scattering from light polarized the x axis to yield light polarized along the x axis for A_{1g} vibrational modes and along x (relative intensity c2) or z (relative intensity d2) for Eg vibrational modes. On the other hand, if the incident light is polarized parallel to the high-symmetry z axis, Raman scattering from an Eg mode will be polarized only along the x axis whilst Raman scattering from an A_{1g} mode will be polarized only along the z axis. This is borne out by experiment.

2.3.4 Relaxation of Raman Selection Rules

Nanostructured materials are generally synthesized in a number of forms: as isolated or loosely connected nanoparticles in the form of powder, as composites of nanoparticles dispersed in a host or as a compact collection of nano-grains as pellets or thin films. Though in principle one can define a nanostructured material as one in which at least one of the dimensions is less than few nanometer, it is often found that several properties do not differ from those of the bulk unless the dimension is less than typically 20 nm [8, 9]. In view of this, it is appropriate to define a critical size below which the property of interest differs from that of the bulk value by at least a few percent. The critical size is thus governed by the property and sometimes also by the method of synthesis. This is due to the defect structures and their concentration. Monoatomic solids with two atoms per primitive cell, such as diamond, magnesium, or diatomic compounds such as GaAs, have three optic phonon branches in addition to the three acoustic phonons. These phonons can propagate in the lattice of a single crystal as a wave and exhibit dispersion depending on their wavelength, or equivalently their wavevector in the Brillouin zone. The momentum conservation selection rule determines the region of the Brillouin zone that can be accessed in the Raman scattering/infrared absorption process. The wavevector of the IR photon for these energies is of the order of 10^2–10^3 cm^{-1}. On the other hand, in a Raman scattering experiment the magnitude of scattering vector is $2k_0 \sin(\theta/2)$, where k_0 is the wavevector of the incident light and θ the scattering angle. Therefore the maximum value of the scattering vector could at best be $2k_0$ (corresponding to the backscattering geometry), which has a value ~5×10^4 cm^{-1} for visible light. Hence, the wavevector probed by either of these techniques is much smaller than the wavevector q of the full phonon dispersion curve, which extends up to the boundary of the Brillouin zone ($\pi/a \sim 10^8$ cm^{-1}, where a is the lattice parameter). Furthermore, as the wavenumber of the acoustic phonons corresponding to $q \sim 5 \times 10^4$ cm^{-1} is just about 1 cm^{-1}, it is not straightforward to investigate the acoustic phonons using conventional Raman equipment. Because of this, the acoustic phonons are most conveniently probed using a Brillouin spectrometer consisting of a Fabry–Perot interferometer. Thus IR and Raman techniques sample only the optical phonons close to the zone centre ($q \approx 0$). This $q \approx 0$ selection rule is essentially a consequence of the infinite periodicity of the crystal lattice. However, if the periodicity of the crystal is interrupted, as in the case of nanocrystalline materials, this rule is relaxed. This is because the phonon propagation gets interrupted when a grain boundary is encountered in a polycrystalline material. In an isolated grain the phonon can get reflected from the boundaries and remain confined within the grain. However, from the point of view of phonons, a well-crystallized polycrystalline sample with a grain size of several micro-metres can be treated as a bulk/infinite crystal for all practical purposes. The consequences of phonon confinement are noticeable in the vibrational spectra only when the grain size is smaller than typically lattice parameters. As mentioned earlier, in ideal single crystals only the zone-centre optical phonons can be observed using optical techniques such as Raman spectroscopy. However, this $q \approx 0$ selection rule is relaxed owing to interruption of lattice periodicity in a atomically thin material. This can be qualitatively explained in the following manner: For a particle of size d, the phonon wavefunction must decay to a very small value close to the boundary. This restriction on the spatial extent of the wavefunction, via a relationship of the uncertainty principle type, leads to discrete values of wave vector q, of which the smallest q is π/d, and its multiples. This allows phonons corresponding to these selected wave vectors to be sampled by techniques such as Raman spectroscopy. The additional contribution to the Raman intensity from these phonons results in asymmetric broadening of the line shape. Strictly speaking, phonons of several q's over the complete Brillouin zone contribute to the spectral line shape; however, their relative contributions gradually diminish as q approaches the Brillouin-zone boundary. The conceptual visualization of phonon confinement in an isolated nanoparticle, as discussed above, is straightforward; however, several nanostructured systems exist as composites, i.e. nanoparticles embedded in a host matrix or as a thin 2D layer sandwiched between layers of another material, e.g. semiconductor heterostructures. In order to understand the phonon confinement in such cases, one needs to consider the phonon spectra of the particle/layer as well as that of the host. If the optical phonon dispersion curves of the particle/layer do not overlap with that of the host, then these phonons cannot propagate into the host material and the confinement effects are similar to those of an isolated particle, e.g. a GaAs particle embedded in an AlAs matrix. On the other hand, if the phonon dispersion curves of the particle and that of the host overlap partially or completely, as in the case of AlAs and InP, then the phonon confinement can be weak, and partially confined/propagating phonons can exist in such systems. Three different types of approaches have been used to theoretically investigate the consequences of confinement on phonon spectra. In analogy with the spatial correlation model originally developed for disordered and amorphous materials a Gaussian confinement model was proposed by Richter et al. [10] and generalized by Campbell and Fauchet [11] to take into account the contribution from phonons away from the zone centre. Subsequently, Roca et al. [12] presented a rigorous continuum theory, which took into account the coupling between the vibrational amplitude and electrostatic potential to obtain the optical vibrational modes in a spherical quantum dot, and applied it to several systems. Microscopic lattice dynamical calculations for nanoparticles containing up to a few thousand atoms have also been carried out and the changes in the phonon spectra as compared to the bulk have been discussed.

2.3.4 Resonant Raman Scattering

Resonance Raman scattering (RRS) occurs when the exciting line is chosen so that its energy intercepts the manifold of an electronic excited state. In detail, it occurs when the sample is irradiated with an exciting line whose energy corresponds to that of the electronic transition of a particular chromophoric group in a molecule. Under these conditions, the intensities of Raman bands originating in this chromophore are selectively enhanced by a factor of 10^3 to 10^5. This selectivity is important not only for identifying vibrations of this particular chromophore in a complex spectrum, but also for locating its electronic transitions in an absorption spectrum. Theoretically, the intensity of a Raman band observed at $\upsilon_0 - \upsilon_{mn}$ is given by [3]:

$$I_{mn} \alpha I_0 (\upsilon_0 - \upsilon_{mn})^4 \sum_{p\sigma} \left| (\alpha_{p\sigma}) \right|_{mn}^2 \qquad (2.7)$$

Here, m and n denote the initial and final states, respectively, of the electronic ground state. Although not explicit in Eq. (2.7), *e* represents an electronic excited state (see Figure 2.3) involved in Raman scattering, I_0 is the intensity of the incident laser beam of frequency υ_0.

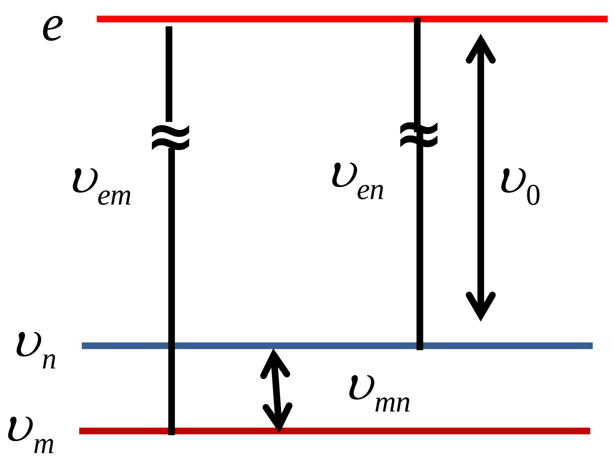

Figure 2.3: Schematic illustration describing the resonant Raman scattering process.

The $(\upsilon_0 - \upsilon_{mn})^4$ term expresses the υ^4 rule. Finally $(\alpha_{\rho\sigma})_{mn}$ represents the change in polarizability caused by the $m \rightarrow e \rightarrow n$ transition, and ρ and σ are x, y and z components of the polarizability tensor.

This term can be rewritten as

$$(\alpha_{\rho\sigma})_{mn} = \frac{1}{h}\sum\left(\frac{M_{me}M_{en}}{\upsilon_{em} - \upsilon_0 + i\Gamma_e} + \frac{M_{me}M_{en}}{\upsilon_{en} + \upsilon_0 + i\Gamma_e}\right), \qquad (2.8)$$

where υ_{en} and υ_{em} are the frequencies corresponding to the energy differences between the states subscribed and h is Planck's constant. M_{en} M_{me} etc., are the electric transition moments, such as

$$M_{me} = \int \Psi_m^* \mu_e \Psi_e d\tau . \qquad (2.9)$$

Here Ψ_m and Ψ_e are total wavefunctions of the m and e states, respectively, and μ_e is the σ component of the electric dipole moment.

In normal Raman scattering, υ_0 is chosen so that $\upsilon_0 \ll \upsilon_{em}$. Namely, the energy of the incident beam is much smaller than that of an electronic transition. Under these conditions, the Raman intensity is proportional to $(\upsilon_0 - \upsilon_{mn})^4$ As υ_0 approaches υ_{em}, the denominator of the first term in the brackets of Eq. (2.8) becomes very small. Hence, this term ("resonance term") becomes so large that the intensity of the Raman band at $\upsilon_0 - \upsilon_{mn}$ increases enormously. This phenomenon is called resonance Raman scattering.

2.3.6 Applications of Raman Spectroscopy

Raman spectroscopy is commonly used in chemistry, since vibrational information is specific to the chemical bonds and symmetry of molecules. It therefore provides a fingerprint by which the molecule can be identified. For instance, the vibrational frequencies of SiO_2, Si_2O_2, and Si_3O_3 were identified and assigned on the basis of normal coordinate analyses using infrared and Raman spectra. The fingerprint region of organic molecules is in the (wavenumber) range 500–2000 cm^{-1}. Another way that the technique is used is to study changes in chemical bonding, e.g., when a substrate is added to an enzyme. Raman gas analyzers have many practical applications. For instance, they are used in medicine for real-time monitoring of anaesthetic and respiratory gas mixtures during surgery.

In solid state physics, spontaneous Raman spectroscopy is used to, among other things, characterize materials, measure temperature, and find the crystallographic orientation of a sample. As with single molecules, a given solid material has characteristic phonon modes that can help an experimenter identify it. In addition, Raman spectroscopy can be used to observe other low frequency excitations of the solid, such as plasmons, magnons, and superconducting gap excitations. The spontaneous Raman signal gives information on the population of a given phonon mode in the ratio between the Stokes (downshifted) intensity and anti-Stokes (upshifted) intensity.

Raman scattering by an anisotropic crystal gives information on the crystal orientation. The polarization of the Raman scattered light with respect to the crystal and the polarization of the laser light can be used to find the orientation of the crystal, if the crystal structure (specifically, its point group) is known.

Raman active fibers, such as aramid and carbon, have vibrational modes that show a shift in Raman frequency with applied stress. Polypropylene fibers also exhibit similar shifts. The radial breathing mode is a commonly used technique to evaluate the diameter of carbon nanotubes. In nanotechnology, a Raman microscope can be used to analyze nanowires to better understand the composition of the structures.

Spatially-offset Raman spectroscopy (SORS), which is less sensitive to surface layers than conventional Raman, can be used to discover counterfeit drugs without opening their internal packaging, and for non-invasive monitoring of biological tissue. Raman spectroscopy can be used to investigate the chemical composition of historical documents and contribute to knowledge of the social and economic conditions at the time the documents were produced. This is especially helpful because Raman spectroscopy offers a non-invasive way to determine the best course of preservation or conservation treatment for such materials. Raman spectroscopy is being investigated as a means to detect explosives for airport security.

2.4 Summary

In this chapter, the basic theoretical overview of quantization of lattice vibration; i.e. phonon was provided. The chapter was continued with detail discussions on phonon vibrational Raman spectroscopy. Use of Raman spectroscoly could be a useful tool to exploit new nanostructured materials (i.e. 2D, 1D, 0D) for further engineering applications. This can provide further various insights on material composition, quality control, disorder, thickness detection (i.e. nanometrology) down to nanoscale regime.

References

[1] C. Kittel, *Introduction to Solid State Physics*, 8th ed., Wiley, ISBN-10: 047141526X (2004).

[2] J. Singh, *Physics of Semiconductors and their Heterostructures*. McGraw-Hill, ISBN-10: 0070576076 (1992).

[3] P. Y. Yu and M. Cardona, *Fundamentals of Semiconductors* **3**, ISBN 3-540-25470-6, (2005).

[4] A. Balandin., *Phys. Low-Dim Structures, **1-2**,* 1 (2000).

[5] G. Chen. A. Narayanaswamy, and C. Dames., *Superlattices and Microstructures*, **35**, 161–172 (2004).

[6] C. V. Raman and K. S. Krishnan, *Indian Journal of Physics*, **2**, 399–419 (1928).

[7] M. A. Stroscio and M. Dutta, *Phonons in Nanostructures*, 1st ed., Cambridge University Press, Cambridge, (2001).

[8] U. Woggon, *Optical Properties of Semiconductor Quantum Dots.* 1st ed., ISBN-10: 3540609067, Springer: Berlin (1996).

[9] H. S. Natwa (ed), *Handbook of Nanostructured Materials & Nanotechnology*, vol. 2, Academic press: New York, 213 (2000).

[10] H. Richter, Z. P. Wang and L. Ley, *Solid State Communication,* **39,**625 (1981).

[11] H. Campbell and P. M. Fauchet. *Solid State Communication*, **58**, 739, (1986).

[12] E. Roca, C. T. Giner and M. Cardona, *Phys. Rev., B*, **49**, 13704 (1994).

Chapter 3

Nanostructures: Quasi 2D Materials

3.1 Introduction

Nanostructure is the group of materials with at least one dimension in the nanometer scale. If only one dimension is restricted, we will have a layered shape or 2D material; if two dimensions are limited in size, we will have a wired or 1D material; if all dimensions are in the range of a few nanometres we usually have 0D materials. Restriction of size in one or more dimensions could effectively change some properties of materials. Optical and electronic properties usually changes not only due to confinement of electrons but also due to the absence of interlayer interactions. Some other changes in properties, such as mechanical and chemical response, are mainly due to different geometry and relatively high surface-bulk ratio. The size and shape of nanomaterials determine their intrinsic properties and behavior. Following the success of graphene [1] i.e. two-dimensional (2D) sheets of carbon exhibiting novel electronic properties; there has been increasing interest in 2D forms of other materials.

3.2 2D Materials: Graphene and Beyond

During the last five decades, an extensive effort was invested in obtaining single atomic layers of graphite, with the aim of having access to the predicted properties of a tightly bond one-atom thick layer of sp^2 carbon. In fact, many techniques had been tested in the past with only moderate success. Most of the reported works until the mid-1990s were focused on graphite intercalation compounds. In these compounds, a host molecule or atom gets ''sandwiched'' between the graphite layers, resulting in a weakening of interplanar forces and facilitating separation of layers. Among these compounds the use of expandable graphite, a compound that can expand in volume by a factor of up to 1000 upon rapid heating, was widespread during the 1960s, but the best results were materials with few (10–50) layers. Many other more sophisticated techniques were tested and reported during the next decades with only moderate success, since the thinner flakes observed were around 10 layers.

Single atomic layers of graphite were first isolated by Andre Geim's group, at Manchester University in 2004 lead them to win Nobel Prize in physics in 2010 [1]. Graphene is a single layer of graphite; that has been one of the first real two dimensional materials (i.e. one atom thick) to be isolated in nature. Figure 3.1 shows a representative optical image of single layer graphene (SLG) attached to multilayer flakes. The figure also shows atomic structure SLG consists of sp^2 bonded C-C atom.

The recent increase of graphene literature evidences not only its basic scientific interest but also its potential technological impact. Extraordinary properties of graphene

[1–5] such as its extremely high room temperature electron mobility [1–3] and thermal conductivity [4, 5] make this material appealing. Graphene is also called Dirac materials as it possess a unique Dirac-like cone type of low-energy band structure within the first Brillioun zone. This property allows for the production of extraordinary electrons that are distinctive from standard electron produced in metals.

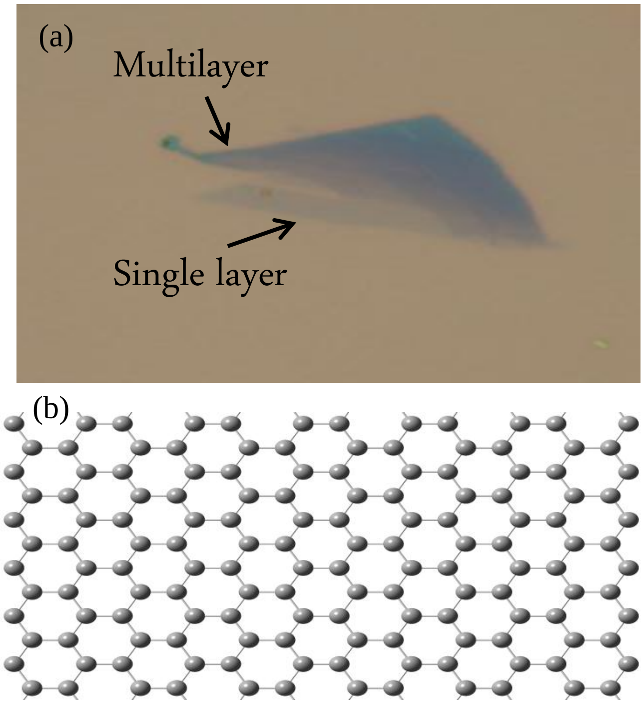

Figure 3.1 (a) Optical image of graphen showing single layer and multilayer graphene, (b) Atomic structure of graphene showing single layer of sp^2 bonded C-C atoms.

Typical electrons tend to behave like massive particles and have a quadratic energy dependence on momentum, which obey Schrodinger’s equation.

The Dirac electrons, on the other hand, have energies that contain a linear dependence on momentum and follow Dirac equations. The Dirac electrons behave like massless fermions which allow for ballistic transport along the surface of the Dirac material. Unlike other massless particles though, such as neutrinos, Dirac electrons have a charge. As a result, electrons in Dirac materials are charged massless particles that can easily be influenced by an external magnetic field. This opens the door to some exotic physics and physical properties in Dirac materials that are not found in typical materials, which may be utilized for a plethora of future applications.

In view of the success obtained in the search for graphene layers, the ideas and methodology learnt in these studies have been extended to other layered materials. Thus, graphene is becoming a cutting edge material that opens up new horizons to a whole new variety of possibilities beyond the limited current applicability of graphene. Fortunately, it is not only graphite that responds to the idea of pulling out one layer from a three dimensional material with strong covalent in-plane bonds and weak van der Waals-like coupling between layers.

Two dimensional (2D) layer of Bi_2Te_3, [6-7] Bi_2Se_3 [8], MnO_2 [9], $Bi_2SrTa_2O_9$ [10], BN [11] $NbSe_2$ [12], MoS_2 [13] and others have been prepared by exfoliation of bulk crystal, leaving a variety of flakes attached to it. The resulting 2D materials so obtained exhibit high crystal quality and macroscopic continuity, as in the case of graphene. These materials intrinsically have a 2D character and are termed as “Quasi-2D”. It may also be possible to produce new hybrid devices with unprecedented functionalities by stacking layers of different materials. These studies [1-13] will help future work in 2D materials with more complex compositions and structures. It is too early to say whether or not 2D materials will be present in future technology.

However, the recent findings in this field [1-13] indicate that their influence will be noticeable in the near future.

3.3 Quasi 2D Materials

3.3.1 B_V-A_{VI} compounds: Bi_2Te_3, Bi_2Se_3 and Sb_2Te_3

The B_V-A_{VI} compounds (i.e. Bi_2Te_3, Bi_2Se_3 and Sb_2Te_3) exhibit a layered, rhombohedral crystal structure of the space group $R\bar{3}m(D^5_{3d})$, and are composed of hexagonal close-packed atomic layers which are periodically arranged along the C_H axis in five layers as follows [14]

$$A_{VI}^{(1)}\text{-}B_V\text{-}A_{VI}^{(2)}\text{-}B_V\text{-}A_{VI}^{(1)} \quad (3.1)$$

Here the subscript corresponds to the group of the element in the periodic system, and the superscripts on the A_{VI} atoms designate the different positions within the fivefold layer. A_{VI} may be either Te or Se, and B_V, either Bi or Sb. The superscripts on the A_{VI} atoms designate the different positions within the fivefold layer. The 5-layer stacks are centro-symmetrical with respect to $A_{VI}^{(2)}$ which plays a role of an inversion center [15]. The conventional unit cell spans over three quintuple layers and each quintuple layer has a thickness of H~1 nm. The quintuple layers are weakly bound to each other by the van der Waals forces that allow one to disassemble B_V-A_{VI} crystal into its building blocks. In some cases, the atomic five-folds can be broken further into sub-quintuple leading to B_V-A_{VI} atomic bi-layers and B_V-A_{VI}-B_V atomic tri-layers. While the band gap in a single quintuple is larger than in a few-quintuple layer (FQL), the latter has less coupling between the surface states of the top and bottom interfaces. The nearest-neighbour distances between atoms in different mono atomic layers are given in Table 3.1 for the three pure binary compounds.

Table 3.1: Nearest neighbor distances ($\overset{0}{A}$) for atoms in different layers [14]

	Sb_2Te_3	Bi_2Te_3	Bi_2Se_3
d_1 (V-VI$^{(1)}$)	3.06	3.04	2.99
d_2 (V-VI$^{(2)}$)	3.16	3.24	3.06
d_3 (VI$^{(1)}$-VI$^{(1)}$)	3.64	3.72	3.27

Within the fivefold layer covalent bonding is assumed to dominate a small ionic contribution. The valence electron states are thought to form highly excited hybrids of the type sp^3d^2 or p^3d^3 around the B_V, lattice sites, which may bind the approximately octahedral nearest A_{VI} neighbors, three in each of the adjacent $A_{VI}^{(1)}$ and $A_{VI}^{(2)}$ layers. The weaker bonds between the fivefold layers (i.e. between the $A_{VI}^{(1)}$ double atomic layers) are assumed to be of the van der Waals type.

3.3.2 Crystal Structure and Lattice Vibrations of Bi_2Te_3

The crystal structure of Bi_2Te_3 is rhombohedral with five atoms in one unit cell [15]. The lattice parameters of the hexagonal cells of Bi_2Te_3 are a_H = 0.4384 nm and c_H = 3.045 nm.

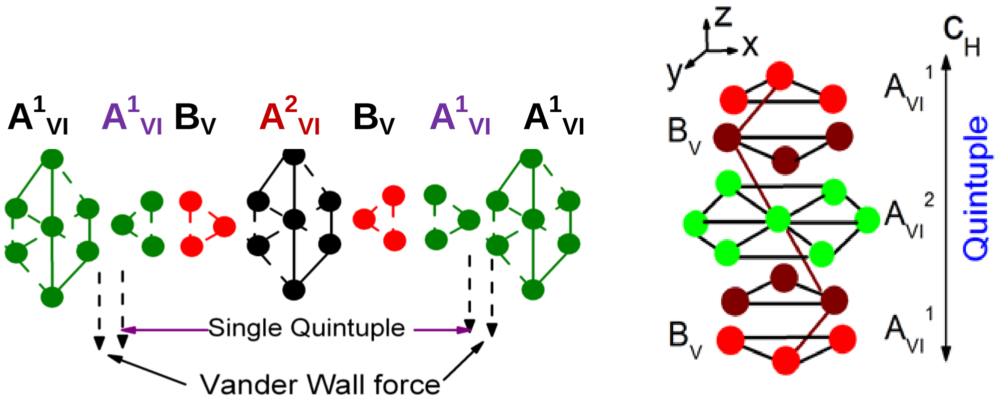

Figure 3.2 Crystal structure of the rhombohedral (B_V-A_{VI}) Bi_2Te_3.

Its atomic arrangement can be visualized in terms of the layered sandwich structure as shown in Figure 3.2. Each sandwich is built up by five mono-atomic sheets {-$Te^{(1)}$-Bi-$Te^{(2)}$-Bi-$Te^{(1)}$-}, referred to as atomic five-folds, along the C_H axis. The superscripts (1) and (2) denote two different chemical states for the anions. The outmost atoms $Te^{(1)}$ are strongly bound to three planar $Te^{(1)}$ and three Bi metal atoms of the same five-fold (also referred to as quintuple) layers and weakly bound to three $Te^{(1)}$ atoms of the next five-fold. The presence of the van der Waals gap allows one to disassemble Bi_2Te_3 crystal into its building blocks – five mono-atomic sheets of $Te^{(1)}$-Bi-$Te^{(2)}$-Bi-$Te^{(1)}$, which have the thickness of ~1 nm. In some cases, the atomic five-folds can be broken further leading to Bi-Te atomic bi-layers and Bi-Te-Bi atomic tri-layers. The bond strength within the five-fold is not the same. The Bi-Te$^{(1)}$ bond is stronger than Bi-Te$^{(2)}$ bond which is the second weakest points within the crystal structure.

The latter creates a possibility for producing quasi 2-D atomic tri-layers and bi-layers. The Bi-Te$^{(2)}$ bond is covalent while the Bi-Te$^{(1)}$ binding includes both covalent and ionic interaction. In Bi_2Te_3 the 5-layer stacks are centrosymmetrical with respect to Te$^{(2)}$ which has also the role of an inversion center [15]. Any crystal with inversion symmetry in said to be centrosymmetric [16]. The very easy cleavage plane perpendicular to the trigonal axis is attributed to a weak Te,-Te, binding, believed to be mainly of Van der Waals character, in contrast to the largely covalent Bi-Te bonds [14, 15]. In fact, as a result of the present investigation, we now conclude that covalent binding plays an important role even for the interlayer interaction in Bi_2Te_3.

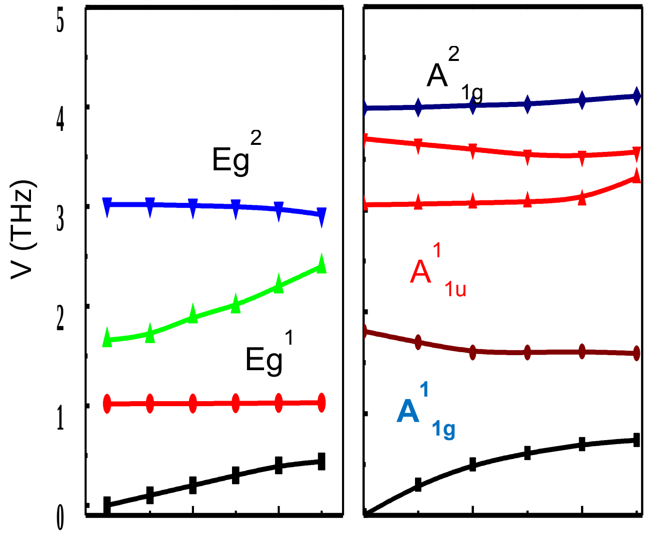

Figure 3.3: The frequencies of longitudinal (Λ_1) and transverse (Λ_3) normal modes of vibration of Bi_2Te_3 propagating along the trigonal axis [15].

Normal modes of vibration propagating along the trigonal c-axis involve motions of entire planes of atoms, either parallel or perpendicular to C_H, and thus depend directly upon the interplanar forces in which we are primarily interested. The reported results [15] for lattice vibrations propagating along the trigonal axis perpendicular to the layers are shown in Fig. 3.3 for the two polarizations, longitudinal **(**Λ_1**)** and transverse **(**Λ_3**)**. Analysis of these normal mode frequencies in terms of a simple one-dimensional model leads at once to numerical values for the interplanar force constants. Since Bi, Te, has five atoms in the primitive unit cell, there will in general be 15 branches of the normal mode. The frequencies of vibrational modes at 77K and 300K are listed in Table 3.2.

Table 3.2 Normal mode frequencies (THz) for the high symmetry points Γ and Z in Bi_2Te_3 at 77K and 300K [15]

Modes	**77K**		**300K**	
	Γ	Z	Γ	Z
Longitudinal modes	4.24±0.08	4.32±0.09	4.00	4.12
				3.57
	3.70±0.12	3.60±0.12	3.05	3.32
	3.10±0.06	3.30±0.07	1.81	1.59
	1.93±0.14	1.65±0.03		0.74
		0.78±0.04		
Transverse modes	3.05±0.05	2.98	3.02	2.92
	2.60±0.15	2.60		
	1.56±0.10	2.25±0.05	1.66±0.10	2.40±0.10
	0.98±0.04	1.17±0.04	1.02	1.03
	3.05±0.05	0.51±0.04		0.44

At the Brillouin zone centre, there are four distinct representations, namely $2\Gamma_1^+$, $2\Gamma_3^+, 3\Gamma_2^-$ and $3\Gamma_3^-$. The Γ_1^+ and Γ_{31}^+, modes are Raman active, while the $3\Gamma_2^-$ and $3\Gamma_3^-$**;** modes of non-zero frequency are infra-red active. For modes propagating along the c-axis, it is readily shown from symmetry arguments that there are five non-degenerate longitudinal modes (L, Λ_1**)** and five double degenerate transverse modes (T, Λ_3**).**

3.3.3 Symmetry Properties and Selection Rules

The crystal structure has the following symmetry elements: one trigonal axis perpendicular to the atomic layers, three binary axes parallel to the atomic layers, three mirror planes which contain the trigonal axis and are each perpendicular to one of the binary axis, and finally the $A_{VI}^{(2)}$ atoms are centres of inversion. The primitive unit cell of Bi_2Se_3, Bi_2Te_3 and Sb_2Te_3, contains five atoms in accordance with the chemical formula. There are consequently 15 lattice dynamical modes at p = 0, three of which are acoustic modes and 12 optical modes Group theory classifies these 12 optical modes into $2A_{1g}$, 2Eg, $2A_{1u}$, and 2Eu. The corresponding atomic displacements are shown in Fig. 3.4. The letters “E” and “A” indicate the in-plane and out-of-plane (C_H axis) lattice vibrations, respectively. The subscript “g” denotes Raman active while “u” stands for IR-active modes. The optical modes belonging to A_{1u} and E_u are allowed to be infrared active. According to selection rule given in Table 3.3, the off-diagonal Raman tensor components of the E_g mode distinguish itself from A_{1g} mode. This is because; a general phonon of this type E_g possesses displacements in both x- and y- direction. In the E_g^1 and

A^1_{1g}, modes the outer B_V-$A_{VI}^{(l}$) pairs move in phase . Thus the B_V-$A_{VI}^{(2)}$ bonding forces will be primarily involved in these vibrations. Whereas, in the Eg^2 and A^2_{1g} modes the outer B_V and $A_{VI}^{(l)}$ atoms move in opposite phase, will mainly be affected by forces between B_V and $A_{VI}^{(l)}$ atoms. The nearest-neighbor distances between B_V and $A_{VI}^{(1)}$ atoms are smaller than those between B_V and $A_{VI}^{(2)}$ atoms [14]. Because of this the A^1_{1g} and E_g^1 modes occur at lower frequencies than the A^2_{1g} and Eg^2 modes.

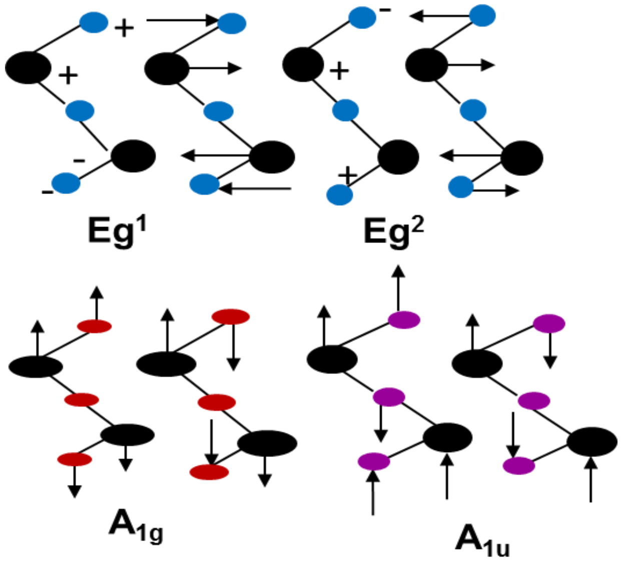

Figure 3.4: Infrared- and Raman-active modes of B_V-A_{VI} showing in plane and out of plane modes of vibration.

Because of inversion symmetry these modes are exclusively Raman- or infrared-active according to the selection rules given in Table 3.3. It follows that the E_g, and A_{lg}**,** modes may be distinguished from one another as a result of the off-diagonal Raman tensor components of the E_g, modes. Similarly, the symmetry of the infrared-active modes may be ascertained by polarizing the incident light either parallelly (A_{lu}) or perpendicularly (Eu) to the c-axis [14].

Table 3.3: Selection rule for one phonon infrared absorption (IR) and Raman scattering in B_V-A_{VI} compounds having *R-3m* symmetry

Modes		**Selection rule**	
Symmetry	number	Raman	IR
A_{1g}	2	$\begin{pmatrix} a & 0 & 0 \\ 0 & a & 0 \\ 0 & 0 & a \end{pmatrix}$	-
E_g	2	$\begin{pmatrix} c & 0 & 0 \\ 0 & -c & d \\ 0 & d & 0 \end{pmatrix} \begin{pmatrix} 0 & -c & d \\ -c & 0 & 0 \\ -d & 0 & 0 \end{pmatrix}$	-
A_{1u}	2	-	E||c
Eu	2	-	$E \perp c$

From the nearest-neighbour distances (Table 3.1) and also from the lattice dynamical model used by Jenkins et al. [17] it is reasonable to assume that the nearest-neighbour force constants between V and $VI^{(2)}$ atoms are smaller than those between V and $VI^{(1)}$ atoms. Consequently, one expects the $A^1{}_{1g}$ and $E_g{}^1$ modes to occur at lower frequencies than the $A^2{}_{1g}$ and $E_g{}^2$ modes. The latter modes, where the outer V and $VI^{(l)}$ atoms move in opposite phase, will mainly be affected by forces between V and $VI^{(l)}$ atoms.

3.4 Topological Insulators

Dissipation less transport mechanism could be extremely useful for semiconductor devices. Unfortunately, the requirement of a large magnetic field severely limits the application potential of the Quantum Hall (QH) effect. In the past few years, theoretical developments suggest that new classes of topological states of quantum matter might exist in nature. Such states are purely topological in nature in the sense that they do not break time-reversal (TR) symmetry, and hence can be realized without any applied magnetic field: "Quantum Hall-like effects without magnetic field". Thus a new class of topological states has emerged called Quantum spin hall (QSH) states or topological insulator. QSH states have been theoretically predicted and experimentally observed in mercury telluride quantum well, bismuth antimony alloys [18] and in Bi_2Se_3 and Bi_2Te_3 bulk crystals [19, 20].

In particular Quantum Hall (QH) states require an external magnetic field, which breaks TR symmetry; QSH states, in contrast are TR invariant and do not require an applied magnetic field. QSH systems are insulating in the bulk, they have an energy gap separating the valence and conduction bands but on the boundary they have gapless edge or surface states that are topologically protected and immune to impurities or geometrical perturbations [21]. Such systems are thought to provide an avenue for the realization of fault-tolerant quantum computing because they contain surface states that are topologically protected against scattering by time-reversal symmetry. A certain class of three-dimensional topological insulator material can have protected surface states and display other topological behavior potentially up to room temperature without magnetic fields.

In the bulk of a topological insulator the electronic band structure resembles an ordinary band insulator, with the Fermi level falling between the conduction and valence bands. On the surface of a topological insulator there are special states that fall within the bulk energy gap and allow surface metallic conduction (see figure 3.5). The surface states consist of an odd number of massless Dirac cones, with a single Dirac cone being the simplest case. The existence of an odd number of massless Dirac cones on the surface is ensured by the Z2 topological invariant of the bulk [19].

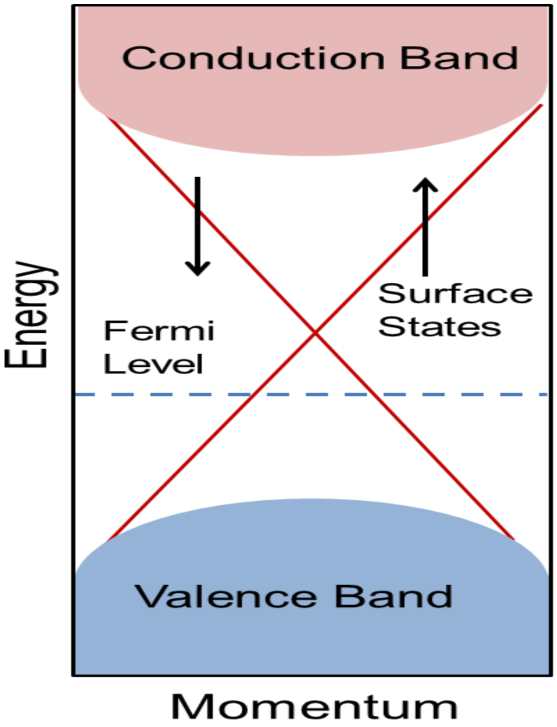

Figure 3.5: Schematic diagram of a typical band structure for a topological insulator. The Fermi level falls within the bulk band gap which is traversed by topologically-protected surface states.

Recently, it was realized that topological phases can also exist in simple two-dimensional (2D) band insulators which preserve TRS [21, 22]. These insulators have two phases and are said to be characterized by a topological Z2 invariant. Two-dimensional topological insulators are predicted to exhibit similar edge states even in the absence of a magnetic field because spin-orbit coupling can simulate its effect due to the relativistic terms added in a band insulator's Hamiltonian.

This observation demonstrates that Bi_2Te_3 is an ideal candidate as the parent compound for the simplest kind of 3D topological insulator. The Te ^{2}/Se^2 site has the role of an inversion centre and under an inversion operation, Bi^1 is changed to Bi^1 and Se^1 is changed to Se^1. The existence of inversion symmetry enables us to construct eigenstates with definite parity for this system [19]. The reason of using thin film (2D) now is because that due to the defects of the crystal, there is usually residual bulk carrier/conductance in the samples. In this case, the thin film is easier to be gated so the chemical potential can be tuned into the bulk gap. This is not necessary if the sample is perfect, i.e. no residual bulk conductance. However, if the sample quality can be improved in the future, this is not necessary. Further, the surface state can be dominating in thin films making the observation of the surface effects more easily; also they can even coupled between top and bulk surfaces and cause periodic quantum behavior depending on the thickness/layer number to be observed. This is another major and more interesting reason why people go to thin film rather than thick film. Depending on what kind of experiments people like to do, we can either embed thin or thick films between FM layers.

3.5 Summary

The chapter stared with a description of exotic properties of the leading cutting edge 2D material i.e. graphene followed by a brief outline of other promising quasi 2D nanostructured materials. A set of promising quasi 2D materials, i.e., Bi_2Te_3 and its related compounds has been discussed later. These new material are called “topological insular” with a bulk insulating gap, exhibiting quantum-Hall-like behaviour in the absence of a magnetic field. Such systems are thought to provide an avenue for the realization of fault-tolerant quantum computing because they contain surface states that are topologically protected against scattering by time-reversal symmetry. Fundamental discussions including crystal structure, phonon vibrational modes, selection rule etc. important for this study are also discussed in this chapter.

References

[1] K. S. Novoselov, A. K. Geim, S. V. Morozov, D. Jiang, Y. Zhang, S. V. Dubonos, I. V. Grigorieva, and A. A. Firsov, *Science* , **306**, 666 (2004); K. S. Novoselov, A. K. Geim, S. V. Morozov, D. Jiang, M. I. Katsnelson, I. V. Grigorieva, S. V. Dubonos, and A. A. Firsov, *Nature* **438**,197(2005).

[2] Y. B. Zhang, Y. W. Tan, H. L. Stormer, and P. Kim, *Nature* **438**, 201(2005); Y. W. Tan, Y. Zhang, H. L. Stormer, and P. Kim, *Eur. Phys. J. Spec. Top* **148**, 15(2007).

[3] S. V. Morozov, K. S. Novoselov, M. I. Katsnelson, F. Schedin, D. C. Elias, J. A. Jaszczak, and A. K. Geim, *Phys. Rev. Lett.* **100**, 016602 (2008).

[4] A. A. Balandin, S. Ghosh, W. Bao, I. Calizo, D. Teweldebrhan, F. Miao, and C. N. Lau, *Nano Lett.* **8**, 902(2008).

[5] S. Ghosh, I. Calizo, D. Teweldebrhan, E. P. Pokatilov, D. L. Nika, A. A. Balandin, W. Bao, F. Miao and C. N. Lau, *Appl. Phys. Lett.* **92**, 151911(2008); D. L. Nika, E. P. Pokatilov, A. S. Askerov, and A. A. Balandin, *Phys. Rev. B* **79**, 155413(2009).

[6] D. Teweldebrhan, V. Goyal and A. A. Balandin, *Nano Lett.* **10**, 1209 (2010). D. Teweldebrhan, V. Goyal, M. Rahman and A. A. Balandin, *Appl. Phys. Lett*. **96**, 053107 (2010).

[7] K. M. F. Shahil, M. Z. Hossain, D. Teweldebrhan, and A. A. Balandin, *Appl.Phys. Lett.* **96**, 153103 (2010).

[8] M. Z. Hossain, S. L. Rumyantsev, D. Teweldebrhan,K. M. F. Shahil, M. Shur, A. A. Balandin, *Physica Status Solidi (A), Applications and Materials* **208**, 1, 144-146 (2011). M. Z. Hossain, S. L. Rumyantsev, K. M. F. Shahil, D. Teweldebrhan, M. Shur, A. A. Balandin, *ACS Nano* **5** (4), 2657-2663 (2011).

[9] Y. Omomo, T. Sasaki, L. Z. Wang and M. Watanabe, *J. Am. Chem.Soc.* **125**, 3568–3575 (2003).

[10] S. Ida, C. Ogata, U. Unal, K. Izawa, T. Inoue, O. Altuntasoglu and Y. Matsumoto, *J. Am. Chem. Soc.* **129**, 8956–8957 (2007).

[11] Y. Lin, Tiffany, V. Williams and J. W. Connel, *J. Phys. Chem. Lett.***1**, 277–283 (2010).

[12] N. E. Staley, J. Wu, P. Eklund, Y. Liu, L. Li and Z. Xu, *Phys. Rev. B* **80**, 184505 (2009).

[13] J. Xiao, D. Choi, L. Cosimbescu, P. Koech, J. Liu and J. P. Lemmon, *Chem. Mater*. **22** (16), 4522–4524 (2010).

[14] W. Richter, H. Kohler and C. R. Becker, *Phys. stat. sol. (b)* **84**, 629 (1977).

[15] V. Wagner, G. Dolling, B. M. Powell and G. landwehr, *Phys stat. sol. (b)*, **85**, 311 (1978).

[16] P. Y. Yu and M. Cardona, *Fundamentals of Semiconductors* 3, ISBN 3-540-25470-6, (2005).

[17] J. 0. Jenkins, J. A. Rayne and R. W. Ure, *Phys. Rev. B*, **5**, 3171 (1972).

[18] L. Fu, C. L. Kane and E. J. Mele, *Phys. Rev. Lett.*, **98**, 106803(2007).

[19] H. Zhang, C. X. Liu, X. L. Qi, X. Dai, Z. Fang and S. C. Zhang, *Nat. Phys.* **5**, 438 (2009).

[20] Y. L. Chen, J. G. Analytis, J. H. Chu, Z. K. Liu, S. K. Mo, X. L. Qi, H. J. Zhang, D. H. Lu, X. Dai, Z. Fang, S. C. Zhang, I. R. Fisher, Z. Hussain and Z. X. Shen, *Science*, **325**, 178-181 (2009).

[21] C. L. Kane and E. J. Mele, *Phys. Rev. Lett.*, **95**, 146802 (2005).

[22] B. A. Bernevig and S. C. Zhang, *Phys. Rev. Lett.*, **96**, 106802 (2006).

Chapter 4

Experimental Methodology: Raman Nanometrology

4.1 Introduction

In this chapter*, the experimental methodology to study the Raman nanometrology of Topological Insulators (TIs) is described. The chapter discusses the method of sample preparation for the experimental measurements and also describes the experimental setup. In section 4.2, detail sample preparation techniques of FQL TIs is described followed by a brief description on the methodology of Raman spectroscopy in section 4.3.

---

* Part of this chapter has been excerpted with permission from the papers by K. M. F. Shahil, M. Z. Hossain, D. Teweldebrhan, and A. A. Balandin, "Crystal symmetry breaking in few-quintuple Bi_2Te_3 films: Applications in nanometrology of topological insulators" *Appl. Phys. Lett.* **96**,153103 (2010), © 2010 American Institute of Physics and K. M. F. Shahil, M. Z. Hossain, V. Goyal and A. A. Balandin, "Micro-Raman Spectroscopy of Mechanically Exfoliated Few-Quintuple Layers of Bi_2Te_3, Bi_2Se_3 and Sb_2Te_3 Materials" *Journal of Applied Physics* (2012), © 2012 American Institute of Physics.

4.2 Sample Preparation

4.2.1 Mechanical Exfoliation

We exfoliate the bismuth telluride and bismuth sellenoid on degenerately doped p-type Si substrate capped by 300 nm thickness of SiO_2 using the mechanical exfoliation process similar to graphene [1, 2]. The process was repeated several times to obtain layers with just a few atomic planes. Prior to the deposition, we clean the substrate in acetone and isopropanol (IPA) solution. Then a thin piece of samples peeled from a bulk sample using scotch tape and transferred on to the clean substrate. Our prior extensive experience with graphene [3, 4] and few layer garphene helps us to separate weakly distinguishable optical features in B_V-A_{VI} (A_{VI} may be either Te or Se, and B_V, either Bi or Sb) atomic layers placed on SiO_2/Si substrate. Owing to the specific structure of B_V-A_{VI} crystal along the C_H direction (C_H = 3.045 nm is a very large lattice constant as compared to other materials), we were able to verify the number of layers using the optical inspection combined with atomic force microscopy (AFM) and scanning electron microscopy (SEM). The thickness of the atomic quintuple is H ∼ 1 nm. The steplike changes in the cleaved layers highest of ∼1 nm can be distinguished well with AFM. The produced atomic layers were placed on Si substrates containing a 300 nm thick SiO_2 capping layer. The silicon oxide thickness was selected by analogy with that for graphene on Si/SiO_2. We then isolated and separate individual crystal planes which exhibited high crystal quality with little to no structural defects. The mechanical cleavage of B_V-A_{VI} (Bi_2Te_3/Bi_2Se_3/Sb_2Te_3) has led to a high portion of quintuples with five atomic planes.

In some cases, we observed atomic planes with thickness smaller than that of the quintuple layers. The produced flakes had various shapes and sizes ranging from ~2 to 30 μm. Some flakes had correct geometrical shapes indicative of the facets and suggesting a high degree of crystallinity. We selected large uniform B_V-A_{VI} flakes with dimensions of ~20-30 μm for fabrication of metal contacts for electrical characterization. The detailed sample preparation and identification techniques were described by some of us elsewhere [5-8].

4.2.2 Characterization Techniques: Optical and Scanning Electron Microscopy

The isolated few quintuple layer (FQL) films were investigated using a combination of optical and high-resolution field-emission scanning electron micro-scope (SEM, XL-30 FEG) operated at 10-15 kV. An SEM is essentially a high magnification microscope, which uses a focussed scanned electron beam to produce images of the sample, both top-down and, with the necessary sample preparation, cross-sections.

The representative high-resolution optical and SEM micrographs of some of our exfoliated FQL film are presented in this section. Figure 4.1 (a) shows an optical image of FQL Bismuth telluride, (b) shows SEM image of bulk Bismuth telluride film having dimension of ~ 40 μm×25 μm. As can be seen relatively thicker film can be easily identified through SEM inspection. An example of an exfoliated FQL with the lateral dimension of ~ 9 μm × 3 μm and uniform thickness is shown in Fig.4.1(c). A detail AFM inspection confirms a uniformity of this film with the thickness of ~15 quintuples. Some of the obtained FQLs were transferred to Si/SO$_2$ wafers with prefabricated trenches for better visualization and Raman characterization (see inset). The trenches were fabricated by reactive ion etching (RIE). They had a depth of ~ 300 nm and widths ranging from 1 to 5 μm. By suspending the ultrathin atomic films over these trenches, we reduced the coupling to the substrate. This allowed us to achieve a better understanding of the intrinsic properties of the atomically thin layers. Note that the sides of the trench are clearly seen through the film owing to its few-atomic thickness.

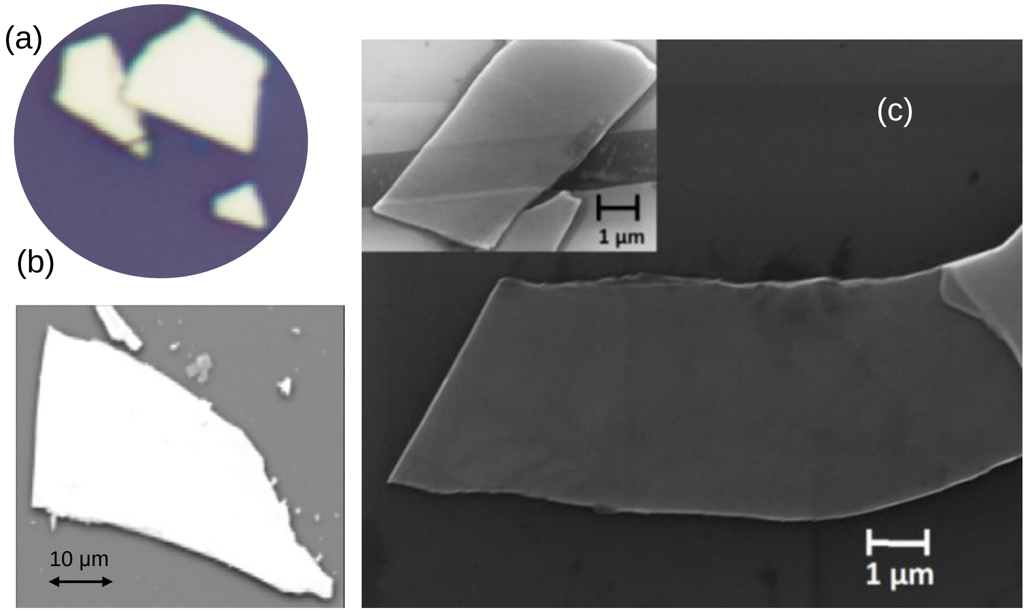

Figure 4.1: (a) Optical image of mechanically exfoliated Bi_2Te_3 film (b) SEM image of bulk Bi_2Te_3 film (c) SEM images of the mechanically exfoliated few-quintuple Bi_2Te_3 film with large lateral dimensions. The inset shows single-crystal bismuth telluride film suspended across a trench in Si/SiO$_2$ wafer. Reprinted in part with permission from K. M. F. Shahil, M. Z. Hossain, D. Teweldebrhan, and A. A. Balandin, *Appl. Phys. Lett*. **96**,153103 (2010), © 2010 American Institute of Physics.

Figure 4.2 (a-d) shows SEM images of various FQL films of Sb_2Te_3, Bi_2Se_3 and Bi_2Te_3, respectively. In Figure 4.2 (c)FQL Bi_2Te_3 crystal stack is attached to the edge of larger area flake.

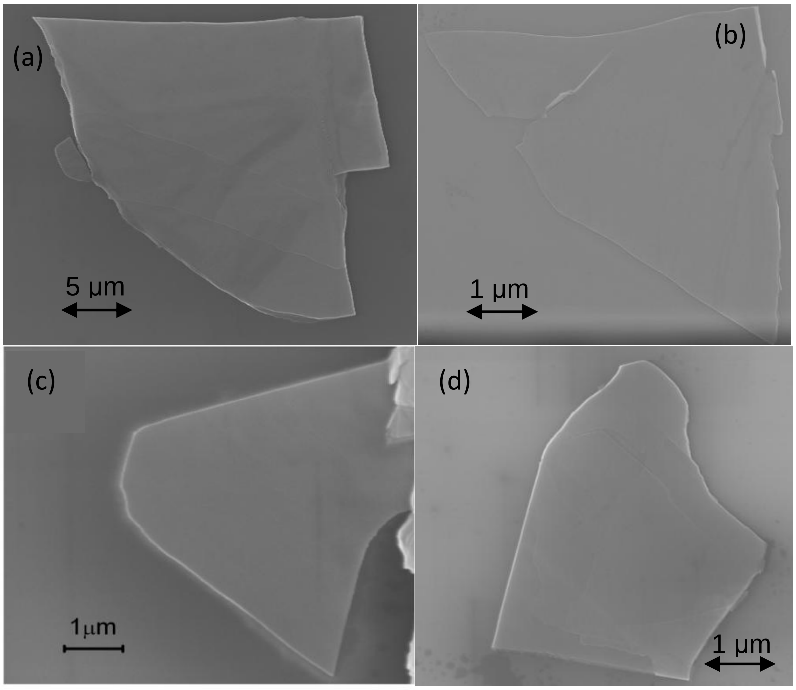

Figure 4.2: SEM images of exfoliated B_V-A_{VI} thin films with the large lateral dimensions showing (a) Sb_2Te_3, (b) Bi_2Se_3, and (c, d) Bi_2Te_3 flakes. Reprinted in part with permission from K. M. F. Shahil, M. Z. Hossain, V. Goyal and A. A. Balandin, "Micro-Raman Spectroscopy of Mechanically Exfoliated Few-Quintuple Layers of Bi_2Te_3, Bi_2Se_3 and Sb_2Te_3 Materials" *Journal of Applied Physics* (2012), © 2012 American Institute of Physics.

All FGL films have the lateral sizes ranging from a few microns to tens of microns. Some FQL samples show a uniform surface and have correct geometrical shapes indicative of the facets and suggesting the high degree of crystalinity.

4.2.3 Stoichiometric Composition and Crystallinity: Energy Dispersive Spectrometry and Transmission Electron Microscopy

It is known that these materials e.g. Bi_2Te_3, Bi_2Se_3 can be made either n or p type by changing the Bi/Te (Se) ratio. For example, if the composition is 40 % Bi and 60% Te then the material is p type. Even though the material that we assume is pure Bi_2Te_3, the relative Bi/Te composition does not have to be stochiometric, due to Bi/Te differential surface tension effects and constitutional supercooling effects [5].

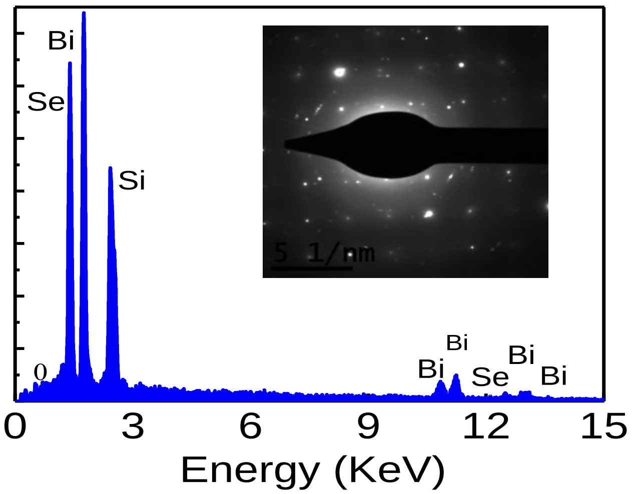

Figure 4.3: Structural and compositional characterization data showing EDS spectrum and electron diffraction pattern of Bi_2Se_3 FQL (inset) indicating the crystalline nature of the film. Reprinted in part with permission from K. M. F. Shahil, M. Z. Hossain, V. Goyal and A. A. Balandin, "Micro-Raman Spectroscopy of Mechanically Exfoliated Few-Quintuple Layers of Bi_2Te_3, Bi_2Se_3 and Sb_2Te_3 Materials" *Journal of Applied Physics* **XX** (2012), © 2012 American Institute of Physics.

In case of Bi_2Se_3, the defect chemistry is dominated by the charged selenium vacancies, which act as the electron donors resulting in *n*-type behavior. So, the elemental composition of FQL films was studied by the energy dispersive spectrometry (EDS) using Philips XL-30 FEG field-emission system. Figure 4.3 shows a representative EDS spectrum taken for Bi_2Se_3 FQL film. The molar contents of Bi and Se were found to be ~38.98 % and 54.55 %, respectively. A pronounced peak of Si indicates the electron beam penetration through thin FQL Bi_2Se_3 films. This peak is not visible in EDS spectra taken for bulk sample (not shown here) indicating that the exfoliated FQL films are atomically thin.

The selected area electron diffraction of the crystalline structures of the layers was studied using FEI-PHILIPS CM300 transmission electron microscopy (TEM). The sample preparation for TEM inspection was carried out through ultrasonic separation of dissolved samples in isopropyl alcohol (IPA) solution. The sonication was most effective with 500 μL of solution where the molar concentration of films was held at a constant 1.41×10^{-1} mol/L throughout the solution. The samples were then transferred onto carbon coated copper grids and studied under electron beam energy of 300 kV. The inset to Figure 4.3 shows a representative electron diffraction pattern of the crystalline structure of Bi_2Se_3 which indicates Bi-Se sample's perfect crystalline nature. So the exfoliated atomically thin layers of bismuth telluride/selenoid are crystalline after all processing steps.

4.2.4 Surface Profile and Thickness calibration: Atomic Force Microscopy

The thickness of different regions of the flakes was determined through Atomic Force microscopy (AFM) scans. AFM studies were performed using a VEECO instrument with the vertical resolution down to ~0.1 nm in order to estimate the thickness of FQLs. The thickness of the atomic quintuple is H~1 nm which can be clearly distinguished with AFM by the step like changes in the cleaved layers. The high-resolution AFM images of the exfoliated Bi_2Se_3 FQL are shown in Figure 4.4 (a, b).

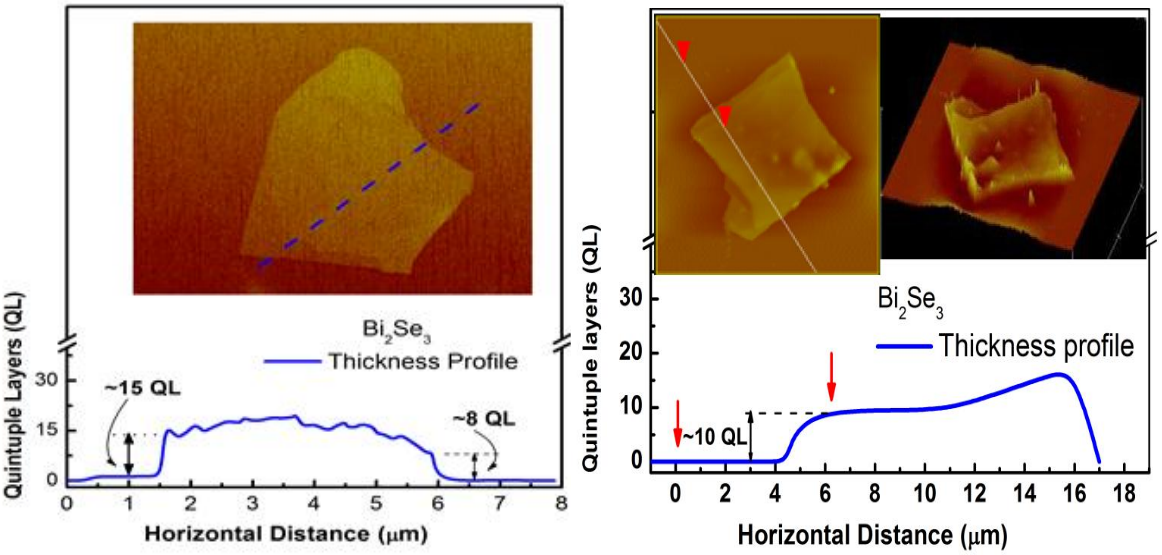

Figure 4.4: AFM images of FQL of Bi_2Se_3. Surface variation of the same sample is shown; the inset shows the actual scan area. Reprinted with permission from K. M. F. Shahil, M. Z. Hossain, V. Goyal and A. A. Balandin, "Micro-Raman Spectroscopy of Mechanically Exfoliated Few-Quintuple Layers of Bi_2Te_3, Bi_2Se_3 and Sb_2Te_3 Materials" *Journal of Applied Physics* (2012), © 2012 American Institute of Physics.

The thickness of the films was measured along the line scan (see insets to the figures). The thickness profile is re-plotted (Figure 4.4 (a)) showing an 8-nm (~8 quintuple) step with respect to the substrate. The surface profile shows a variation from 8 quintuple to 15 quintuple. In Figure 4.4 (b) another AFM image of Bi_2Se_3 is presented with the height profile and more uniform surface. Inset shows the line scan and top view of the film surface variation.

In Fig. 4.5 we present a typical AFM height profile of FQL Bi_2Te_3 film, which starts at zero height (substrate) goes to the thick (~40 nm) region and then falls back to the thin (~4 nm) region, which corresponds to a four-quintuple layer. The inset shows the actual scan area.

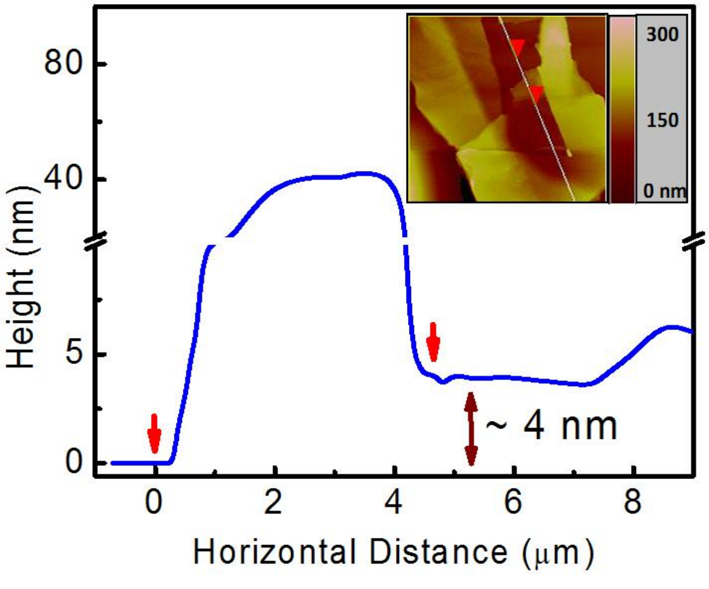

Figure 4.5: AFM measured profile of the exfoliated Bi_2Te_3 film showing a region with four quintuples. The inset is an AFM image of the scanned area with the red markers indicating the position of the tip, which correspond to the points in the height profile marked by the red arrows. Reprinted with permission from K. M. F. Shahil, M. Z. Hossain, D. Teweldebrhan, and A. A. Balandin, *Appl. Phys. Lett.* **96**,153103 (2010), © 2010 American Institute of Physics.

Through a series of optical, SEM, AFM investigation, we prepared several atomically thin FQL films for further Raman measurement. Next section, we will discuss the detail instrumentation of Raman Spectroscopy.

4.3 Raman Spectroscopy: Experimental Setup

4.3.1 Instrumentation

The Raman spectrometers today now use commercially available lasers and charge-coupled device (CCD) cameras in contrast to the instrumentation first used for spectroscopic study of scattered light in 1928 by Landsberg and Mandelstam, a mercury lamp and a quartz spectrograph.

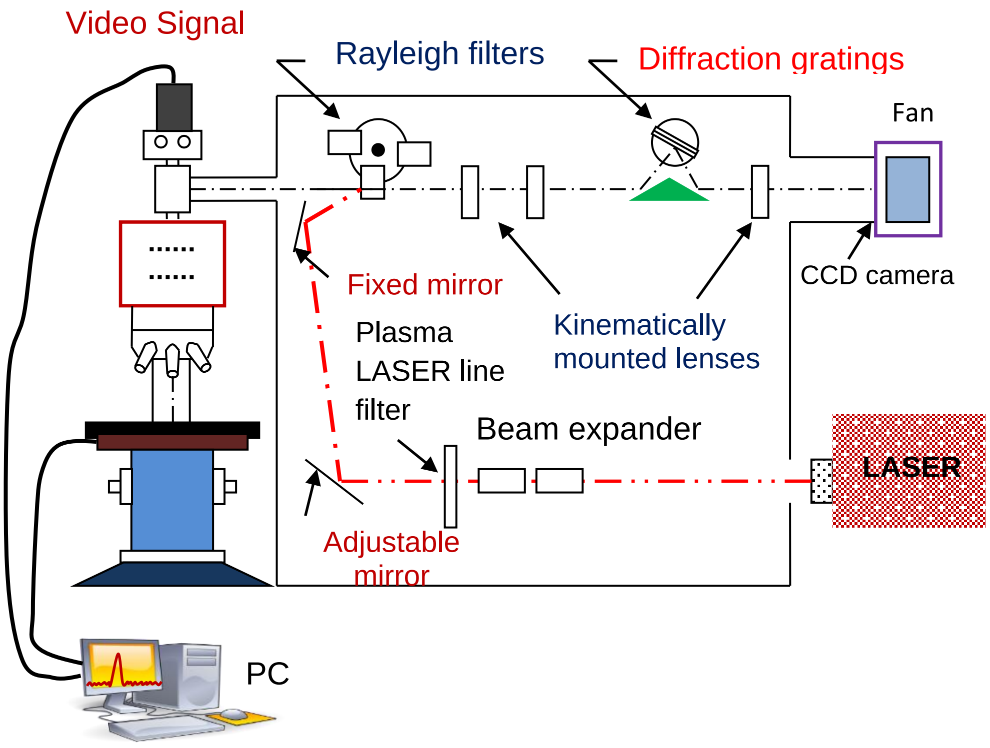

Figure 4.6: Schematic diagram of Raman Microscope system.

Early work in Raman spectroscopy instrumentation focused on improved light sources. Various forms of mercury lamps were implemented in the 1930s and 1940s. In the early 1960s came the development of lasers. This marked a significant improvement which fulfilled the requirement of light source monochromaticity. The micro-Raman spectroscopy system consists of a spectrograph with three major components as shown in the schematic diagram of Fig. 4.6.

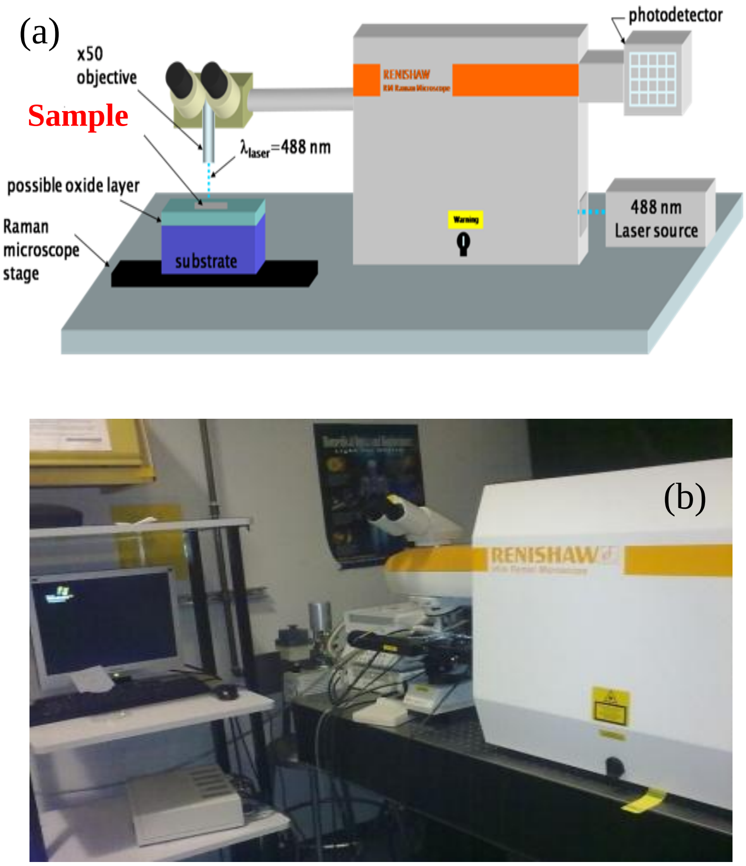

Figure 4.7: (a) Renishaw Raman microscope system used for Raman measurement. (b) Photograph of the Raman instrumentation system in the Nano device laboratory, UCR.

They are the excitation source, light detector, and a light collection and delivery system. With the advent of the laser and more sophisticated photodetection schemes, far superior Raman spectroscopy systems have been developed. The excitation source is almost exclusively a laser, CCD camera for detection, and optical microscope for light collection and delivery. The image and original photograph of Renishaw Raman microscope used for Raman spectroscopy in this dissertation are shown in Fig. 4.7.

4.3.2 Light Sources and Detection

The average power from the excitation source needed for Raman spectroscopy can range from about 3-10 mW [9] depending on the system. Although increasing the laser power can increase the Raman scattering intensity, this excessive heat can, in some cases, damage the sample due to local heating. The light source should be monochromatic at least to the point where its linewidth is much lower than the width of the Raman lines in the Raman spectrum, which is generally around 1 to 10 cm^{-1}[9]. In selecting an appropriate laser wavelength for non-resonance Raman spectroscopy work, one important criterion is that there are no absorption bands for the sample. However, for resonance Raman spectroscopy work, the laser wavelength is deliberately chosen to be within the absorption band of the sample.

The light detection system includes a slit, diffraction grating, mirror, and detector. The slit limits the light that enters the detection system of the spectrometer so that it experiences diffraction, which increases as the slit is narrowed, acting as a point source.

After passing through the slit, it travels to a recollimating lens and then onto a diffraction grating. The diffraction grating consists of many parallel and closely spaced (similar to that of the light's wavelength) slits that separates the light into its constituent wavelengths. Selected components of the light from the diffraction grating are directed onto a focusing lens based on the number of and spacing between slits as well as the angle between the diffraction grating and the incident light. If the grating remains stationary with just one center wavenumber specified during a measurement, this is a static scan. For an extended scan, the grating is rotated so different and more center wavenumbers can be selected. From the focusing lens, the remaining light falls on the detector. Baffles decrease stray light in the system and a shutter controls the detector exposure time. Considering that the Raman signal is usually relatively weak, generally a micro-Raman spectroscopy system will use a cooled CCD camera due to its inherent low noise features. The cooling system can implement something as simple as a fan or as elaborate as a liquid nitrogen system, depending on the requirements for low noise.

4.3.3 Rayleigh Scattering Filters

In addition with the Raman spectra i.e. inelastic scattering of light, there is also elastically scattered light which is called the Rayleigh scattering. In a Raman spectroscopy system, this light which is at the same frequency as the excitation laser light needs to be rejected. A variety of filters used to reject light of the same frequency as the excitation source (Rayleigh or elastic) can be found in a Raman spectroscopy system. It is important to remove this elastically scattered light especially since its intensity is about 10^7 times greater than the weak Raman signal. Edge filter and notch filters are some of the Rayleigh filters which reject the Rayleigh scattered light and allow only the Raman scattered light to pass through. Edge filter is a holographic filter which removes the Rayleigh scattered light while allowing Raman scattered light to pass only on the Stokes shifted side of the Rayleigh line. The notch filter rejects the Rayleigh scattered light while allowing the Raman scattered light to pass as close to it as 50 cm^{-1} on both sides of the Rayleigh line.

4.3.4 Objective Lenses

Objective lenses are used to focus the laser light on the sample and also define the sampling volume of the material. The spot size is the size of the spot on the sample due to the laser and describes the smallest distance that can be resolved by the Raman spectrometer system. This value depends both on the excitation laser's wavelength and the numerical aperture of the objective lens. When light passes uniformly through a small aperture, it is diffracted and subsequently produces an Airy pattern. The lateral resolution will then be the radius of the Airy disk. For an objective lens with numerical aperture, NA, the spot size, s, can be calculated with the following equation

$$s = \frac{0.61 \times \lambda_{laser}}{NA} \tag{4.1}$$

It is desirable to have a small spot size for high lateral resolution. This can be achieved by using an objective lens with a high NA and a shorter laser wavelength. The spot sizes available for the Renishaw Raman Microscope have been calculated using (4.1) and their values tabulated in Table 4.1. The axial resolution is determined by the microscope's depth of field and can be approximated by the equation below when the sample is measured in air [10]

$$R_{axial} = \frac{\lambda}{NA^2} \tag{4.2}$$

Table 4.1: Estimated spot sizes

Objective	Type	λ_{laser} (nm)	NA	S(μm)
×5	Visible	488	0.12	2.48
×10	Visible	488	0.40	0.74
×50	Visible	488	0.75	0.40
×40	Near UV	325	0.32	0.40
×50	Near UV	325	0.50	0.40
×50 LWD	Visible, LWD	488	0.50	0.60

4.3.5 Analysis Techniques of Raman Spectroscopy

We can produce one, two and three dimensional spectra with Raman Spectroscopy. One-dimensional spectra are usually sufficient for homogeneous samples. One point is illuminated and a spectrum is taken at that point for one dimensional measurement. Raman shift is determined by measuring the wavelength of the scattered light via the spectrograph.

The Raman shift (cm^{-1}) is calculated with the following equation

$$\Delta\upsilon = \upsilon_{Laser} - \upsilon_{Raman}(cm^{-1}) \text{ ,} \qquad (4.3)$$

where ν is the wavenumber.

We can rewrite Eqn. 4.3 in terms of wavelength, λ, as follows

$$\Delta\upsilon = \frac{10^7}{\lambda_{laser}} - \frac{10^7}{\lambda_{Raman}}(cm^{-1}), \qquad (4.4)$$

For a two-dimensional mapped spectrum, a software-controlled motorized stage moves the sample with respect to the laser in two directions, providing a two-dimensional map of the Raman spectra. There are a few methods for obtaining a three-dimensional Raman spectrum. One method is by incorporating lasers of different wave- lengths into the measurement, with higher wavelengths penetrating deeper into the sample. A three-dimensional Raman mapped spectrum is produced through a combination of this depth profiling along with the lateral Raman maps. A second approach uses a confocal microscope so that raising or lowering the stage changes the depth profile. The software-controlled motorized stage of the Renishaw Raman microscope has this capability. A third technique is to successively remove a layer from the sample followed by the capture of a Raman spectrum in order to compile depth profile information. Another available technique is Raman imaging. The 1-D, 2-D and 3-D mappings described above are types of Raman point imaging. Line focus imaging measures Raman spectra from lines instead of points. The resulting data consists of spectra from individual points on the line sampled simultaneously. The line can then be moved to a new position and a mapping produced consisting of lines instead of points. Since this type of Raman measurement technique results in lower laser powers, it is good to use on samples where laser damage is an issue.

4.4 Summary

The chapter describes in detail the sample preparation and characterization done prior to Raman measurement. The experimental set up of Raman measurement is described. The analysis procedure and theoretical formalism of Raman measurement are also presented in the chapter. In the next chapter, detail experimental results on Raman measurement of TIs will be presented.

References

[1] K. S. Novoselov, A. K. Geim, S. V. Morozov, D. Jiang, M. I. Katsnelson, I. V. Grigorieva, S. V. Dubonos and A. A. Firsov, *Nature* **438**, 197-200 (2005).

[2] K. S. Novoselov, A. K. Geim, S. V. Morozov, D. Jiang, Y. Zhang, S.V. Dubonos, I. V. Grigorieva and A. A. Firsov, *Science* **306**, 666 (2004).

[3] A. A. Balandin, S. Ghosh, W. Bao, I. Calizo, D. Teweldebrhan, F. Miao and C. N. Lau, *Nano Letters* **8**, 902 (2008); S. Ghosh, I. Calizo, D. Teweldebrhan, E. P. Pokatilov, D. L. Nika, A. A. Balandin, W. Bao, F. Miao, and C. N. Lau, *Applied Physics Letters* **92**, 151911 (2008).

[4] D. L. Nika, S. Ghosh, E. P. Pokatilov, A. A. Balandin, *Appl. Phys. Lett.* **94**, 203103 (2009); D. L. Nika, E. P. Pokatilov, A. S. Askerov and A. A. Balandin, *Physical Review B* **79**, 155413 (2009).

[5] D. Teweldebrhan, V. Goyal and A. A. Balandin, *Nano Lett.* **10**, 1209 (2010). D. Teweldebrhan, V. Goyal, M. Rahman and A. A. Balandin, *Appl. Phys. Lett.* **96**, 053107 (2010).

[6] M. Z. Hossain, S. L. Rumyantsev, D. Teweldebrhan, K. M. F. Shahil, M. Shur, A. A. Balandin, *Physica Status Solidi (A) Applications and Materials* **208**, 1, 144-146 (2011). M. Z. Hossain, S. L. Rumyantsev, K. M. F. Shahil, D. Teweldebrhan, M. Shur, A. A. Balandin, *ACS Nano* **5** (4), 2657-2663 (2011).

[7] K. M. F. Shahil, M. Z. Hossain, D. Teweldebrhan, and A. A. Balandin, *Appl. Phys. Lett.* **96**, 153103 (2010).

[8] K. M. F. Shahil, M. Z. Hossain, V. Goyal, and A. A. Balandin, *Journal of Appl. Phys*. (2012).

[9] M. Sushchinskii and V. Gorelik, *Journal of Applied Spectroscopy* **38**, 80-93 (1983).

[10] A. E. Conrady, *Applied Optics and Optical Design*, Part 2. Dover Publications, ISBN-10: 0486670082, New York (1992).

Chapter 5

Results and Discussions: Raman Nanometrology

5.1 Introduction

This chapter* describes the experimental results on micro-raman spectroscopy of topological insulators (TIs) in detail. The discussion covers detailed Raman spectra analysis of all three quasi 2D materials used in this study. The Raman spectra were collected at room temperature using a Renishaw RM2000 micro-Raman spectrometer fitted with an argon ion (Ar^+) LASER. An upgraded Renishaw in Via micro-Raman spectrometer RM 2000 was used for this study.

---

* Part of this chapter has been excerpted with permission from the papers by K. M. F. Shahil, M. Z. Hossain, D. Teweldebrhan, and A. A. Balandin, “Crystal symmetry breaking in few-quintuple Bi_2Te_3 films: Applications in nanometrology of topological insulators” *Appl. Phys. Lett.* **96**,153103 (2010), © 2010 American Institute of Physics and K. M. F. Shahil, M. Z. Hossain, V. Goyal and A. A. Balandin, “Micro-Raman Spectroscopy of Mechanically Exfoliated Few-Quintuple Layers of Bi_2Te_3, Bi_2Se_3 and Sb_2Te_3 Materials” *Journal of Applied Physics* (2012), © 2012 American Institute of Physics.

The settings for each Raman measurement include a spectral scan range of 50-250 cm^{-1}, detector time of 10 seconds, and 4 accumulations at optimum power. Some of the spectra of these particular measurements were fitted usinga Lorentzian line shape and a linear baseline model.

5.2 Optimum Laser Power Selection

In this study, all Raman spectra were taken at room temperature with laser light λ=488 nm and λ=633 nm recorded in the backscattering configuration through a 50× objective. With the 1800 lines/mm grating at 488 nm excitation and picking off the high resolution (-1 order) we can have the “hard-ware” spectral resolution of 1.35 cm^{-1} (~1 cm^{-1}). It was software-enhanced to 0.5 cm^{-1} so that we were able to see the difference between peaks (with plotted Lorentzians) down to approximately ~0.5 cm^{-1}. At the 633 nm excitation, the corresponding value of the spectral resolution was 0.63 cm^{-1}.

The Raman spectroscopic studies of thin films made from these materials are complicated due to the local heating effects since the materials have very low thermal conductivity and melting temperature [1]. For example, Bi_2Te_3 has very low thermal conductivity of 1.5 W/mK along the cleavage plane and 0.6 W/mK along the vander waals bonding direction [2]. It has also a low melting point of 573 °C. So these Raman spectra are taken at very low excitation power to avoid local heating. The maximum excitation power of the Ar + laser with the wavelength of 488 nm used in this study was 10 mW. Approximately half of the excitation power reaches the sample surface after transmission through the optical system. The local laser-induced heating produces melting or oxidation of FQL films [1, 3], that makes it difficult to get meaningful Raman spectra. On the other hand, the measurement taken at insufficient excitation power produces low signal to noise (S/N) ratio since the Raman spectra of these low-bandgap materials generally show the lower Raman count owing to their metallic behavior. From the trial-and-error studies we established that the optimum excitation power in our setup was ~0.25 mW on the sample surface consistent. It provided a good signal-to-noise (S/N) ratio without damaging the FQL samples.

5.3 Non-resonant Raman Spectra: Bulk Bi_2Te_3

We first performed analysis of Raman spectrum of exfoliated bulk Bi_2Te_3 film. Bi_2Te_3 is a semiconductor which at room temperature belongs to the space group $R\bar{3}m(D_{3d}^5)$ [4] and presents four Raman active modes. Kullmann *et al.* [5] successfully reported measured four expected Raman wave numbers for bulk sample shown at Table 5.1. All four Raman modes of Bi_2Te_3 are detected as shown in Figure 5.1. To investigate LASER heating effect a spectra taken at higher LASER power is shown in the same figure. The plot shows Raman spectra taken for two different bulk Bi_2Te_3 sample at 0.25 mW excitation power. For comparison a Raman spectra of bulk film taken at higher excitation LASER power is plotted in the same figure. The spectra shows arbitrary signature with high intensity.

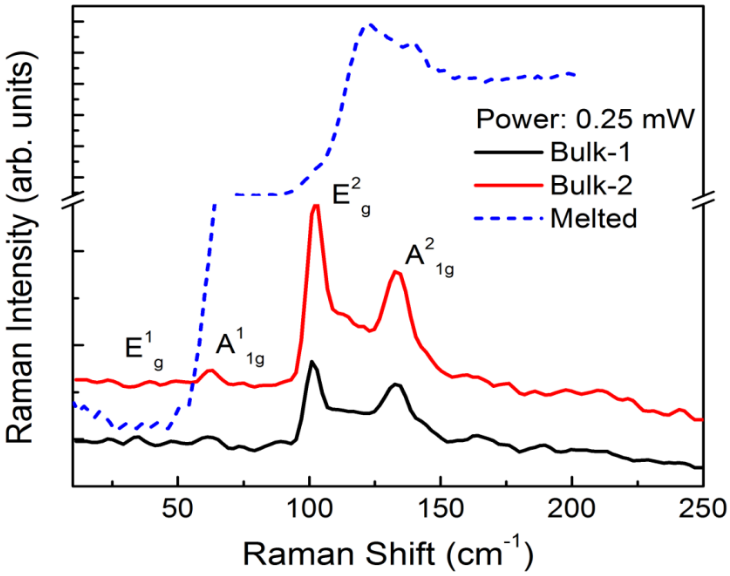

Figure 5.1: Raman spectra of bulk bismuth telluride crystals. Informative band in the spectra of Bi_2Te_3 atomic film is recorded at very low excitation power level. Spectra taken at higher LASER power is shown in the same image.

These peaks are very close to the previously measured and assigned Raman peaks of Bi_2Te_3 bulk sample [4-7]. Each of the E_g and A_{1g} modes are two-fold degenerate. In the twofold degenerate E_g modes, the atoms vibrate in the basal plane; while in the two A_{1g} modes the atoms vibrate along the trigonal direction $C_{H.}$ [4]. The A^1_{1g} and Eg^1 modes occur at lower frequencies than the A^2_{1g} and E_g^2 modes. The letter modes, where the outer Bi and $Te^{(1)}$ atoms move in opposite phase, will mainly be affected by forces between Bi and $Te^{(1)}$ atoms. In the Eg^1 and A^1_{1g} modes the outer Bi-Te $^{(1)}$ pairs move in phase. Thus the Bi-Te $^{(2)}$ bonding forces will be primarily involved in these vibrations. In crystals with inversion symmetry, an infrared-active phonon (A_{1u}) must be odd parity while a Raman-active phonon (Eg, A_{1g}) must be even parity under inversion [8] (see table

3.3). It is evident from figure 5.1 that the odd-parity phonons (IR active) do not show up in Raman spectra for bulk samples as long as crystal retains its inversion symmetry.

5.4 Non-resonant Raman Spectra: FQL of Bi_2Te_3

5.4.1 Crystal Symmetry Breaking

We now turn to the analysis of Raman spectrum of exfoliated few quintuple layer (FQL) Bi_2Te_3 film. In principle, one can define a nanostructured material as thin film with at least one dimension ≤ 100nm and that is single crystalline. For Raman studies of thin crystalline Bi_2Te_3 film, we choose several samples having different thickness (sub 10~100 nm) confirmed by a combination of Optical, SEM and AFM as described in the previous chapter.

The measured non-resonant Raman spectra of Bi_2Te_3 FQLs are shown in Figure. 5.2. The spectra are recorded under 488-nm excitation. The observed four optical phonon peaks are identified (see Table 5.1). The frequencies of all these four zone-center regular Raman active modes are Eg^1 (TO) ~ 1.02 THz, A^1_{1g} (LO) ~ 1.81 THz, Eg^2 (TO) ~ 3.02 THz and A^2_{1g} (LO) ~ 4 THz [9]. These peaks are very close to the previously measured and assigned Raman peaks of Bi_2Te_3 bulk sample [4, 6, 7, 9]. In addition to these peaks another peak, A_{1u}= 116.7 cm^{-1} is found for the atomically thin FQL Bi_2Te_3 films. The A_{1u} mode of the longitudinal optical (LO) phonons at 116.7 cm^{-1} is IR active and corresponds to the zone-boundary phonon (Z point) of the frequency ~3.57 THz [4, 9].

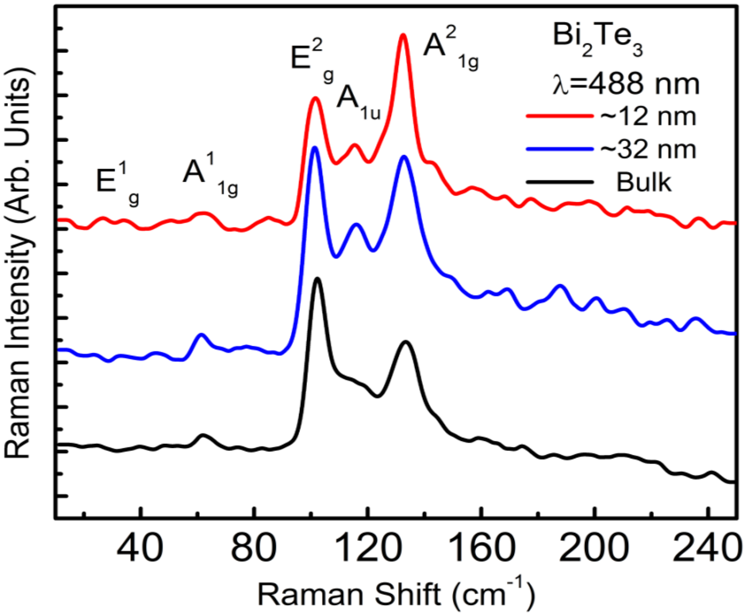

Figure 5.2: Raman spectrums of Bi_2Te_3 FQLs on Si/SiO_2 substrate. Spectra are taken from the spots with different thicknesses (~12 nm and ~32 nm) to demonstrate reproducibility. The displacement patterns of A_{1u} phonon mode are shown in inset.

According to the theory [8], in crystals with the inversion symmetry, the IR-active modes like A_{1u} must be odd parity while the Raman-active modes E_g, A_{1g} must be even parity under inversion. The phonon displacement vector Q of an odd-parity phonon (IR) changes the sign under inversion, hence the Raman tensor ($d\chi / dQ$) of the odd-parity phonons in the centrosymmetric crystals must vanish [8]. Thus, the odd-parity phonons (A_{1u}, E_u) do not show up in Raman spectra of bulk samples [5, 7] as long as the crystal retains its symmetry. We attribute the appearance of A_{1u} mode in FQL to breaking of the crystal symmetry in the third dimension due to the limited thickness of FQL and presence of the interfaces.

Table 5.1 Raman Peaks in FQL Bi_2Te_3

Bi_2Te_3	**E^1_g**	**A^1_{1g}**	**E^2_g**	**A_{1u}**	**A^2_{1g}**	**Comments**
12 nm	35.2	62.2	101.4	115.9	132.8	This work
32 nm	34.5	61.1	101.4	115.7	132.9	
Bulk		62.5	102.5		133.73	
Bulk	36.5	62.0	102.3	-	134.0	Ref. [5]
Bulk	-	62.3	103.7	-	134.2	Ref. [7]

We estimated the light penetration depth in our samples to be ~60–90 nm for 488 nm laser depending on the carrier concentration. One can calculate the penetration depth from the equation $\delta = 1/\sqrt{\pi f \sigma \mu}$, where f is the frequency of light, σ is the electrical conductivity of the materials and μ is the magnetic permeability. We assumed σ in the range from 1.1×10^5 S/m to 5×10^4 S/m [1] and the calculated the penetration depth to be from ~60 nm to 90 nm at 488-nm laser light. This value correlates well with thickness H when the 117 cm^{-1} peak appears in FQL's spectrum. The onset of the A_{1u} peak at the moment when the penetration depth becomes equal to that of the FQL thickness suggests that the loss of the translation symmetry at the FQL – substrate interface is the main mechanism of the crystal symmetry breaking.

Our results are in agreement with a recent computational study [10], which found that the crystal symmetry breaking in Bi_2Te_3 thin films should lead the Raman activity of

$A_{1u.}$ The a*b initio* calculation, which included the spin-orbit (SO) coupling, found that the single quintuple-layer films and the bulk materials have different symmetries [10]. The film has P-3m^{1}symmetry while the bulk has R-3m symmetry. It was also noted that because of their limited thickness the films have no translational symmetry in the third dimension. The loss of the translational symmetry in films was considered to be one of the crystal breaking mechanisms. Another possible mechanism for very thin films identified in Ref. [10] was a strong inharmonic potential that exists around Bi atoms in the single quintuple films, which can be one of the symmetry breaking mechanisms caused by SO interactions. We also note that a single quintuple is inversely symmetric. Breaking of the individual quintuple layers to sub-quintuples, which in principle is possible, particularly on the film surface, could be an extra mechanism leading the crystal symmetry breaking and appearance of A_{1u} peak. The effect from such sub-quintuple breaking will become stronger as the thickness of the films and, correspondingly, the Raman interaction volume, decreases.

5.4.2 Raman as a Nanometrology Tool

As evidenced from ARPES measurements, an energy gap exists below a thickness of six quintuple layers of Bi_2Se_3 [11] and the films preserve gapless surface states when the thickness is above six QL. On the other hand, a significant improvement in thermoelectric applications could be achieved in 2D structure where electrons and holes are strongly confined in one or two dimensions.

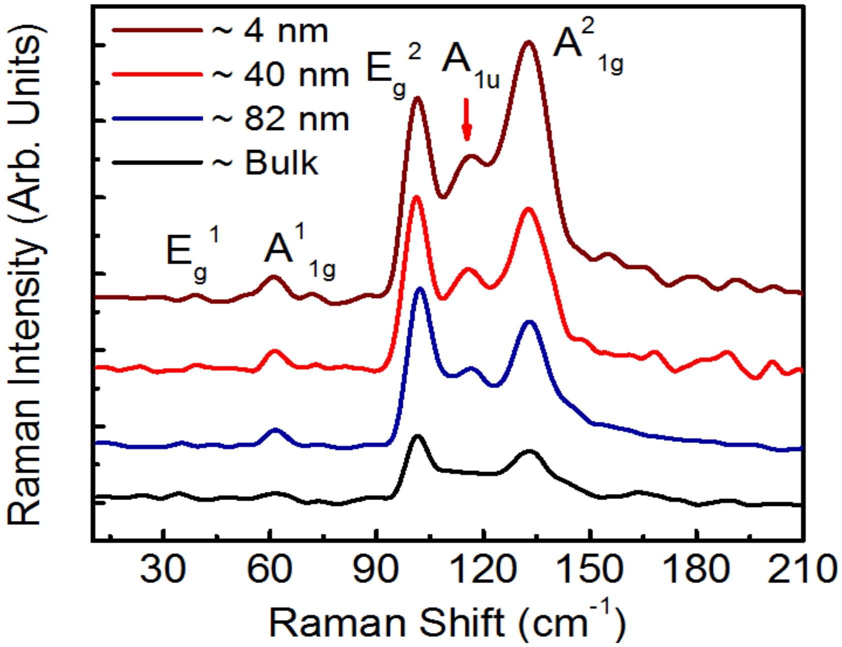

Figure 5.3: Raman spectra of reference bulk Bi_2Te_3 crystal and few-quintuple films. Note that A_{1u} mode at ~117 cm^{-1} becomes Raman active only in the thin films. Reprinted with permission from K. M. F. Shahil, M. Z. Hossain, D. Teweldebrhan, and A. A. Balandin, “Crystal symmetry breaking in few-quintuple Bi 2 Te 3 films: Applicationsin nanometrology of topological insulators”, *Appl. Phys. Lett.* **96**,153103 (2010), © 2010 American Institute of Physics.

Fig. 5.3 presents Raman spectra of bulk Bi_2Te_3 crystal and three FQLs as their thickness *H* decreases from ~82 nm to ~4 nm. The frequencies of the observed peaks and their assignment are listed in Table 5.2 together with previously reported data for bulk Bi_2Te_3.

Table 5.2: Raman peaks in Bi_2Te_3 crystals and few-quintuple films

Bi_2Te_3	E_g^1	A^1_{1g}	E_g^2	A_{1u}	A^2_{1g}	$I(A^2_{1g})/ I(E_g^2)$	$I(A_{1u})/ I(E_g^2)$	**Comments**
Bulk	34.4	62.1	101.7	-	134.0	0.75	-	This work
82 nm	35.8	61.5	101.9	116.9	132.7	0.83	0.62	
40 nm	38.9	61.3	101.3	116.2	133.0	0.92	0.76	
4 nm	38.9	60.9	101.4	116.7	132.9	1.30	0.86	
Bulk	36.5	62.0	102.3	-	134.0	-	-	Ref. [5]
Bulk	-	62.3	103.7	-	134.2	-	-	Ref. [7]

One intriguing observation from Fig. 5.3 is an evolution of the $I(A^2_{1g})/I(E_g^2)$ ratio as one goes from bulk crystal to FQLs. In bulk, the measured intensity of in-plane vibrations $I(E_g^2)$ is higher than that of the out-of-plane vibrations $I(A^2_{1g})$, which is in agreement with literature for bulk Bi_2Te_3 [4-7]. But in the atomically thin films the intensity of the out-of-plane vibrations increases with decreasing thickness and at some *H* exceeds that of $I(E_g^2)$. In FQL with *H*=4 nm, the ratio $I(A^2_{1g})/I(E_g^2)>1$. So we calibrated the intensity ratio of highest-frequency A_{1g} (i.e. $A^2_{1g} \sim 4$ THz) mode to that of Eg^2 mode (Eg^2 the most pronounced feature in the spectrum) shown in Figure 5.4. The calculated intensity ratios are listed in Table 5.2.

At this point, it is reasonable to assume that the out-of-plane vibrations will be less restrained in a four-quintuple film than in bulk, which may lead to larger amplitudes of vibrations. This hypothesis is supported by comparison of the Raman spectra recorded from the suspended and supported portions of FQLs.

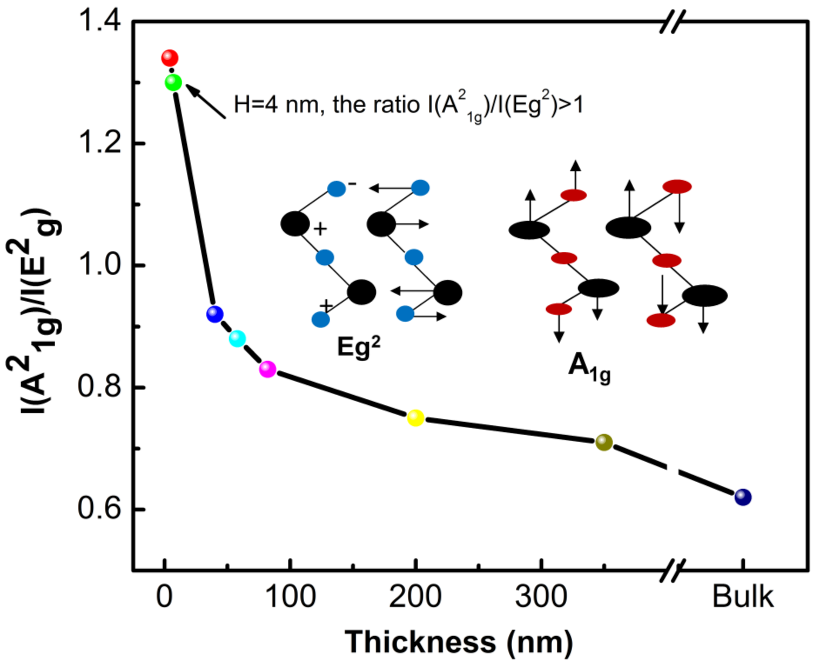

Figure 5.4: Calibrated Intensity ratio of Out of plane mode (A^2_{1g}) to that of in plane mode (E_g^2). The inset is the schematic of vibrational modes. Reprinted with permission from K. M. F. Shahil, M. Z. Hossain, V. Goyal and A. A. Balandin, "Micro-Raman Spectroscopy of Mechanically Exfoliated Few-Quintuple Layers of Bi_2Te_3, Bi_2Se_3 and Sb_2Te_3 Materials" Journal of Applied Physics (2012), © 2012 American Institute of Physics.

We also calculate the ratio of the intensity of A_{1u} mode to that of Eg^2 and found increasing with decrease of oxide thickness which implies that the appearance of infrared mode is not for substrate effect rather than due to periodicity breaking (see table 5.2). Since E_g^2 (TO) is a regular BZ-center peak originating in the "bulk" of the film, the $I(A_{1u})/I(E_g^2)$ ratio increases with decreasing *H* because of the decreasing interaction volume $V = S \times H$ (S is the cross-sectional area of the laser spot), which defines $I(E_g^2)$ for H smaller than the light penetration depth in a given material.

According to a theoretical calculation [10], there is another infra-active mode, A_{2u} around ~3.97 Thz. This peak may also become Raman active due to the symmetry breaking. However, it is difficult to distinguish these two peaks experimentally because they are too close to each other. The strength of the Raman intensity of A^2_{1g} mode (~4 THz) can increase due to the activation of another IR mode, which is close to the A^2_{1g} mode frequency. In this case, a combination of two Raman-active (A^2_{1g} + A_{2u}) modes, with an average frequency of ~4.03 THz will appear as the Raman signature around ~132 cm^{-1} with increased intensity.

The discussed modifications of the characteristic peaks in Raman spectra of FQL Bi_2Te_3 with the thickness create a basis for the use of micro-Raman spectroscopy as a nanometrology tool for characterization of these unique structures with the potential for practical applications.

5.5 Suspended Structures

Motivated by recent experiments on suspended graphene we transfer few atomic layer flakes of Bi_2Te_3 to the Si/SiO_2 wafers with pre-fabricated trenches. The examined flake is placed in such a way that it has a suspended region as well as region rested on Si/SiO_2 substrate. Here in Figure 5.5, the A_{1u} mode is showed up at ~117 cm^{-1} along with the three regular Raman peaks listed in Table 5.3. For suspended film, the out of plane mode (A^2_{1g}) is enhanced over in plane mode (Eg^2). We know that the intensity of Raman peak due to "out of plane" vibration depends on the scattering rate for charge impurities of the substrate. When suspended, there is no surface charge density, so low rate of scattering enhances the intensity of out of plane mode.

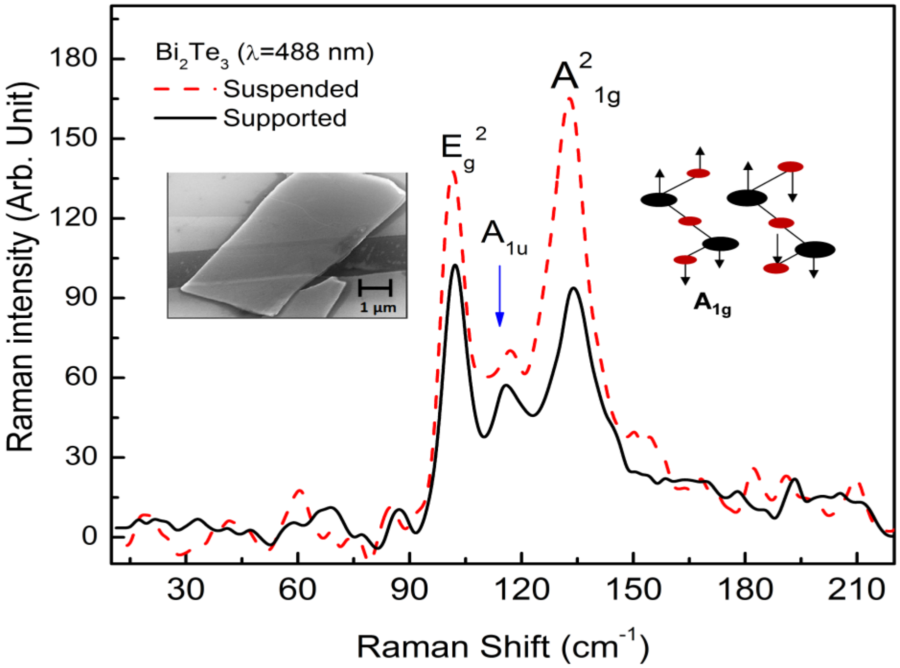

Figure 5.5: Comparison of Raman signature of suspended film with that of supported one. Here the out of plane mode is enhanced due to reduced scattering. Also the Raman band is red shifted due to strain effect. Inset shows a representative suspended FQL on S/SiO_2 wafer. Inset Reprinted with permission from K. M. F. Shahil, M. Z. Hossain, D. Teweldebrhan, and A. A. Balandin, *Appl. Phys. Lett.* **96**,153103 (2010), © 2010 American Institute of Physics.

Table 5.3 Raman modes of Suspended Structure

Bi_2Te_3	**A^1_{1g}**	**E_g^2**	**A_{1u}**	**A^2_{1g}**	**$I(A^2_{1g})/I(E_g^2)$**
Supported	62.9	103.0	119.5	134.2	0.93
Suspended	60.8	101.5	117.3	132.9	1.19

Another point to be noted that, for suspended structures all phonon modes are red shifted. This indicates either a small compression in the suspended region or, more likely, a small strain in the substrate region.

5.6 Non-resonant Raman Spectra: FQL of Bi_2Se_3 and Sb_2Te_3

We now turn to the analysis of Raman spectrum of FQL Bi_2Se_3 films. Figure 5.6 shows Raman spectra of Bi_2Se_3 FQLs taken in the geometry $z(xx)\bar{z}$ i.e. incident light shines along z- direction and both the incident and scattered light are polarized along x-direction. There are three characteristic peaks within the scanned frequency range: ~71 cm^{-1}, ~131 cm^{-1} and ~173 cm^{-1} which are identified in Raman spectra.

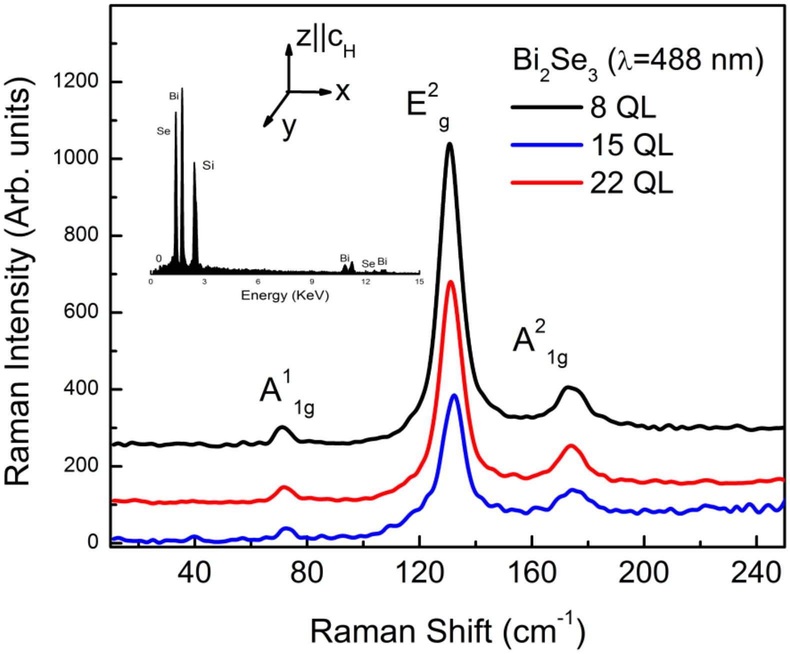

Figure 5.6: Raman spectra of Bi_2Se_3 FQLs in the 10-250 cm^{-1} region. Three spectra are taken at different thickness of the sample. The displacement patterns of Eg^2, A^1_{1g} and A^2_{1g} phonon modes are shown in inset. The incident LASER shines alone z direction and polarized along x direction.

From the selection rules given in Table 5.4 it follows that the peak at 131.5 cm^{-1} has to be assigned to the E^2_g mode whereas the other two (71 cm^{-1} and 171.5cm^{-1}) corresponds to A_{1g} mode. The observed frequencies are well comparable with the previously reported experimental and calculated phonon vibration modes of Bi_2Se_3 [4].

Table 5.4: Raman peaks in FQLs Bi_2Se_3 film

Thickness	**A^1_{1g}**	**E^2_g**	**A^2_{1g}**	**Comment**
~8 nm	70.6	131	173.4	This work
~15 nm	72.4	132	174.7	
~22 nm	71.5	131.2	174.2	
Bulk	72	131.5	174.5	Ref. 4
Calculated	67.5	121	157.5	

If polarization of x-direction is present ($z(xx)\bar{z}$ geometry), one will observe phonons denoted by A^1_{1g}, A^1_{2g} and E^2_g. If one measures scattered light with a polarization in the y direction, only Eg^2 will appear in the Raman spectrum [4]. This can be understood by considering the nature of the atomic displacements associated with the phonon modes. If a phonon mode A_{1g} is excited, the tensor implies that the polarization induced by the incident electric field $\xi_0 = (\xi_{x0}, \xi_{y0}, 0)$ has the same direction as ξ_0. So A_{1g} type phonon has $d\chi_{xy} / dQ = 0$. On the other hand, a phonon of the type E_g possesses displacements in both x- and y- directions i.e., in plane vibration. An incident electric field ξ_{x0} thus induces polarization changes in both directions and the scattered light contains polarization components in both these directions, i.e. $d\chi_{xx} / dQ \neq 0, d\chi_{xy} / dQ \neq 0$

.

For Bi_2Se_3 crystal, the Raman bands appear in higher frequency range than that of Bi_2Te_3. This is due to stronger bonding forces compared to Bi_2Te_3 and Sb_2Te_3. This fact is also supported by small atomic distances in Bi_2Se_3 [4]. Also “Se” atom is lighter than “Te” atom; when LASER interacts with the material “Se” atoms vibrate more strongly producing informative Raman bands to a higher frequency range. Another important observation is no IR mode is present in FQLs Bi_2Se_3 films as compared to Bi_2Te_3. According to reference 18, for Bi_2Te_3 both $E \perp C$ and E || C polarization conditions could be possible. But for Bi_2Se_3, only $E \perp C$ polarization (~ E_u mode) conditions on cleavage planes were possible. So, for Bi_2Se_3, only E_u mode conditions on cleavage planes are possible [4]. As this E_u mode is “in plane” vibration, so it does not show up when thickness of exfoliated Bi_2Se_3 goes down to few quintuple layers along C_H axis.

Let us discuss now the non-resonant Raman spectra of antimony telluride (Sb_2Te_3), which are shown in Figure 5.7. The calculated frequencies of the Raman active phonon modes for Sb_2Te_3 crystal reported by Sosso et al. [12] are also listed in Table 5.5. Comparing with calculated value [12], we can conclude that in Sb_2Te_3 FQL the peak at ~35 cm^{-1} corresponds to Eg^1 (TO), ~70 cm^{-1} corresponds to A^1_{1g} (LO), ~114 cm^{-1} corresponds to Eg^2 (TO) and ~165 cm^{-1} corresponds to A^2_{1g} (LO). The agreement with calculative data is overall acceptable.

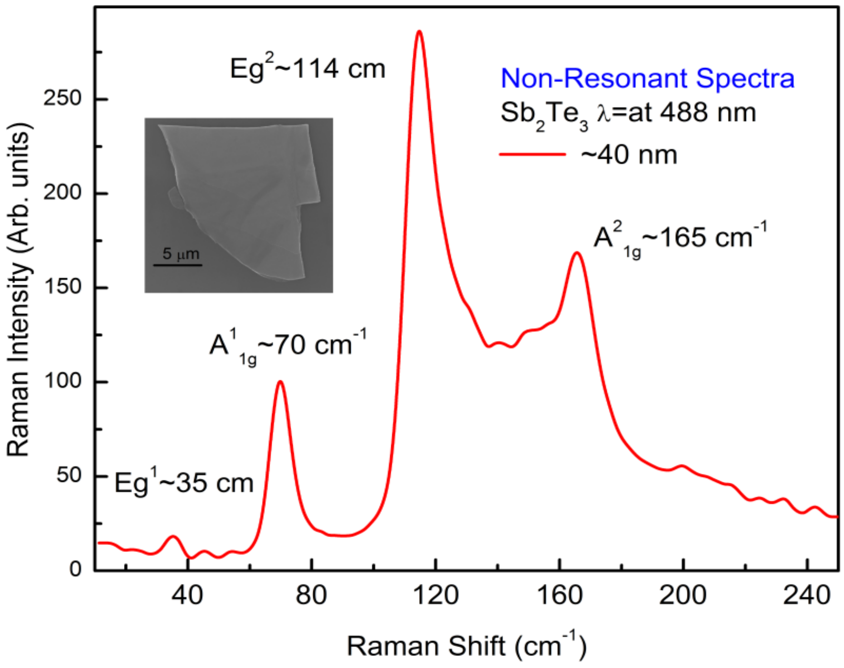

Figure 5.7: Informative Raman spectra of sub 40 nm Sb_2Te_3 at 488 nm LASER. Inset shows a SEM image of FQL Sb_2Te_3 flake. Reprinted with permission from K. M. F. Shahil, M. Z. Hossain, V. Goyal and A. A. Balandin, "Micro-Raman Spectroscopy of Mechanically Exfoliated Few-Quintuple Layers of Bi_2Te_3, Bi_2Se_3 and Sb_2Te_3 Materials" *Journal of Applied Physics* (2012), © 2012 American Institute of Physics.

Table 5.5: Raman peaks in FQLs Sb_2Te_3 film

Sb_2Te_3	**E^1_g**	**A^1_{1g}**	**E^2_g**	**A^2_{1g}**	**Comment**
Sub 40 nm	35.1	69.8	114.5	167.5	Our work
Calculated	46	62	113	166	Ref. 12

5.7 Resonant Raman Spectra

Raman spectroscopy is considered to be promising for highly sensitive detection if resonant Raman scattering (RRS) occurs. When the excitation line is tuned into an electronic absorption band, some of the Raman bands which are related to the electronic transition that is responsible for the absorption will be greatly enhanced. This means that equilibrium conformation of the molecule is distorted along the normal coordinate of the given Raman line in the transition from the ground to excited electronic state. Theoretically, a change in polarizibility, $(\alpha_{p\sigma})_{mn}$ due to electronic transition ($m \rightarrow e \rightarrow n$) can be written as [8]

$$(\alpha_{p\sigma})_{mn} = \frac{1}{h}\sum\left(\frac{M_{me}M_{en}}{\upsilon_{em}-\upsilon_0+i\Gamma_e}+\frac{M_{me}M_{en}}{\upsilon_{en}+\upsilon_0+i\Gamma_e}\right) \tag{5.1}$$

where m, n, e are electronic states, υ_{en} and υ_{em} are the frequencies corresponding to the energy differences between the states and incident laser beam of frequency υ_0. As υ_0 approaches υ_{em}, the denominator of the first term in the brackets of Eq. (5.1) becomes very small. Hence, this term ("resonance term") becomes so large that the intensity of the Raman band at $\upsilon_0 - \upsilon_{mn}$ increases enormously. This selectivity is important not only for identifying vibrations of this particular chromophore in a complex spectrum, but also for locating its electronic transitions in an absorption spectrum. Therefore RRS has a wide range of application including determination of electronic states. The obtained Raman scattering spectra of FQL Bi_2Te_3 and Bi_2Se_3 taken at 633 nm wavelength are shown in

Figure 5.8 (a,b). Raman spectra taken at 488 nm is also shown in the same figure for the comparison. Same polarization setup (i.e. $z(xx)\bar{z}$) and same conditions (i.e. accumulation time, laser power, and objective) were maintained for both 488 nm and 633 nm LASER.

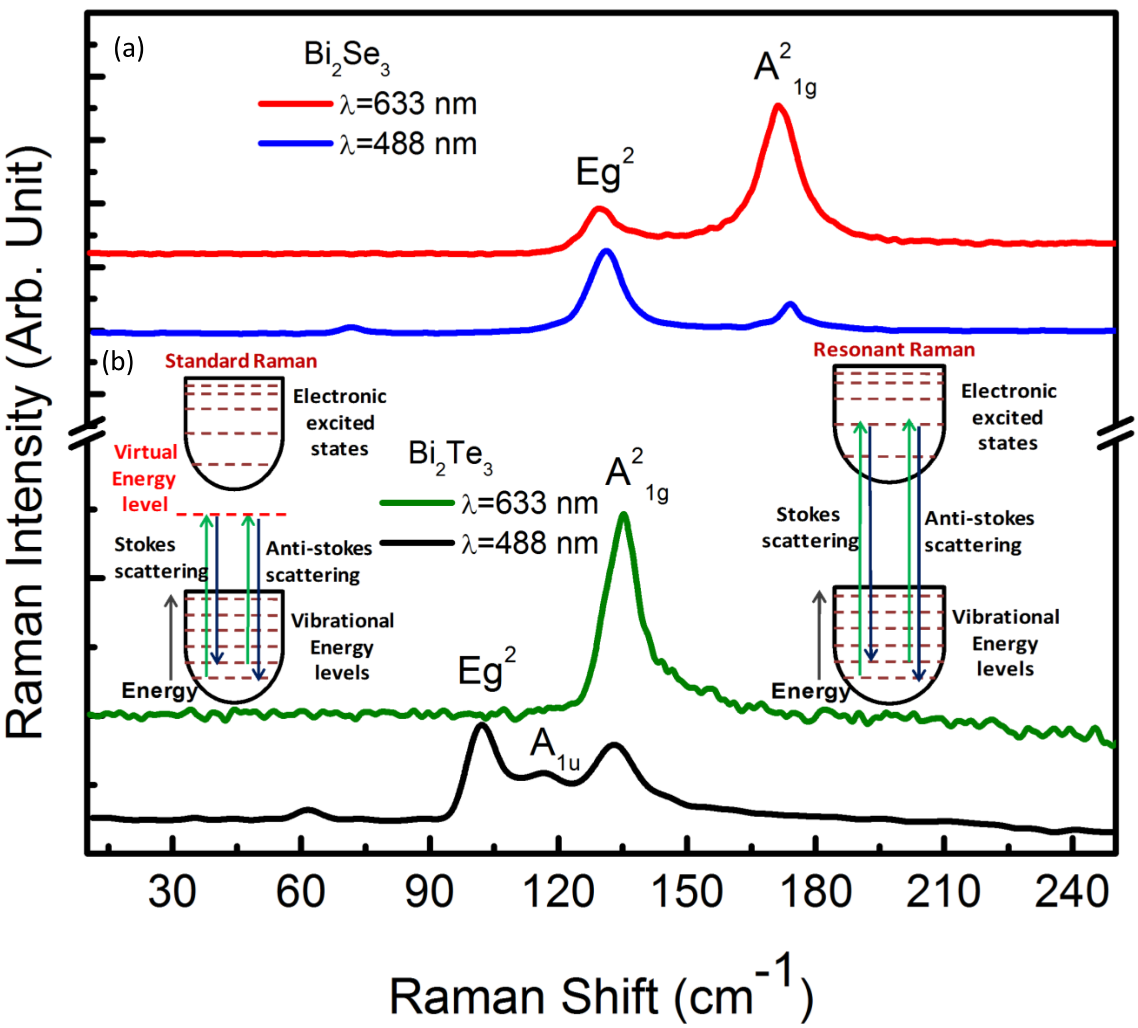

Figure 5.8: Resonant Raman spectra acquired at LASER excitations of 633 nm (1.96 eV) and non-resonant Raman spectra at 488 nm (2.54 eV) LASER is shown for comparison. (a) Bi_2Se_3 (b) Bi_2Te_3 Note that for non-resonant condition at 488 nm LASER, the TO phonon mode dominates. Reprinted with permission from K. M. F. Shahil, M. Z. Hossain, V. Goyal and A. A. Balandin, “Micro-Raman Spectroscopy of Mechanically Exfoliated Few-Quintuple Layers of Bi_2Te_3, Bi_2Se_3 and Sb_2Te_3 Materials” *Journal of Applied Physics*. XX (2012), © 2012 American Institute of Physics.

Strong resonance was observed as the excitation LASER energy (1.96 eV) creates a vibrational state near the electronic state of the band structure. This is exactly what is expected for both Bi_2Se_3 and Bi_2Te_3 since at Γ point there exists a conduction band (electronic excited state) which lies at 633 nm (~1.96 eV) above the valence band maximum (ground state) [13].

Another intriguing observation from Figure 5.8 is that at 488 nm (2.54 eV) the off-resonance excitations, the Eg (TO) mode is the dominant feature in the spectra, while at the resonance with a laser excitation at 633 nm (1.96 eV) the A1g (LO) becomes the dominant mode. For Bi_2Te_3 a strong evolution of $A^2{}_{1g}$ mode (LO) is observed in Figure 5.8 and no Eg^2 mode (TO) can be seen under the resonant condition, i.e. 633-nm laser light. Similarly, in the case of Bi_2Se_3, the intensity of $A^2{}_{1g}$ mode becomes larger than that of Eg^2 mode. This evolution is analogous to the one observed by some of us in ZnO nanocrystals [14-15], where at the resonant conditions the LO is dominant and no TO phonons are observed. The dominance of LO modes can be explained by an analysis of how these phonons couple to the electronic systems. The LO phonon-electron interaction is mediated via Frohlich interaction [16] and the intensity of the LO modes might be strongly enhanced. On the other hand, the Frohlich coupling cancels for E_g phonons. The properties of the longitudinal optical modes are of great interest because of the fact that their long range electrostatic field can couple and interact with electrons. This LO phonon-electron interaction can diminish the performance of optoelectronics devices [17] or, on the other hand, can be utilized in phonon engineering to create devices such as cascade lasers [18].

5.8 Substrate Effects

In order to extend the use of Raman spectroscopy as a thin film nanometrology tool, one needs to study how the Raman signatures of thin film are affected when it is placed on different substrates other than the regular SiO_2/Si. The knowledge of the substrate effects on Raman spectra is important for extending the application of micro-Raman spectroscopy as a nanometrology tool for characterization and device fabrication. Previously we reported that the Raman phonon peaks undergo modification when graphene is placed on other substrates due to changes in the nature and density of the defects, surface charges and different strength of the graphene–substrate bonding [19].

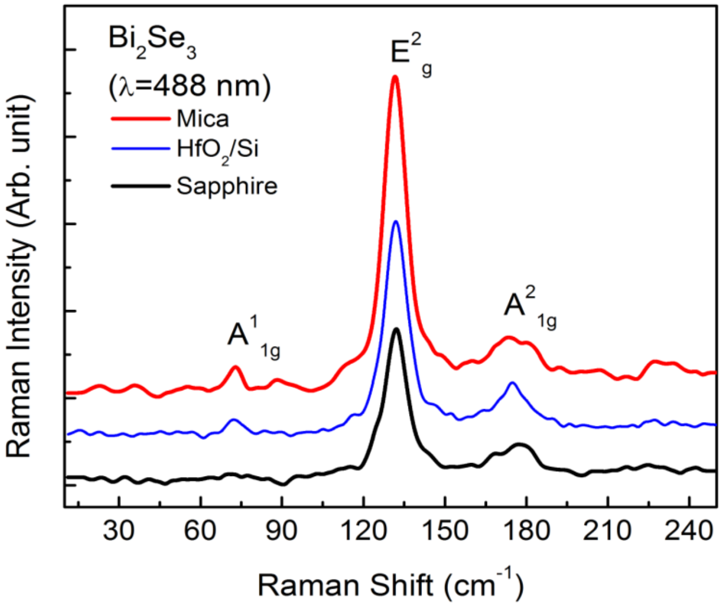

Figure 5.9: Raman spectra of Bi_2Se_3 FQLs on different substrates. Reprinted with permission from K. M. F. Shahil, M. Z. Hossain, V. Goyal and A. A. Balandin, "Micro-Raman Spectroscopy of Mechanically Exfoliated Few-Quintuple Layers of Bi_2Te_3, Bi_2Se_3 and Sb_2Te_3 Materials" Journal of Applied Physics (2012), © 2012 American Institute of Physics.

After taking Raman spectra from FQL on the standard SiO_2/Si substrate, we investigated Bi_2Se_3 placed on HfO_2/Si, sapphire, and Mica substrates. Figure 5.9 compares Bi_2Se_3 on different substrate (HfO_2/Si, MICA and Sapphire) at 488 nm LASER. For sapphire at 488 nm the A^2_{1g} mode shows a blue shift of 4 cm^{-1}. This could be due to compressive strain. However at 488 nm the A^2_{1g} mode splits. Previous Raman inspection of our group on graphene layers on glass also indicated that in some instances G peak was split into doublets [19, 20]. Random defects or charges on the surface may explain the doublets. It is also worthwhile to mention that, the adherence of FQL to different substrates was similar. This conclusion could be important for further investigation of topological insulator on different substrates.

Table 5.6: Raman peaks in FQLs Bi_2Se_3 film on different substrate

Substrate	**A_{1g}**	**E_g**	**A_{1g}**
SiO_2/Si	71.52	131.19	173.57
Mica	72.88	131.37	174.53
HfO_2/Si	71.95	131.7	174.96
Sapphire	-	133.3	177.05

Figure 5.10 shows Raman spectra of Bi_2Te_3 FQL on sapphire substrate. Here also A_{1u} mode is visible at 116 cm^{-1} for FGL film. Also as shown in the figure, the Raman modes of Bi_2Te_3 on Sapphire are blue shifted (~2 cm^{-1}) due to compressive strain

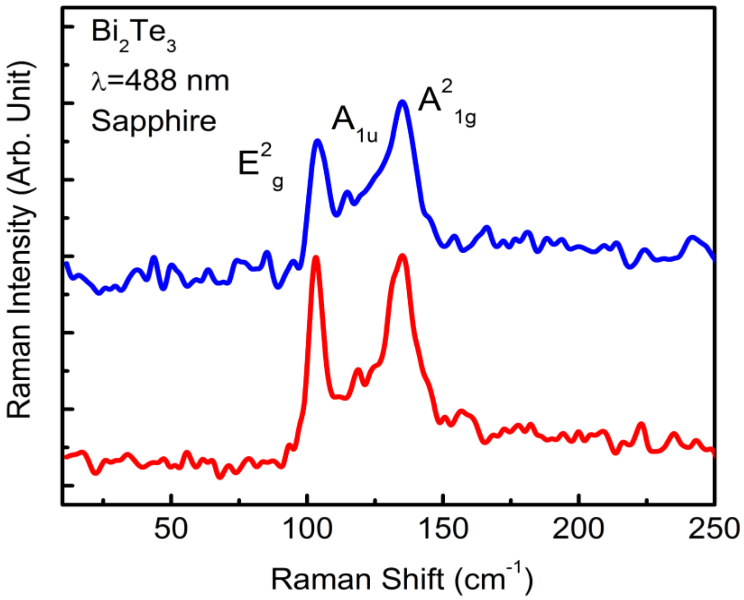

Figure 5.10: Raman spectra of Bi_2Te_3 FQLs on sapphire. Inset shows optical image of Bi_2Te_3 flakes on Sapphire substrate.

The knowledge of the substrate effects on graphene Raman spectra is important for extending the application of micro-Raman spectroscopy as a nanometrology tool for TI characterization and device fabrication.

5.9 Summary

We presented results of detail Raman studies of the few-quintuple-thick films of Bi_2Te_3, Bi_2Se_3 and Sb_2Te_3. The films were prepared by the "graphene-like" mechanical exfoliation from bulk crystals. We have shown how resonant Raman scattering by LO phonons can be used to analyze FQL Bi_2Te_3 and Bi_2Se_3 films. Tuning the incident photon energy into resonance with appropriate band gap energy allows the vibrational properties of that particular layer to be probed with a high degree of selectivity. The activation of non-Raman active IR mode found in relatively thin Bi_2Te_3 film is informative and could be used to identify few-quintuple films of high quality. The obtained results are important for further development of the topological insulator field.

References

[1] D. Teweldebrhan, V. Goyal and A. A. Balandin, *Nano Lett.* **10**, 1209 (2010). D. Teweldebrhan, V. Goyal, M. Rahman and A. A. Balandin, *Appl. Phys. Lett.* **96**, 053107 (2010).

[2] D. G. Cahill, W. K. Ford, K. E. Goodson, G. D. Mahan, A. Majumdar, H. J. Maris, R. Merlin, and S. R. Phillpo, *J Appl. Phys.* **93**,2,793 (2003).

[3] K. M. F. Shahil, M. Z. Hossain, D. Teweldebrhan, and A. A. Balandin, *Appl. Phys. Lett.* **96**, 153103 (2010).
K. M. F. Shahil, M. Z. Hossain, V. Goyal and A. A. Balandin, *J Appl. Phys.* (2012).

[4] W. Richter, H. Kohler and C. R. Becker *Phys stat. sol. (b)* **84**, 629 (1977).

[5] W. Kullmann, J. Geurts, W. Richter, N. Lehner, H. Rauh, U. Steigenberger, G. Eichhorn, R. Geick, *Phys. Status Solidi. B* **125**,131, (1984); W. Kullmann, G. Eichhorn, H. Rauh, R. Geick, G. Eckold, and U. Steigenberger, Phys. stat. sol. (b) **162**, 125 (1990).

[6] V. Russo, A. Bailini, M. Zamboni, M. Passoni, C. Conti, C. S. Casari, A. Li Bassi and C. E. Bottani1. J. Raman Spectrosc. **39**, 205-210 (1984).

[7] L. M. Goncalves , C. Couto, P. Alpuim , A. G. Rolo , F. Völklein , J. H. Correia , Thin Solid Films **518**,10, 2816 (2009).

[8] P. Y. Yu and M. Cardona, *Fundamentals of Semiconductors*, 3rd ed. ISBN 3-540-25470-6, (2005).

[9] V. Wagner, G. Dolling, B. M. Powell and G. landwehr, *Phys stat. sol. (b)* **85**, 311 (1978).

[10] W. Cheng and S. F. Ren, *Phys. Rev. B* **83**, 094301 (2011).

[11] Y. Zhang, K. He, C. Z. Chang, C. L. Song, L. L. Wang, X. Chen, J. F. Jia, Z. Fang, X. Dai, W. Y. Shan, S. Q. Shen, Q. Niu, X. L.Qi, S. C. Zhang, X. C. Ma and Q. K. Xue, *Nature Physics* 6, 584 (2010).

[12] G. C. Sosso, S. Caravati1, and M. Bernasconi, *J. Phys.: Condens. Matter* **21**, 095410 (2009).

[13] S. K. Mishra, S. Satpathy and O. Jepsen, *J. Phys.: Condens. Matter* **9**, 461 (1997).

[14] K. Alim, V.A. Fonoberov and A.A. Balandin, *Appl. Phys. Lett.* **86**, 053103 (2005).

[15] K. A. Alim, V. A. Fonoberov, M. Shamsa, and A. A. Balandin, *J. Appl. Phys.* **97**, 124313 (2005).

[16] A. K. Sood, J. Menendez, M. Cardona and K. Ploog, *Phys. Rev. Lett.* **54**, 2111 (1985).

[17] A. A. Kiselev, K. W. Kim, M. A. Stroscio, *Phys. Rev. B* **59**, 10212 (1999).

[18] V. P. Elestin, Y. V. Kopaev, *Solid State Commun.* **96**, 897 (1995).

[19] I. Calizo, S. Ghosha, W. Baob, F. Miaob, C. N. Lau and A. A. Balandin, *Solid State Commun.* **149**, 1132 (2009).

[20] I. Calizo, W. Bao, F. Miao, C.N. Lau and A.A. Balandin, *Appl. Phys. Lett.* **91**, 201904 (2007).

Chapter 6

Thermal Properties of Graphene: Future Paradigm for Thermal Interface Materials

6.1 Introduction

Graphene reveals unique thermal properties near room temperature. The excellent heat-conduction properties of graphene are beneficial for all proposed electronic and photonic applications. This chapter* describes the detailed literature support on experimental and theoretical investigation on thermal conductivity of graphene. It also presents a brief review on thermal interface materials (TIMs).

---

* Part of this chapter has been excerpted by permission from Macmillan Publishers Ltd: A.A. Balandin, "Thermal properties of graphene and nanostructured carbon materials," *Nature Materials* **10**, 569 - 581 (2011). © Nature Publishing Group, 2011

6.2 Basic Heat Conduction

We will start with the basic formalism of heat conduction. According to Fourier's law Thermal conductivity can be expressed as

$$q = K\nabla \mathrm{T} \,. \qquad (6.1)$$

Here K, thermal conductivity is treated as constant for small temperature (T) variations but in case of wide temperature range, K is a function of T. and ∇T is the temperature gradient. In solid materials heat is carried by acoustic phonons and electrons so that $K = K_e + K_p$, where K_p and K_e are the phonon and electron contributions, respectively. In metals, electron contributed thermal conductivity is dominant assuming large concentrations of free carriers (eg. In pure copper, K_p is limited to 1–2% of the total K ≈ 400 W mK^{-1} at RT). Measurements of the electrical conductivity (σ) define K_e via the Wiedemann–Franz law,

$$\frac{K_e}{\sigma T} = \frac{\pi^2 k_B^2}{3e^2} \,, \qquad (6.2)$$

Where, k_B the Boltzmann constant and e is the charge of an electron. The effect of temperature on thermal conductivity is different for metals and nonmetals. In metals conductivity is primarily due to free electrons. Following Wiedemann–Franz law (eqn. 6.2) thermal conductivity of metals is approximately proportional to the absolute temperature (in Kelvin) times electrical conductivity. In pure metals the electrical resistivity often increases proportional to temperature and thus thermal conductivity stays approximately constant. In alloys the change in electrical conductivity is usually smaller and thus thermal conductivity increases with temperature, often proportional to temperature. On the other hand conductivity in nonmetals is mainly due to lattice vibrations (phonons). Except for high quality crystals at low temperatures, the phonon mean free path of phonons is not reduced significantly at higher temperatures. Thus the thermal conductivity of nonmetals is approximately not constant at low temperatures. At low temperatures well below Debye-temperature thermal conductivity decreases just like the heat capacity does. Heat conduction in carbon materials is usually dominated by phonons, even for graphite [1], which has metal-like properties [2]. This is explained by the strong covalent sp^2 bonding resulting in efficient heat transfer by lattice vibrations. However, electron contribution, K_e can become significant in doped materials. The phonon thermal conductivity is expressed as

$$K_p = \sum_j \int C_j(\omega)\upsilon_j^2(\omega)\tau_j(\omega)d\omega \ , \tag{6.3}$$

where j is the phonon polarization branch, that is, two transverse acoustic (TA) branches and one longitudinal acoustic (LO) branch; υ is the phonon group velocity, which, in many solids, can be approximated by the sound velocity; τ is the phonon relaxation time, ω is the phonon frequency and C is the heat capacity. The phonon mean-free path (Λ) is related to the relaxation time as $\Lambda = \tau\upsilon$. In the relaxation-time approximation, various scattering mechanisms, which limit Λ, are additive, that is, $\tau^{-1} = \Sigma\tau_i^{-1}$, where i enumerates the scattering processes. In typical solids, the acoustic phonons, which carry the bulk of heat, are scattered by other phonons, lattice defects, impurities, conduction electrons and interfaces.

A simpler equation for K_p, derived from the kinetic theory of gases, is $K_p = \frac{1}{3} C_p \upsilon \Lambda$, where C_p is the specific heat capacity. It is important to distinguish between diffusive and ballistic phonon-transport regimes. The thermal transport is called diffusive if the size of the sample, L, is much larger than Λ, that is, phonons undergo many scattering events. When $L < \Lambda$ the thermal transport is termed ballistic. Fourier's law assumes diffusive transport. Thermal conductivity is called intrinsic when it is limited by the crystal-lattice anharmonicity. Thermal conductivity is extrinsic when it is mostly limited by the extrinsic effects, such phonon-rough-boundary or phonon-defect scattering. In nanostructures, K is reduced by scattering from boundaries, which can be evaluated as $\frac{1}{\tau_B} = \left(\frac{\upsilon}{D}\right)\left(\frac{1-\rho}{1+\rho}\right)$. Here τ_B is the phonon lifetime and $\frac{1}{\tau_B}$ is the phonon scattering rate, D is the nanostructure or grain size and ρ is the specularity parameter defined as a probability of specular scattering at the boundary. In nanostructures with $D << \Lambda$, phonon dispersion can undergo modifications owing to confinement resulting in changes in υ and more complicated size dependence. C_p is defined by the phonon density of states, which leads to different temperature dependence of C_p in 3D, 2D and 1D systems, and reflected in the *K(T)* dependence at low T [3,4]. For example, in bulk at low T, *K(T)* is ~T^3 , whereas it is ~T^2 in 2D systems.

6.3 Thermal Properties of Graphene

Graphene attracts much interest due to its high intrinsic thermal conductivity. In order to get graphene through mechanical exfoliation process one generally uses highly oriented pyrolytic graphite (HOPG) bulk graphite. Pyrolytic graphite, which is similar to highly oriented pyrolytic graphite (HOPG), has an in-plane K of ~2,000 W mK^{-1} at room temperature. The experimental K values for HOPG are in excellent agreement with theoretical predictions for the intrinsic K of graphite [1, 5]. So graphite itself has a high thermal conductivity compare to other leading metals (eg. Cu: K ~ 400 W/mK, Al: K~237 W/mK and Sn: K ~ 68 W/mK) [1-4]. Any smaller value is indicative of lower-quality graphite, where K is limited by phonon scattering on grain boundaries, defects or rough sample edges.

Two leading carbon allotropies are graphene and CNT and here in this discussion we will discuss on the different aspects of thermal properties of graphene. Thermal transport in CNTs and graphene, unlike in NCD or DLC, can be dominated by the intrinsic properties of the strong sp^2 lattice, rather than by phonon scattering on boundaries or by disorder, giving rise to extremely high K values [6-9] . From the theoretical point of view, CNTs are similar to graphene, but have large curvatures and different quantization conditions for phonon modes.

The first experimental studies of the thermal conductivity of graphene were reported by Balandin *et al.* [8]. The optothermal Raman measurements were performed with large-area suspended graphene layers exfoliated from high-quality HOPG. The experiment was performed by developing an optothermal Raman technique. The heating power ΔP was provided by a laser light focused on a suspended graphene layer connected to heat sinks at its ends. Temperature rise (ΔT) in response to ΔP was determined with a micro-Raman spectrometer. The G peak in graphene's Raman spectrum exhibits strong T dependence. The excitation power dependence of the Raman G peak has been calculated for a number of long graphene flakes suspended over the trench and connected to the large graphite heat sinks. Finally the thermal conductivity is calculated using following equation

$$K = \left(\frac{L}{2a_G W} \right) \chi_G \left(\frac{\Delta\omega}{\Delta P_G} \right)^{-1}, \tag{6.4}$$

Where, $\chi_G = \frac{\Delta\omega}{\Delta T}$ is the temperature coefficient, L is the distance from the middle of the suspended SLG to the heat sink. Detail experimental procedure can be found at ref. [8]. The authors found K exceeding ~3,000 W mK^{-1} near room temperature, that is, above the bulk graphite limit.

Now we will discuss on some other reports on thermal conductivity of Graphene which are also in line with the first experimental studies carried out by Balandin *et al.* [8]. A following independent study also used the Raman technique, but modified it by addition of a power meter under the suspended portion of graphene. It was found that the K of suspended high-quality graphene prepared by CVD exceeded ~2,500 W mK^{-1} at 350 K, and it was as high as ~1,400 W mK^{-1} at 500 K (experimental uncertainty ~40%) . The reported value is larger than the K of bulk graphite at room temperature [10]. Another group that repeated the optothermal Raman measurements found $K \approx 630$ W mK^{-1} for suspended graphene at $T \approx 660$ K [25]. The graphene membrane was heated to T = 660 K in the centre and above ~500 K over most of its area. Since K decreases with T, this fact can be explained the lower K value of graphene. Differences in strain distribution in the suspended graphene of various sizes and geometries may also affect the results. Other optothermal studies with suspended graphene found K in the range from ~1,500 to ~5,000 W mK^{-1} [11]. The data for suspended or partially suspended graphene is closer to the intrinsic K because suspension reduces thermal coupling to the substrate and scattering on the substrate defects and impurities. It also helps to form the in-plane heat wave front, which allows one to obtain the data pertinent to graphene itself rather than to the graphene/substrate interface even if only a part of the layer is suspended.

For practical applications, it is important to know the thermal conductivity of supported graphene, that is, graphene attached to the substrate along its entire length. The measurements for exfoliated graphene on SiO_2/Si revealed an in-plane K of ~600 W mK^{-1} near room temperature [12]. This value is below those reported for suspended graphene, but it is still rather high, exceeding the K of Si (145 W/mK^{-1}) and Cu (400 W /mK^{-1}). Solving the Boltzmann transport equation, the authors determined the K of free graphene to be ~3,000 W mK^{-1} near room temperature. They attributed the reduced experimental value to graphene–substrate coupling and phonon leaking across the interface [12]. An independent study, which used an electrical self-heating method, found $K \approx 1{,}000 - 1{,}400$ W mK^{-1} near room temperature for graphene nanoribbons with less than five atomic planes and a width between 16 nm and 52 nm [13].

Table 6.1: Thermal Conductivity of Graphene and Carbon nanotubes.

Sample	**K(W/mK)**	**Method**	**Comments**	**Refs**
SW-CNT	~3500	Electrical self-heating	individual; boundary	7
	1750 - 5800	Thermocouples	bundles; diffusive	17
	3000 - 7000	Thermocouples	individual; ballistic	18
	~2500	Theory: BTE	$K_{CNT} < K_{graphene}$	22
MW-CNT	>3000	Electrical self-heating	individual; diffusive	6
CNT	1500 - 2900	Electrical	Individual	19
	~6600	Theory: MD	$K_{CNT} < K_{graphene}$	20
	~3000	Theory: MD	Strong defect dependence	21
Graphene	~2000 - 5000	Raman optothermal	suspended; exfoliated	8,9
FLG	~1300 - 2800	Raman optothermal	suspended; exf. n=4-2	14
Graphene	~2500	Raman optothermal	suspended; CVD	10
	1500 - 5000	Raman optothermal	suspended; CVD	11
	600	Raman optothermal	Suspended,exf.;T~660 K	25
FLG ribbon	1100	Electrical self-heating	supported;exfoliated; n<5	13
Graphene	600	Electrical	supported; exfoliated	12
	2000 - 5000	Theory:VFF,BTE	strong width dependence	24
	1 - 5000	Theory: RTA, g_{TA}, g_{LA}	strong size dependence	25
	8000 - 10000	Theory: MD, Tersoff	square graphene sheet	26
	1400 - 3400	Theory: BTE	length dependence	22
	~4000	Theory: ballistic	strong width dependence	15

Table 6.1 provides representative experimental data for suspended and supported graphene. The reported thermal conductivity value varies depending on measurement procedure and quality of flakes.

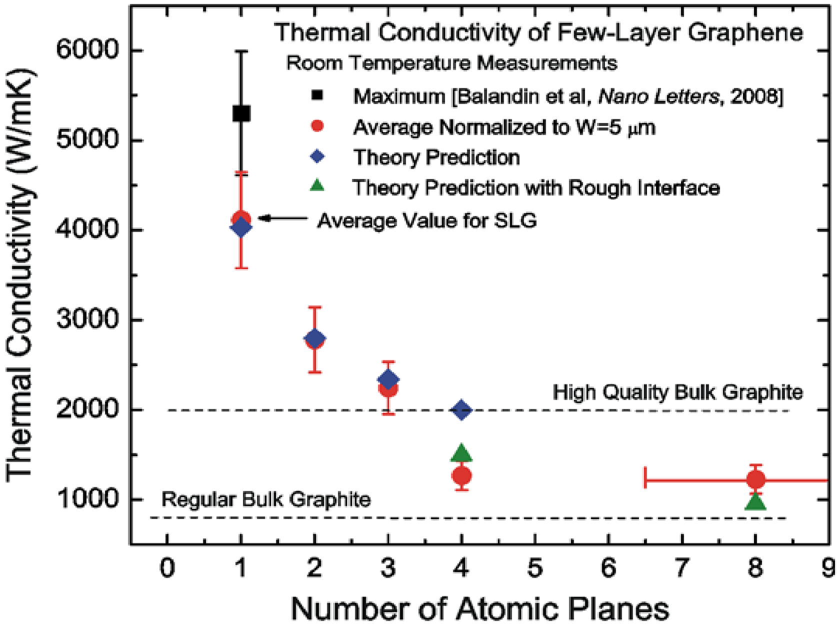

Figure 6.1: Measured and calculated thermal conductivity of suspended FLG as a function of n (at the fixed flake width, W). Adapted from ref. 14, Reprinted by permission from Macmillan Publishers Ltd: A.A. Balandin, "Thermal properties of graphene and nanostructured carbon materials," *Nature Materials* **10**, 569 - 581 (2011). © Nature Publishing Group, 2011.

To examine the evolution of the thermal properties of FLG with increasing thickness, H (number of atomic planes, n) a separate Raman study [14] found that K of suspended uncapped FLG decreases with increasing n, approaching the bulk graphite limit (Fig. 6.1). This evolution of K was explained by considering the intrinsic quasi-2D crystal properties described by the phonon Umklapp scattering [14]. As n in FLG increases, the phonon dispersion changes and more phase-space states become available for phonon scattering leading to a decrease in K. In case of encased graphene, the situation is entirely different because thermal transport is limited by the acoustic phonon scattering from the top and bottom boundaries and disorder, which is unavoidable when FLG is embedded between two layers of dielectrics. Jang *et al*. [15] conducted a study with the 3ω technique and found $K \approx 160$ W mK^{-1} for encased single-layer graphene at $T = 310$ K. It increases to ~1,000 W mK^{-1} for graphite films with $H \approx 8$ nm. Thermal conduction in encased FLG was limited by rough-boundary scattering and disorder penetration throughout the graphene. The presence of the evaporated oxide layers on top of the graphene also cause defects in the graphene layer. Correspondingly, K dependence on H was similar to other material systems where K is extrinsically limited and scales with H. In conventional crystalline thin films, where $H < \Lambda$, but still much larger than the lattice constant, K grows with H as $K \approx C\upsilon H$ until it reaches the bulk limit $K \approx C\upsilon\Lambda$. Similar trend was also reported by Balandin *et al.* [16] for ultrathin Diamond like Carbon films.

All these interesting properties attracted us to propose Graphene as leading materials for thermal management applications. In the next section, I will discuss in brief about thermal interface materials which is considered as one of the major components of thermal management system.

6.4 Thermal Interface Materials

Rapidly increasing power densities in electronics made efficient heat removal a crucial issue for progress in information, communication and energy storage technologies [27-29]. Various interfaces exist between the high power, heat generating component and the heat sink. Micro-scale surface roughness and waviness of the surfaces have an impact on the heat conduction across the interface, as there are gaps filled with low thermal conductivity air. The irregularity of real surfaces is therefore a primary cause of thermal contact resistance. In order to minimize the thermal contact resistance, filler materials are therefore generally required to enhance the contact between the mating surfaces. Thermal interface materials (TIMs), applied between heat sources and heat sinks, are essential ingredients of thermal management [30-34] (see figure 6.2). The function of TIMs is to fill the microscale gaps between two contacting materials to enhance the heat conduction through the interfaces.

Conventional TIMs filled with thermally conductive particles require high volume fractions f of filler (f~50%) to achieve thermal conductivity K of the composite in the range of ~1-5 W/mK at room temperature (RT) [29-32]. Earlier attempts of utilizing highly thermally conductive nanomaterials, e.g. carbon nanotubes (CNTs), as fillers in TIMs, have not led to practical applications due to weak thermal coupling at CNTs/base interface and prohibitive cost. It has been widely recognized that TIMs are one of the main bottlenecks preventing the efficient heat transfer from the integrated chips to the heat sinks and ambient environment. Intensive efforts have therefore been put into the research of novel TIMs in both academia and industry during recent years.

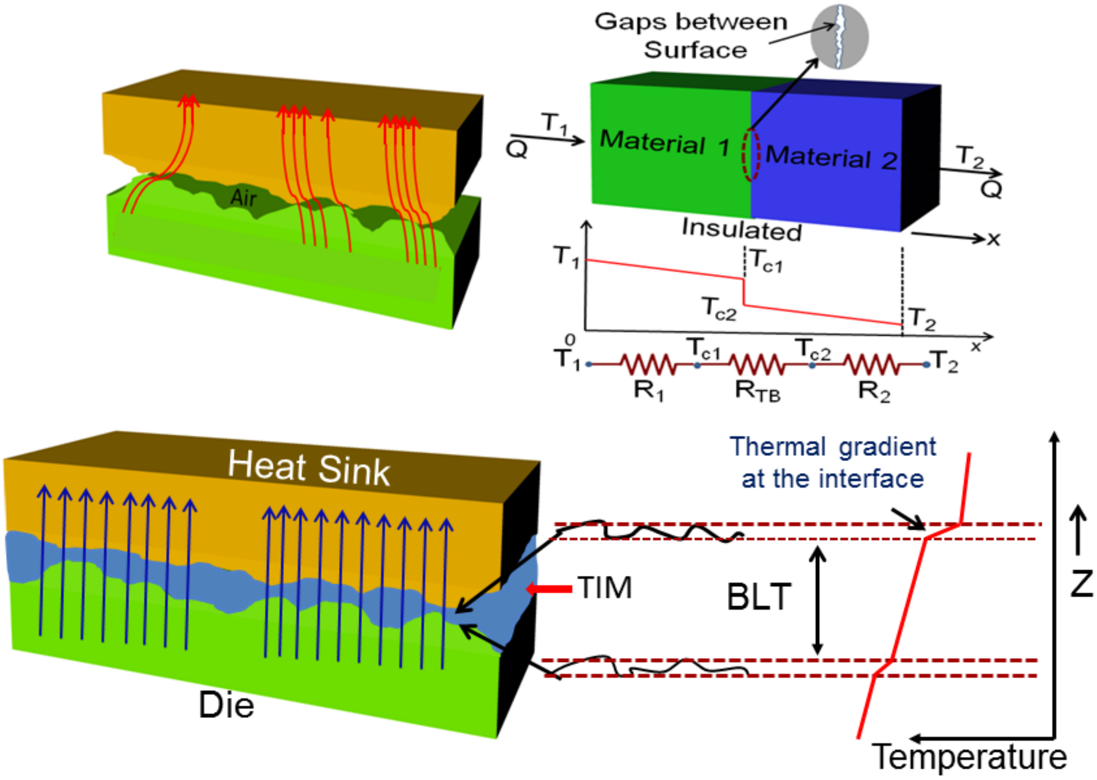

Fig. 6.2: Schematic illustrating the action of thermal interface material, which fills the gaps between two contacting surfaces. The heat removal improves with higher thermal conductivity, smaller bond line thickness and contact resistance of the material.

TIM's performance is characterized by $R_{TIM}=BLT/K+R_{C1}+R_{C2}$, where BLT is the bond line thickness and $R_{C1,2}$ are the TIM's contact resistance with the two bounding surfaces. The magnitude of R_{TIM} depends on the surface roughness, interface pressure P, temperature T, and viscosity ξ. The common TIMs are composites, which consist of polymer matrix or base material and thermally conductive filler particles. TIMs have to be mechanical stabile, reliable, non-toxic, low-cost and easy to apply [28-32]. They should possess as high K as possible, as well as low ξ and coefficient of thermal expansion. The industrial TIMs have R_{TIM} ~3-10×10^{-6} Km^2/W [29]. The drive to reduce L of the conventional fillers, e.g. metal particles, is explained by the fact that smaller L at high f results in larger particle-to-particle contact area and lower R_{TIM} [32]. There has been a great drive in the industry in reducing $\mathrm{R_{TIM}}$. It is not only because of the generated total power (Q) but also due to nonuniform heat flux within the chip. So The thermal problem for chip cooling is not all about maintaining the average temperature of the chip below a certain design point, but it is about maintaining the temperature of the hottest spot below a certain level. The efficiency of the filler in TIMs is characterized by the thermal conductivity enhancement (TCE) defined as $\eta = (K - K_m)/K_m$, where K is thermal conductivity of the composite and K_m is thermal conductivity of the matrix material. TCE of ~170% at the 50% loading of conventional fillers such as silver or alumina with the filler particle size L<10 μm are considered to be standard. Apart from thermal requirements, the specific needs for the electrical insulation of electronic parts have considerable impacts on the product design-in of thermal interface materials. TIMs therefore can be classified into (i) electrically insulating (e.g. Silicone foils, Engineering plastics, Gap fillers based on flexible elastomers, phase change films etc.) or (ii) electrically non-insulating materials (e.g. Thermal grease. Thermally conductive adhesive films made of electrically conductive carriers, Graphite foils consisting 98% pure Graphite etc.). In addition, parameters such as chemical stability, proper surface properties with minimal surface deviations, mechanical tolerances, softness and flexibility, tensile strength, processability, easy handling and last but not least the economic efficiency have to be considered to meet the industry requirement. Also Environmental compatability, reworkability, suitability to adhesive coating, chemical, temperature and ageing resistance, as well as life time and low out-gasing are other important factors.

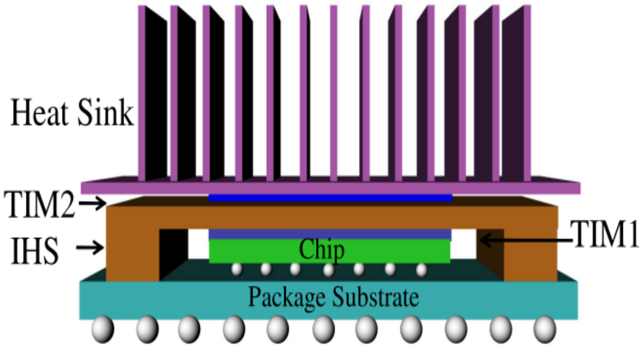

Figure 6.3: A typical packaging architecture for desktop computers where two levels of TIMs are used.

Figure 6.3 shows a typical packaging architecture for desktop computers used for real electronic cooling applications. Two thermal interface material (TIM) layers are used to ensure a continuous path for heat flow. The layer exists at the first level between the backside of the silicon device and an Integrated Heat Spreader (IHS) lid is termed as "TIM1" and the other TIM layer i.e., "TIM2" exists between the IHS and the heat sink, as shown in Figure 6.3. The adhesion of the TIM1 and IHS lid sealant must be high enough to permit rework of the heat sink assembly while the lid remains attached to the heat sink through the TIM2.

A decade ago, CNTs attracted attention as potential fillers for TIMs. Their main attractive feature is extremely high intrinsic thermal conductivity K_i of CNTs in the range of ~3000–3500 W/mK at RT [33-34]. The outcomes of experiments with CNT-based TIMs were controversial. The measured TCE factors were moderate, in the range ~50-250% at f~7% of the CNT loading [35-37]. In some cases, K was not improved substantially [37] or even decreased with addition of single-wall CNTs [38]. The common reason offered as an explanation was that although CNTs have excellent K_i they do not couple well to the matrix material or contact surface. The reported thermal boundary resistance (TBR) between CNTs and polymer matrix was as high as $\sim 10^{-7}$ m^2KW^{-1} [39]. The large TBR at CNT/matrix interface can be attributed to the fundamental property – high Kapitza resistance [40] between one-dimensional (1D) CNTs and 3D bulk owing to the large difference in the phonon density of states (DOS). It was also suggested that the lack of thermal percolation in CNT composites can negatively affect their heat conduction properties [41]. Interestingly, the electrical percolation thresholds f_T for CNT composites are very low, f~0.1 vol. %, compared to 20–30 vol. % for composites with spherical fillers [32, 41]. TIMs with aligned CNTs have better K but suffer from large R_C and prohibitive cost. These outcomes provide strong motivation for the search of alternative high-K fillers.

6.5 Summary

The chapter discusses the excellent heat-conduction properties of graphene, which are beneficial for all proposed electronic and photonic applications. The transparent FLG electrodes can perform the additional function of removing heat and improving the efficiency of photovoltaic solar cells through the reduction of its temperature under illumination. Similarly, FLG serving as interconnects in 3D electronics can simultaneously act as lateral heat spreaders. Here in this dissertation we aim to demonstrated K enhancement of TIMs composites by addition of small volume fractions of grapheme which is promising for future thermal management applications.

References

[1] P. G. Klemens. *J. Wide Bandgap Mater.* **7**, 332–339 (2000).

[2] H. O. Pierson, *Handbook of Carbon, Graphite, Diamonds and Fullerenes: Processing, Properties and Applications*, Noyes Publications (2010).

[3] P. G. Klemens, *Solid State Physics*, Vol. 7 (ed. Seitz, F. & Turnbull, D.) 1–98, Academic, (1958).

[4] J. M. Ziman, *Electrons and Phonons: The Theory of Transport Phenomena in Solids,* Oxford Univ. Press (2001).

[5] P. G. Klemens and D. F. Pedraza, *Carbon* **32**, 735–741 (1994).

[6] P. Kim, L. Shi, A. Majumdar and P. L. McEuen, *Phys. Rev. Lett.* **87**, 215502 (2001).

[7] E. Pop, D. Mann, Q. Wang, K. Goodson, and H. Dai, *Nano Lett.* **6**, 96–100 (2006).

[8] A. A. Balandin S. Ghosh,W. Bao, I. Calizo, D. Teweldebrhan, F. Miao and C. Ning Lau, *Nano Lett.* **8**, 902–907 (2008).

[9] S. Ghosh, I. Calizo, D. Teweldebrhan, E. P. Pokatilov, D. L. Nika, A. A. Balandin,W. Bao, F. Miao and C. N. Lau, *Appl. Phys. Lett.* **92**, 151911 (2008).

[10] C. Faugeras, B. Faugeras, M. Orlita, M. Potemski, R. R. Nair and A. K. Geim, *ACS Nano* **4**, 1889, (2010).

[11] L. A. Jauregui, Y. Yue, A. N. Sidorov, J. Hu, *ECS Trans.* **28**, 73–83 (2010).

[12] J. H Seol, I. Jo, A. L. Moore, L. Lindsay, Z. H. Aitken, M. T. Pettes, X. Li, Z. Yao, R. Huang, D. Broido, N. Mingo, R. S. Ruoff and L. Shi, *Science* **328**, 5975, 213–216 (2010).

[13] R. Murali, Y. Yang, K. Brenner, T. Beck and J. D. Meindl, *Appl. Phys. Lett.* **94**, 243114 (2009).

[14] S. Ghosh, W. Bao, D. L. Nika, S. Subrina, E. P. Pokatilov, C. N. Lau and A. A. Balandin, *Nature Materials* **9**, 555–558 (2010).

[15] W. Jang, Z. Chen, W. Bao, C. N. Lau and C. Dames, *Nano Lett.* **10**, 3909–3913 (2010).

[16] A. A. Balandin, M. Shamsa, W. L. Liu, C. Casiraghi and A. C. Ferrari, *Appl. Phys. Lett.* **93**, 043115 (2008).

[17] J. Hone, M. Whitney, C. Piskoti and A. Zettl, *Phys. Rev. B* **59**, R2514–R2516 (1999).

[18] C. H. Yu, L. Shi, Z. Yao, D. Y. Li and A. Majumdar, *Nano Lett.* **5**, 1842–1846 (2005).

[19] M. Fujii, X. Zhang, H. Xie, H. Ago,K. Takahashi,T. Ikuta, H. Abe and T. Shimizu, *Phys. Rev. Lett.* **95**, 065502 (2005).

[20] S. Berber, Y. K. Kwon and D. Tomanek, *Phys. Rev. Lett.* **84**, 4613–4616 (2000).

[21] J. Che, T. Cagin and W. A. Goddard, *Nanotechnology* **11**, 65–69 (2000).

[22] L. Lindsay, D. A. Broido and N. Mingo, *Phys. Rev. B* **82**, 161402 (2010).

[23] W. Cai, A. L. Moore, Y. Zhu, X. Li, S. Chen, L. Shi and R. S. Ruoff, *Nano Lett.***10**, 5, 1645–1651 (2010).

[24] D. L. Nika, E. P. Pokatilov, A. S. Askerov and A. A. Balandin, *Phys. Rev. B* **79**, 155413 (2009).

[25] D. L. Nika, S. Ghosh, E. P. Pokatilov and A. A. Balandin, *Appl. Phys. Lett.* **94**, 203103 (2009).

[26] W. R. Zhong, M. P. Zhang, B. Q. Ai and D. Q. Zheng, *Appl. Phys. Lett.* **98**, 113107 (2011).

[27] A. A. Balandin, *IEEE Spectrum* **29**, 35-39 (2009).

[28] S.V. Garimella, A. S. Fleischer, J. Y. Murthy, A. Keshavarzi, R. Prasher, C. Patel, S. H. Bhavnani, R. Venkatasubramanian, R. Mahajan, Y. Joshi, B. Sammakia, B. A. Myers, L. Chorosinski, M. Baelmans, P. Sathyamurthy and P. E. Raad, *IEEE Transactions on Components and Packaging Technologies* **31**, 801 – 815 (2008).

[29] R. Prasher, *Proceedings of IEEE*, **94**, 1571 – 1585 (2006).

[30] F. Sarvar, D. C. Whalley and P. P. Conway, *Proceeds. Electronics System Integration Technology Conference* (IEEE 1-4244-0553), **2**, 1292-1302 (2006).

[31] R. S. Prasher, J.-Y. Chang, I. Sauciuc, S. Narasimhan, D. Chau, G. Chrysler, A. Myers, S. Prstic and C. Hu, *Intel Technology Journal*, **9**, 285 – 296 (2005).

[32] J. Felba, *Thermally conductive nanocomposites, in Nano-Bio-Electronic, Photonic and MEMS Packaging* (Springer Science, 2010; DOI 10.1007/978), Editors C.P. Wong, K.-S. Moon and Y. Li, 277 – 314 (2010).

[33] P. Kim, L. Shi, A. Majumdar, and P. L. McEuen, *Phys. Rev. Lett.* **87**, 215502-4 (2001).

[34] E. Pop, D. Mann, Q. Wang, K. Goodson and H. Dai, *Nano Lett.* **6**, 1, 96-100 (2006).

[35] A. Yu, M. E. Itkis, E. Bekyarova and R. C. Haddon, *Appl. Phys. Lett.* **89**, 133102 (2006).

[36] P. Bonnet, D. Sireude, B. Garnier and O. Chauvet, *Appl. Phys. Lett.* **91**, 201910 (2007).

[37] M. T. Hung, O. Choi, Y. S. Ju and H. T. Hahn, *Appl. Phys. Lett.* **89**, 023117(2006).

[38] A. Moisala, Q. Lia, I. A. Kinlocha and A. H. Windle, *Compos. Sci. Technol.* **66**, 10, 1285-1288 (2006).

[39] S. Huxtable, D. G. Cahill, S. Shenogin, L. Xue, R. Ozisik, P. Barone, M. Usrey, M. S. Strano, G. Siddons, M. Shim and P. Keblinski, *Nat. Mater*. **2**, 731 - 734 (2003).

[40] P. L. Kapitza, *J. Phys. USSR* **4**,181(1941).

[41] N. Shenogina, S. Shenogin, L. Xue and P. Keblinski, *Appl. Phys. Lett.* **87**, 133106 (2005).

Chapter 7

Experimental Methodology: Liquid Phase Exfoliation Method and LASER Flash Measurement

7.1 Introduction

In this chapter*, I will discuss the experimental procedure of Thermal Interface Materials (TIMs) sample preparation. We adopted the liquid phase exfoliation (LPE) graphene dispersion method [1-3] and graphene composite preparation techniques [4, 5], with several modifications for maximizing Thermal conductivity enhancement (TCE). The thermal conductivity was measured using LASER flash method [6].

---

* Part of this chapter has been excerpted with permission from K M F Shahil and A. A. Balandin, "Graphene – Multilayer Graphene Nanocomposites as the Highly Efficient Thermal Interface Materials", *Nano Letters*, DOI: 10.1021/nl203906r © 2012, American Chemical Society.

7.2 Liquid Phase Exfoliation Method

The earliest graphene samples were produced using micromechanical cleavage [7, 8]; recent efforts have been focused on developing large scale methods of producing graphene [1-3, 9-12]. Basically two approaches have been considered: one approach is “direct growth” of graphene on substrate which requires transfer of graphene from the growth substrate. Another approach is to use pristine graphite flakes for exfoliation of graphene into various solvent. Our Graphene dispersion process requires ultrasonication of graphite flakes in aqueous solution of sodium cholate followed by sonication and centrifugation. In an extensive trial-and-error procedure, we determined the optimum sonication time (t_s) and centrifugation rate (r_c) resulting in the largest enhancement.

The sample preparations involve the following steps (see Figures 7.1-7.6). First, 10 gm of natural graphite flakes were added to 100 mL of 2% w/v sodium cholate (SC) aqueous solution. In order to maximize the graphene – MLG dispersion we use the high initial graphite concentration. The dispersion was prepared under the ice-cooling with the high-power ultrasonication (see figure 7.2). The ultrasonicated was performed using a Fisher Scientific Model 750 Sonic Dismembrator at a power level of 51-52 W. The ultrasonication was performed for ~12 hr in order to prepare acceptable dispersion of graphitic material. The longer sonication times result in smaller flakes which can be dispersed at higher concentrations. Continuous refilling of the bath water was required to maintain the sonication efficiency and prevent overheating. The process gives not only graphene and thin MLG sheets but also some fraction of thick graphene-graphite slurry.

The solution was left to settle for ~1 hr to allow thick graphite flakes to sediment out of the solution. The top portion of the solution has relatively homogeneous mixture, which is carefully decanted.

Figure 7.1: Determining the weight of the utilized materials – natural graphite and sodium cholate.

The next step is to remove relatively thick layer of graphite material from the dispersion. The solution was centrifuged in filled 2 mL eppendrof tubes at 15 K-rpm for 5 minutes using Fisher Scientific Eppendorf 5424 Microcentrifuges (see figure 7.2). After centrifugation the top 1 mL was carefully separated from each tube and combined. The dispersions (see Figure 7.3) were stable for several weeks and retained for future use. The centrifuged graphene solutions were dried in a vacuum oven at 100°C leaving a suspension of predominately MLG.

Figure 7.2: Photograph of ultrasonication (Fisher Scientific Model 750 Sonic Dismembrator) and centrifuge (Fisher Scientific Eppendorf 5424 Microcentrifuges) equipment at Nano device laboratory, UCR.

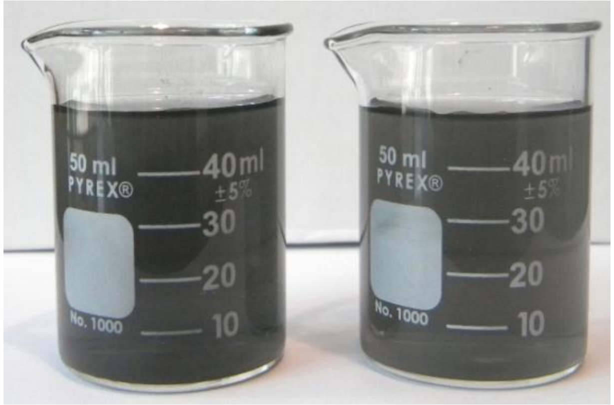

Figure 7.3: Graphene solution after the first ultrasonication and centrifugation. The dispersions were stable for several.

The MLG suspension was dispersed in water followed by ~2 hr ultrasonication. This step was carried out to stabilize the thinnest MLG flakes (*n* is less than 10 layers), which were essential for the enhancement of thermal properties. In order to gain full advantage from dispersions of pristine graphene using surfactants, it will be critical to increase the maximum concentration obtainable while maintaining the quality of the graphene flakes. The goal of this work is to prepare surfactant-stabilized dispersions of graphene at high concentration. In addition, the flakes should be well exfoliated (i.e., few layers per flake) and relatively defect free. Since our chosen method for preparing this type of nanomaterial dispersion requires the use of sonication followed by centrifugation. Thus, we expect that optimization of dispersion parameters will result in enhanced final concentration and dispersion quality.

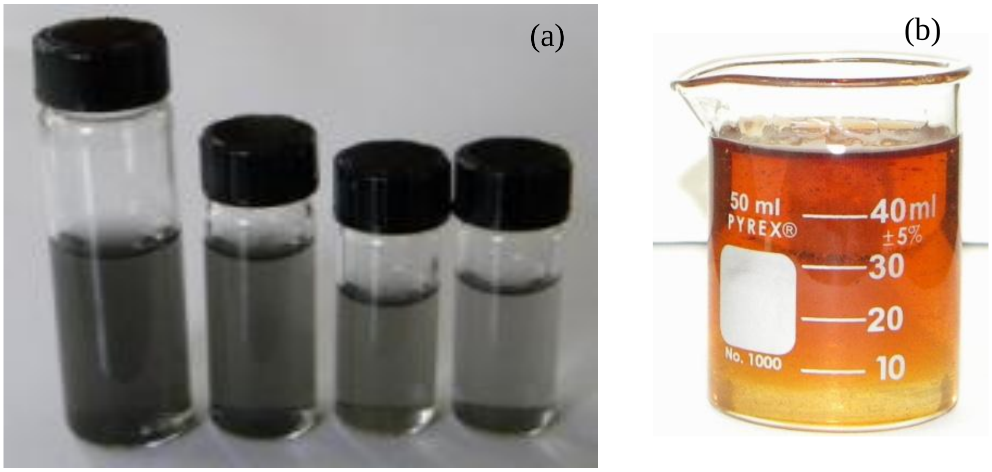

Figure 7.4: (a) LPE graphene dispersion at different concentration. The maximum concentration can be obtained by choosing optimum sonication time and centrifugation time (b) Epoxy resin mixed with curing agent under continuous stirring. Reprinted with permission from K M F Shahil and A. A. Balandin, “Graphene – Multilayer Graphene Nanocomposites as Highly Efficient Thermal Interface Materials”, *Nano Letters,* DOI: 10.1021/nl203906r © 2012, American Chemical Society.

We found that by choosing an optimum optimum sonication time (t_s) and centrifugation rate (r_c) high concentration of graphene can be effectively dispersed in water at a concentration upto 0.25mg/mL (see figure 7.4). This final dispersion was used to prepare TIM samples. Next the solvent was dried in a vacuum oven leaving the hybrid consisting of graphene and MLG with *n*=2-10. The epoxy resin (diglycidyl ether of bisphenol F, EPON 862, source: Hexion) was added to the graphene – MLG suspensnon. The homogeneous mixture was prepared by the high-sheer mixing. The curing agent (diethyltoluenediamine, EPI-CURE W) was added under continuous stirring in a ratio of epoxy to curing agent of 100:26 by weight (Figure 7.4).

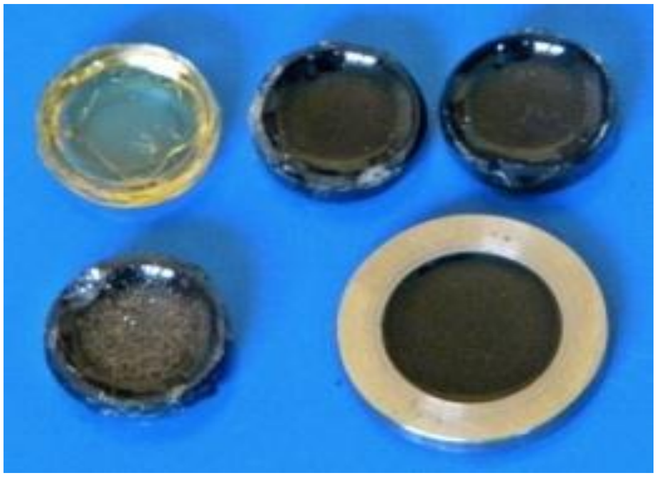

Figure 7.5: Prepared graphene-MLG-hybrid epoxy TIMs. Top left one is prepared with epoxy, and the rests are prepared with prepared with different graphene – MLG loadings at different volume fractions. Reprinted with permission from K M F Shahil and A. A. Balandin, “Graphene – Multilayer Graphene Nanocomposites as Highly Efficient Thermal Interface Materials”, *Nano Letters*, DOI: 10.1021/nl203906r © 2012, American Chemical Society.

Homogeneous mixture of the epoxy and graphene-MLG was loaded into a custom stainless steel mold, heated and degassed in vacuum for curing. The composites were cured at 100 °C for 2 h and at 150 °C for additional 2 h to complete the curing cycle. The curing temperature was determined through the trial and error methods and performed in vacuum oven. Finally the samples were then left for the cool-down and polished. Several samples (Figure 7.5) were prepared with different graphene – MLG loadings varying between 1-10% of the volume fraction.

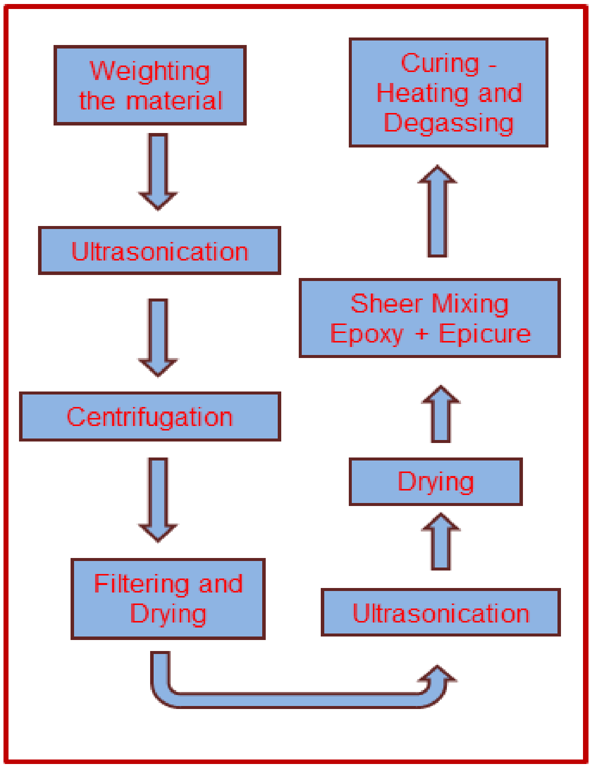

Figure 7.6: Flowchart showing different steps of LPE method.

The detail procedure is shown in the flowchart in figure 7.6. This LPE method described in this section requires no chemical and thermal treatment and inexpensive. We can process graphene in bulk volume without lowering its exotic intrinsic thermal properties.

This method is inexpensive, easy to implement and could be used to scale-up the graphene production important for future industrial applications.

7.3 Laser Flash Method: Experimental Setup

The Nanoflash instrumentation can be used to measure the thermal diffusivity, specific heat and thermal conductivity of metals, graphite, coatings, composites, ceramics, polymers and other materials.

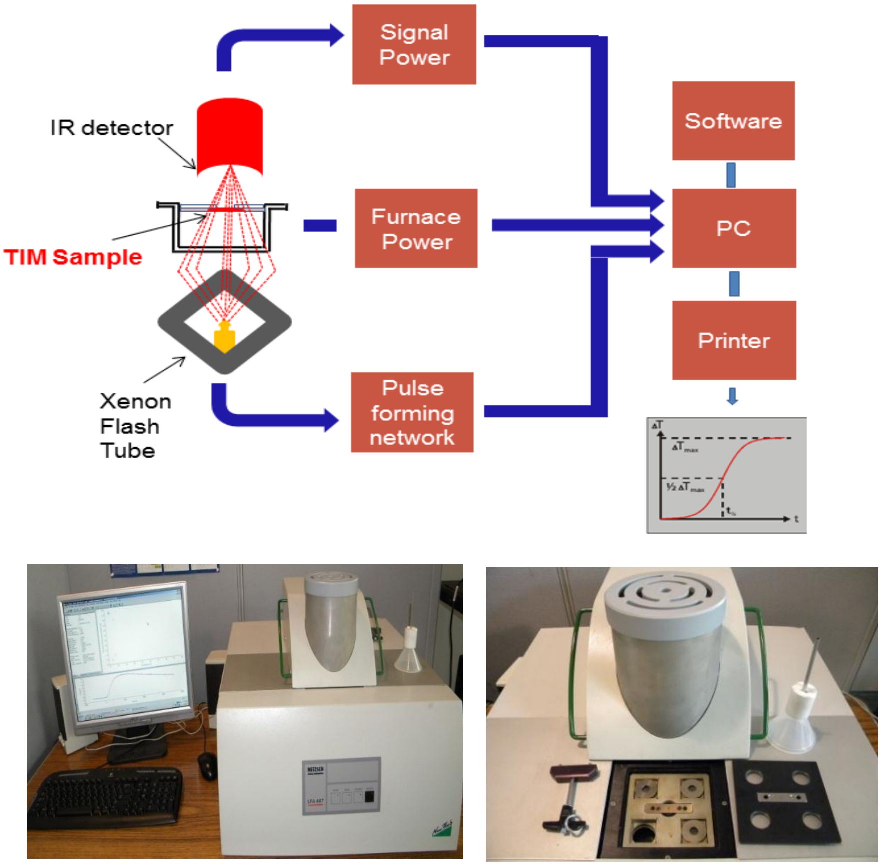

Figure 7.7: (top) Schematic diagram illustrating LASER Flash techniques, (bottom) Photograph of Laser flash equipment used for the measurements (left) and sample holder (right) at Nano device laboratory, UCR.

The instrumentation includes sophisticated hardware and simple menu-driven software to provide fast, accurate, and safe measurements.

The measurements of thermal conductivity, K, were performed by the transient “laser flash” technique (LFT, NETZSCH LFA) (see Figure 7.7). The LFT technique uses a xenon flash lamp, which heats the sample from one end by producing shots with energy of 10 J/pulse. The integrated automatic sample changer allowed unattended analysis of up to 4 samples. The temperature rise was determined at the back end with the nitrogen-cooled InSb IR detector [6]. The output of the temperature detector was amplified and adjusted for the initial ambient conditions. The recorded temperature rise curve is the change in the sample temperature resulting from the firing of the flash lamp. The magnitude of the temperature rise and the amount of the light energy are not required for a diffusivity determination; only the shape of the curve is used in the analysis. From the analysis of the resulting temperature versus – time curve the thermal diffusivity can be determined. For the specific heat measurement, the magnitude of the temperature rise of an unknown sample was compared to that of the reference calibration sample. The measurement of the thermal diffusivity α and specific heat C_p allows the calculation of the thermal conductivity $_K$, with an additional measurement or knowledge of the bulk density ρ of the sample material as shown in equation

$$K = \rho\alpha C_{p}, \tag{7.1}$$

where α is the thermal diffusivity of the film determined in the experiment, C_p is the heat capacity, and ρ is the mass density of the material.

A mathematical analysis of the measured temperature/time function allows the determination of the thermal diffusivity α. This is carried out in the analysis software which includes different mathematical models for the respective application. The simplest model which is described here for understanding is the “adiabatic model” proposed by Parker et al. [13] in 1961. For adiabatic conditions, α is determined by the equation as follows

$$t_{50} = \frac{0.1388 d^2}{\alpha}, \tag{7.2}$$

Where α = temperature diffusivity in cm^2/s, d = thickness of the test piece in cm t_{50}= time at 50% of the temperature increase, the time when the dimensionless temperature, $\theta = T/T_{peak}$ which is equal to 0.5. In 1962, Cowan [14] included the possibility of heat loss from the front and the back face of the sample. In addition, it also assume that the energy pulse was rectangular in shape and relatively short duration (pulse time $t_p >> t_{50}$). Later in 1975, Clark and Taylor [15] made the same assumption as Cowan, but instead of analyzing the cooling part of the temperature rise curve, proposed a method for determining thermal diffusivity based on analysis of the heating part of the curve. A detailed description of all available analyzing models is described in the help-system of the analyzing software.

7.4 Summary

The method adopted in this work (i.e. LPE method) is inexpensive and requires little chemical and thermal modification. Due to minimal modification the intrinsic thermal conductivity of graphene is almost retained which helps for further improvement of thermal conductivity of base material. It is worthwhile to mention that LPE method can be used for further scale up important for further industrial applications. The LASER flash method is suitable for accurate, direct and fast measurement of cross plane thermal conductivity and relative temperature dependence.

References

[1] Y. Hernandez, V. Nicolosi, M. Lotya, F. M. Blighe, Z. Sun, S. De, I. T. McGovern, B. Holland, M. Byrne, Y. K. GunKo, J. J. Boland, P. Niraj, G. Duesberg, S. Krishnamurthy, R. Goodhue, J. Hutchison, V. Scardaci, A. C. Ferrari, and J. N. Coleman, *Nature Nanotechnology* **3**, 563 - 568 (2008).

[2] A. A. Green and M. C. Hersam, *Nano Lett.* **9**, 12, 4031–4036 (2009).

[3] M. Lotya, Y. Hernandez, P. J. King, R. J. Smith, V. Nicolosi, L. S. Karlsson, F. M. Blighe, S. De, Z. Wang, I. T. McGovern, G. S. Duesberg and J. N. Coleman, *J. Am. Chem. Soc.* **131,** 10, 3611–3620 (2009).

[4] S. Stankovich, D. A. Dikin, G H. B. Dommett, K. M. Kohlhaas, E J. Zimney, E A. Stach, R. D. Piner, S. T. Nguyen and R. S. Ruoff, *Nature* **442**, 282-286 (2006).

[5] D. Li, M. B. Müller, S. Gilje, R. B. Kaner and G. G. Wallace, *Nature Nanotech*. **3**, 101 - 105 (2008).

[6] R. Fernandez, D. Teweldebrhan, C. Zhang, A.A. Balandin and S. Khizroev, *J. Appl. Phys.* **109**, 07B763 (2011).

[7] K. S. Novoselov, A. K. Geim, S. V. Morozov, D. Jiang, Y. Zhang, S. V. Dubonos, I. V. Grigorieva and A. A.Firsov, *Science* **306**, 666 (2004).

[8] A. K. Geim and K. S. Novoselov, *Nature Materials* **6**, 183-191. (2007).

[9] P. Blake, P. D. Brimicombe, R. R. Nair, T. J. Booth, D. Jiang, F. Schedin, L. A. Ponomarenko, S. V. Morozov, H. F. Gleeson, E. W. Hill, A. K. Geim, K. S. Novoselov, *Nano Lett.* **8**, 6, 1704–1708 (2008).

[10] M. Lotya, P. J. King, U. Khan, S. De, and J. N Coleman, *ACS Nano,* **4**, 6, 3155–3162 (2010).

[11] K. S. Kim, Y. Zhao, H. Jang, S. Y. Lee, J. M. Kim, K. S. Kim, J. H. Ahn, P. Kim, J. Y. Choi, B. H. Hong, *Nature* **457** (7230), 706–710 (2009).

[12] X. L. Li, G. Y. Zhang, X. D. Bai, X. M. Sun, X. R. Wang, E. Wang, H. J. Dai, *Nat. Nanotech.* **3**, 9, 538–542 (2008).

[13] W. J. Parker, R. J. Jenkins, C. P. Butler, and G. L. Abbott, *Journal of Applied Physics* **32**, 1679 (1961).

[14] R. D. Cowan, *Journal of Applied Physics* **34**, 4, 926 - 927 (1963).

[15] L.M. Clark and R. E. Taylor, *Journal of Applied Physics* **46**, 2, 714-719 (1975).

Chapter 8

Results and Discussions: Graphene Based Thermal Interface Materials

8.1 Introduction

This chapter* presents the experimental results on thermal conductivity enhancement (TCE) of graphene reinforced thermal interface materials (TIMs). The experimental study shows a significant TCE over the base material. Also an industry level testing protocol is presented to investigate the effectiveness of graphene based TIMs samples. Detail formalism and modeling approach of developed physics-based Effective Medium Approximation (EMA) model is presented. Simulated results suggest that graphene can outperform other carbon allotropes and derivatives as the thermal filler material. Finally, three dimensional (3D) thermal simulation studies are carried out with the finite-element method (FEM) with in silicon chip structure.

---

* Part of this chapter has been excerpted with permission from K M F Shahil and A. A. Balandin, “Graphene – Multilayer Graphene Nanocomposites as Highly Efficient Thermal Interface Materials”, *Nano Letters,* DOI: 10.1021/nl203906r © 2012, American Chemical Society.

8.2 Synthesis and Characterization of TIMs Sample

To characterize our synthesized LPE (Liquid phase exfoliated) graphene and TIM samples, we performed optical, scanning electron microscopy (SEM) and atomic force microscopy (AFM) of the. The thickness H (=$h \times n$, where h=0.35 nm is the thickness of graphene monolayerand n is the number of layer) and size L distribution of MLG in the nanocomposites were important for maximizing enhancement. We refer to the synthesized materials as nanocomposites because substantial portion of the filler particles had at least one dimension (thickness) below a few nanometers in size and the presence of these nanoscale components was essential for the materials' functionality. To access the quality of dispersion, some of the few layer graphene (FLG) flakes (referred to as graphene nanocomposite) were deposited from graphene dispersion (see figure 8.1 b) onto Si wafers capped by a 300 nm thick SiO_2 layer and were investigated using scanning electron micro-scope (SEM) operated at 10-15 kV. Representative SEM images of graphene film are shown in Figure 8.1 (c, d). Extremely small dimensions of the resulting graphene lead to wrinkled topology at the nanoscale as shown in Figure 8.1 (c, d). The nanoscale surface roughness of FLG could play an important role in enhancing mechanical inter locking and load transfer with the matrix and consequently, better adhesion [1, 2]. AFM studies were performed using a VEECO instrument with the vertical resolution down to ~0.1 nm.

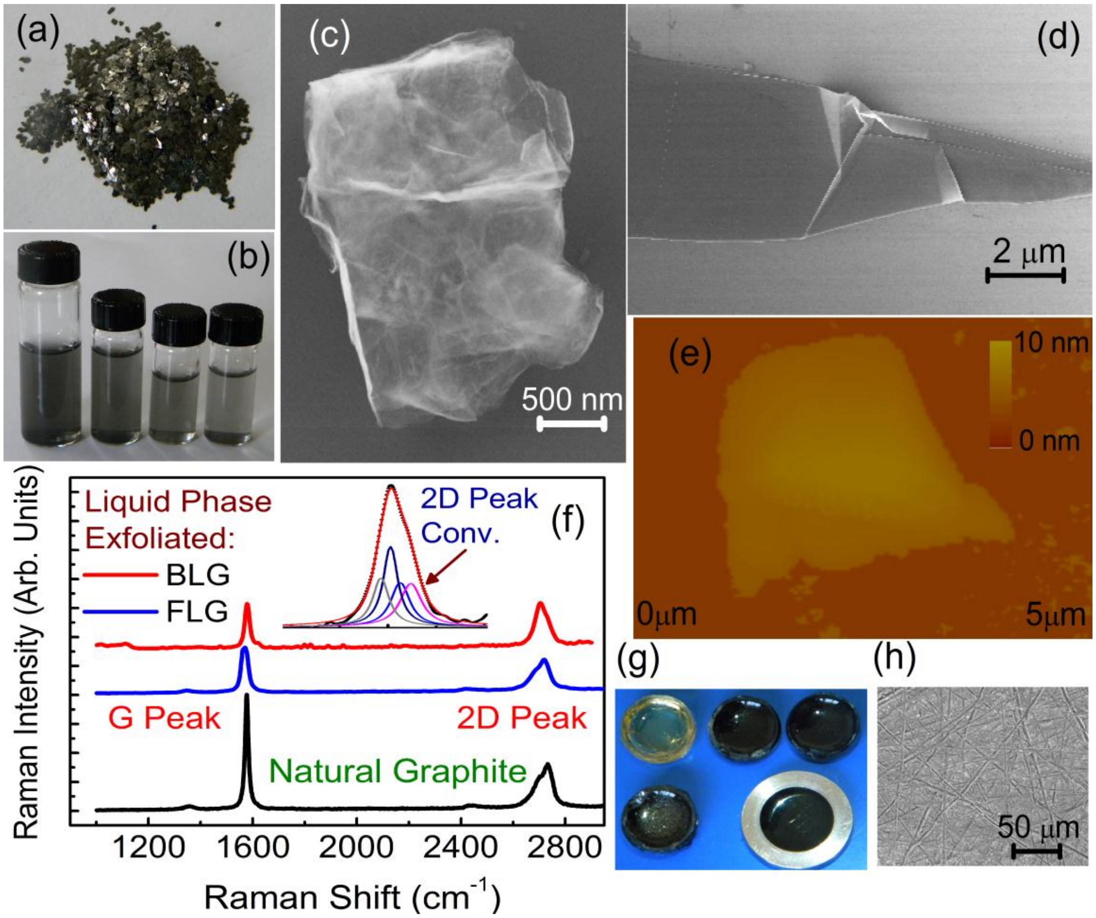

Figure 8.1: Synthesis and characterization of the graphene-MLG polymer nanocomposite TIMs. (a) graphite source material; (b) liquid-phase exfoliated graphene and MLG in solution; (c) SEM image of MLG revealing overlapping regions and wrinkles, which improve thermal coupling. (d) SEM image of a large MLG (n<5) flake extracted from the solution; (e) AFM image of MLG flake with varying n; (f) Raman spectroscopy image of bilayer graphene flakes extracted from the solution; (g) optical image of graphene-MLG polymer composite samples prepared for thermal measurements; (h) representative SEM image of the surface of the resulting graphene based TIMs indicating small roughness and excellent uniformity of the dispersion. Reprinted with permission from K M F Shahil and A. A. Balandin, “Graphene – Multilayer Graphene Nanocomposites as Highly Efficient Thermal Interface Materials”, *Nano Letters,* DOI: 10.1021/nl203906r © 2012, American Chemical Society.

A representative AFM image of chemically derived FLG is shown in as shown in Figure 8.1e. We used micro-Raman spectroscopy to verify number of atomic plane, i.e., *n* [3]. The *n* counting with the Raman spectroscopy is efficient for $n<7$. For thicker flakes the thickness distribution statistics was also derived from AFM inspection. Figure 8.2 (f) shows an example of Raman spectra of MLG from the solution and the reference graphite source excited at $\lambda=488$ nm. The diameter of the laser spot in the micro-Raman spectroscopy was ~1 μm. The spectra are taken in the backscattering configuration under the 488 nm excitation. Three different sets of Raman measurement are shown here. The top two Raman measurements are taken from bilayer (BLG) and few layer regions (i.e. FLG). We have used the spectrum deconvolution procedure to obtain the Lorentzian peaks, which correspond to the four resonant transitions. The splitting of the electron energy levels in BLG leads to appearance of the four phonon peaks, which make up a broad 2D band for BLG. Also the Raman measurement taken from natural graphite (Figure 8.2a) is shown in the same figure for comparison. The most notable features of the spectrum are the G peak at 1578 cm^{-1}, which corresponds to the E_{2g} mode, and a relatively wideband around 2700 cm-1, which refers to as 2D mode [4]. Deconvolution of *2D* band and comparison of the *I(G)/I(2D)* intensity ratio allowed us to determine *n* with a high accuracy, e.g. the plotted spectra correspond to the large-size bilayer graphene ($n=2$) and MLG with $n\approx5$ with The so-called disorder-induced D band is frequently observed in carbon materials at 1350 cm^{-1} The D band has been attributed to in-plane A_{1g} (LA) zone-edge mode, which is silent for the infinite layer dimensions but becomes Raman active for small layers or layers with substantial number of defects through the relaxation of the phonon wave-vector selection rules. The weak intensity of the disorder *D* peak, composed of the A_{1g} zone-edge phonons, indicates the large size and low defect concentration.

The graphene-MLG concentrations utilized for preparation of the nanocomposite TIMs were ~0.253 mg/mL (t_s≈12 hrs, r_c =15 K-rpm). From the statistical analysis we established that the composites with ~10-15% of MLG with $n \leq 2$, ~50% of FLG with $n \leq 5$ are the optimum for maximizing enhancement (see figure 8.2). Based on the optical microscopy and SEM examination, most of the graphene and MLG flakes (~90%) had lateral dimensions in the range L≈50 nm - 0.5 μm. A small fraction of the flakes (~10%), predominantly with $n<5$, had large lateral sizes L≈2-5 μm. As discussed below, their presence in the composites was important.

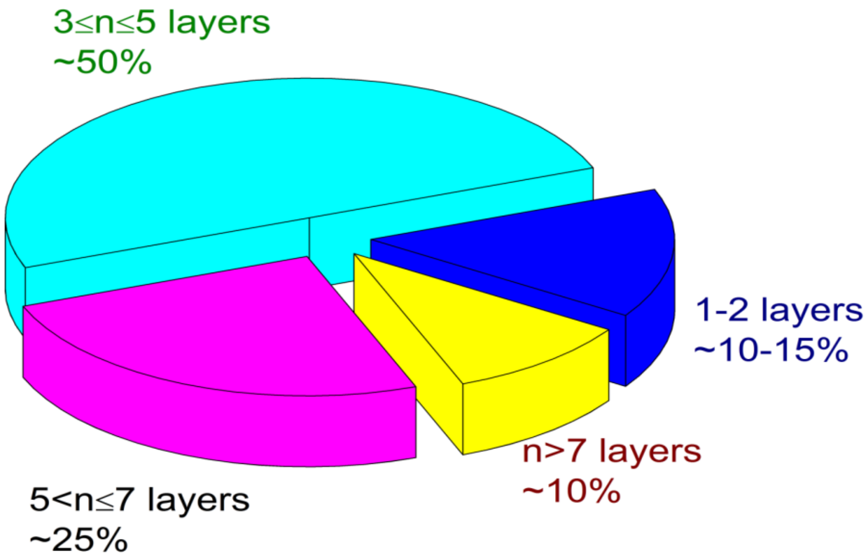

Figure 8.2: Diagram showing statistical analysis of composition of graphene-MLG nanocomposites.

The prepared nanocomposite graphene-MLG solutions were mixed with epoxy followed by curing and heating in vacuum to produce a large number of samples with the carbon loading f ~0.2-10vol.%. The homogeneity and surface variation of the resulting composite and adhesive bonding have been verified with SEM. The prepared graphene-epoxy composite samples were investigated using a high-resolution field-emission scanning electron micro-scope (XL-30 FEG) operated at 10-15 kV. The representative SEM image of the sample surface is presented in Figure 8.1(h) .Uniform dispersion is visible in the SEM image. The image confirms visually the interlayer adhesive bonding of graphene filler with epoxy matrix. The size scale and morphology (wrinkled texture) of the nanostructured graphene lead to strong interfacial interaction with the host polymer. It is important to mention here that our graphene-MLG fillers were substantially different from what is referred to as graphite nanoplatelets (GnP) characterized by higher thickness (10 – 100 nm).

8.3 Thermal Conductivity Enhancement

8.3.1 Experimental Results

We define, the efficiency of the filler in TIMs is characterized by the thermal conductivity enhancement (TCE) defined as $\eta = (K - K_m)/K_m$, where K is thermal conductivity of the composite and K_m is thermal conductivity of the matrix material. Thermal conductivity measurements were conducted with the “laser flash” technique (NETZSCH). Measurements details are given in chapter 7. The sample thicknesses were

1-1.5 mm to ensure that their thermal resistances were much larger than the contact resistance. As a control experiment we measured thermal conductivity of pristine epoxy and obtained K=0.201 W/mK at RT, in agreement with the epoxy vendor's specifications. Figure 8.3 shows TCE factor as a function of f for the graphene-MLG-hybrid epoxy - sample A ($t_s\approx 12$ hrs, $r_c=15$ K-rpm) and sample B ($t_s\approx 10$ hrs, $r_c= 5$ K-rpm) at RT. For comparison, we also measured TCE for the epoxy composites with graphite micro- and nanoparticles obtained by grinding the same graphite (substantial fraction of particles have $L\sim 40$ μm) and for the epoxy composite with commercial carbon black (CB) powder.

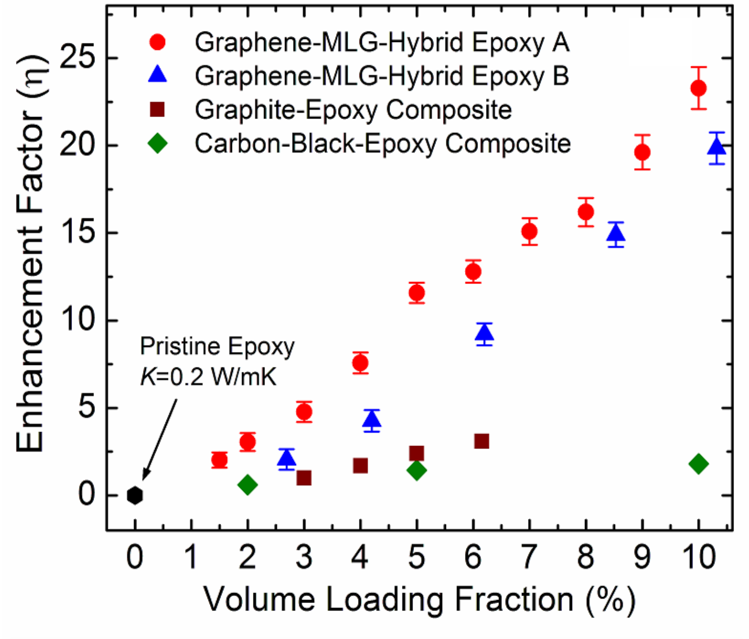

Figure 8.3: Measured thermal conductivity enhancement factor as a fraction of the filler volume loading fraction. Note an extremely large enhancement of ~2300% at f=10 vol. % for the optimum nanocomposite. Reprinted with permission from K M F Shahil and A. A. Balandin, "Graphene– Multilayer Graphene Nanocomposites as Highly Efficient Thermal Interface Materials", *Nano Letters*, DOI: 10.1021/nl203906r © 2012, American Chemical Society.

One can see that there is extraordinary increase in η for our graphene-MLG hybrid composites. At f=10 vol. % loading, K reaches the value of ~5.1 W/mK, which corresponds to TCE of ~2300 %.

Traditional fillers with small aspect ratios show TCE ~20% per 1 vol. % loading. The measured TCE for composites with the amorphous graphite particles were low and consistent with the literature [5-9].There were almost no TCE in CB-epoxy composites for the examined loading fractions. The control experiments with graphite particles and CB confirm that thermal properties of graphene and MLG were essential for increasing K of TIMs. It is interesting to note that TCE follows approximately linear dependence on f without revealing any clear signature of thermal percolation threshold. One would expect to observe a kink in $K(f)$ plot and $K = K_T[(f - f_T)/(1 - f_T)]^{\beta}$ dependence (where □≈2 in 3D) if the percolation is resolved (f step is 1 vol. % in our measurements). The physics of thermal percolation is still a subject of intense debates [5, 10-12].

Unlike electrical percolation the thermal percolation threshold can be less pronounced due to heat conduction by the matrix. Our attempts to increase f of the graphene-MLG-polymer composites beyond 10 vol. % while maintaining acceptable TIM characteristics, e.g. ξ, R_C, were not successful. The changes in ξ lead to inhomogeneous inclusions and surface roughness for f>10 vol. %.

8.3.2 Temperature Dependence

To investigate the temperature dependence of TCE we varied temperature up to ~ 400K. Figure 8.4 shows *K* as a function of *T* for different *f*. The *K* decrease with *T* at higher loading is reminiscent of the Umklapp phonon scattering characteristic for crystalline materials, including graphene [13].

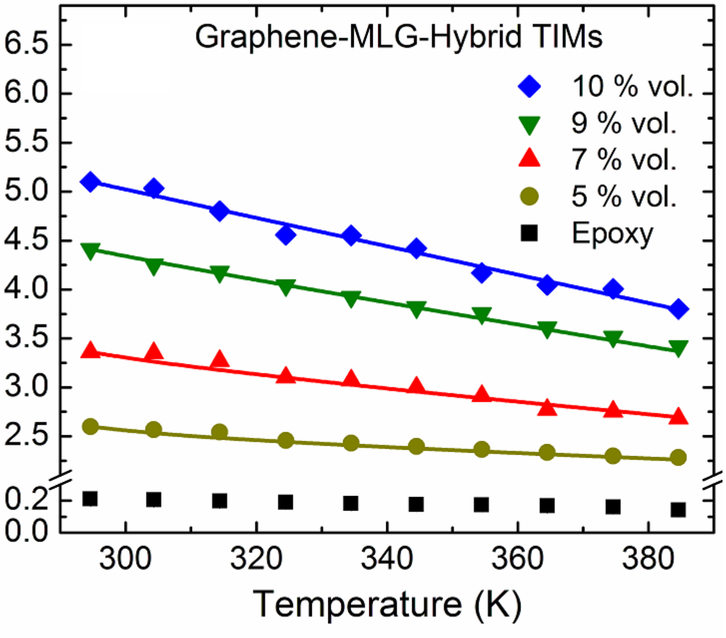

Figure 8.4: Experimentally determined dependence of thermal conductivity of TIMs on temperature for different loading fractions. Reprinted with permission from K M F Shahil and A. A. Balandin, “Graphene – Multilayer Graphene Nanocomposites as Highly Efficient Thermal Interface Materials”, *Nano Letters*, DOI: 10.1021/nl203906r © 2012, American Chemical Society.

This suggests that heat is carried by the thermally linked graphene or MLG flakes when *f*~10%. Contrary, in pristine epoxy the *K(T)* dependence is nearly absent, which is expected for the non-crystalline amorphous solids [13]. To achieve such strong enhancement with the conventional filler materials one would need a higher loading fraction of ~70%. Generally traditional fillers typically show an enhancement of ~20% per 1% vol. loading [9] (see table 8.1).

Table 8.1: Thermal Conductivity Enhancement in TIM Composites

Filler	TCE	Fraction	Base Material	Method	Reference
MWNT	150 %	1.0 vol. %	oil	transient hot wire	[15]
SWNT	125 %	1.0 wt. %	epoxy	comparative method	[18]
p-SWNT	350 %	9.0 wt. %	epoxy	laser flash	[14]
CNT	65 %	3.8 wt. %	silicone	ASTM	[19]
GNP	3000 %	25.0 vol. %	epoxy	laser flash	[20]
GON	30% - 80%	5.0 vol. %	glycol and paraffin	comparative method	[21]
SWNT	55 %	7.0 wt. %	PMMA	guarded plate	[10]
GNP	10 %	1.0 vol. %	epoxy	transient hot wire	[17]
Ni	566 %	<30 %	epoxy	laser flash	[22]
ALN	1900 %	60 %	epoxy	ASTM	[23]
BN	650 %	30 wt. %	epoxy	ASTM	[24]
SWNT	50 %	1 wt. %	polystyrene	steady state method	[25]
Graphite	1800 %	20 wt. %	epoxy	laser flash	[16]
Graphene	2300 %	10 vol. %	epoxy	laser flash	This work [54]

Although a higher filler volume fraction increases the thermal conductivity, it also increases the viscosity of the mix making it more difficult to dispense. The result is an adhesive that is extremely high in viscosity which traps air easily and cannot accommodate thin bond line (see schematic 6.4). Using graphene as filler, a higher thermal conductivity enhancement can be achieved at lower filler loading and this could have much smaller effect on the viscosity. Minimizing the viscosity of TIMs is important in improving the processability, reducing the BLW and overall thermal resistance of the thermal interface layer [9]. The graphene provide very efficient thermal conductivity enhancement compared to other carbon materials as tabulated in Table 8.1. Moreover graphene provide reinforcement in two directions and are expected to be more efficient in improving mechanical properties. It is evident that, for graphene, other factors have effect in thermal conductivity enhancement such as dimensionality, rigidity and low TBR due to its flat structure.

8.4 Theoretical Interpretation and Simulation

8.4.1 Theoretical formalism

Several approaches [26-31] have been proposed to calculate effective thermal conductivity of composite embedded with host material and all these approaches are known as the effective medium approximation (EMA). Rayleigh [26] and Maxwell [27] derived expressions for the thermal conductivity of spherical particle embedded in a host. Later, Hasselman and Johnson [30] incorporated Thermal boundary resistance (TBR) in their model. Nan et al. [28] developed a general equation of the effective thermal conductivity for arbitrary particulate composites based on multiple scattering theories.

To analyze our experimental data, we used the Maxwell-Garnett effective medium approximation (EMA), which works well for f<40% [28-29]. We modified it to include the size of the fillers, aspect ratios α and TBR between the fillers and matrix. First we start with the generalized formalism which gives the thermal conductivity of the composite as

$$K^*_{11} = K^*_{22} = K_m \frac{2 + f\left[\beta_{11}\left(1-L_{11}\right)\left(1+\left\langle \cos^2\phi \right\rangle\right) + \beta_{33}\left(1-L_{33}\right)\left(1-\left\langle \cos^2\phi \right\rangle\right)\right]}{2 - f\left[\beta_{11} L_{11}\left(1+\left\langle \cos^2\phi \right\rangle\right) + \beta_{33} L_{33}\left(1-\left\langle \cos^2\phi \right\rangle\right)\right]} \tag{8.1a}$$

$$K^*_{33} = K_m \frac{1 + f\left[\beta_{11}\left(1-L_{11}\right)\left(1+\left\langle \cos^2\phi \right\rangle\right) + \beta_{33}\left(1-L_{33}\right)\left\langle \cos^2\phi \right\rangle\right]}{1 - f\left[\beta_{11} L_{11}\left(1-\left\langle \cos^2\phi \right\rangle\right) + \beta_{33} L_{33}\left\langle \cos^2\phi \right\rangle\right]} \tag{8.1b}$$

where

$$\beta_{ii} = \frac{K^c_{ii} - K_m}{K_m + L_{ii}\left(K^c_{ii} - K_m\right)} \quad \text{and} \quad \left\langle \cos^2\phi \right\rangle = \frac{\int \rho(\phi)\cos^2\phi \sin\phi \, d\phi}{\int \rho(\phi)\sin\phi \, d\phi} \tag{8.2}$$

Here ϕ is the angle between the material axis X_3 and the local particle symmetric axis X_3'. $\rho(\theta)$ is the distribution function describing particle orientation, f is the volume fraction, $K^c_{ii}(i=1,2,3)$ are the equivalent thermal conductivities along symmetric axis of the composite unit cell, K_m is the thermal conductivity of the matrix phase.

In equation 8.1, L_{ii} are the geometrical factors dependent on the particle shape given by [28]

$$L_{11} = L_{22} = \frac{p^2}{2\left(p^2 - 1\right)} + \frac{p}{2\left(1 - p^2\right)^{\frac{3}{2}}} \cos^{-1} p \quad \text{for} \quad p < 1$$
$$L_{33} = 1 - 2L_{11} \tag{8.3}$$

The equivalent thermal conductivities $K_{ii}^{c}\left(i = 1,2,3\right)$ are as follows

$$K_{ii}^{c} = \frac{K_P}{1 + \frac{\gamma L_{ii} K_p}{K_m}} \tag{8.4}$$

With $\gamma = \left(1 + 2P\right)\alpha$ for $P \leq 1$

Here α is a dimensionless parameter defined as $\alpha = \dfrac{R_{BD} K_m}{a_3}$

With $R_{BD} = \lim\limits_{\delta, K_s \to 0} \left(\dfrac{\delta}{K_s} \right)$

Considering randomly oriented particles, the equations 1(a) and 1(b) are reduced to

$$K^{*}_{eff} = K_m \frac{3 + f\left[2\,\beta_{11}\left(1 - L_{11}\right) + \beta_{33}\left(1 - L_{33}\right)\right]}{3 - f\left[2\,\beta_{11} L_{11} + \beta_{33} L_{33}\right]} \tag{8.5}$$

For the MLG based composite (assuming ideal case) $P \to 0$, $L_{11} \to 0$, $L_{33} \to 1$

$$K_{11}^{c} = Kp \qquad \beta_{11} = \frac{K_p - K_m}{K_m}$$
$$K_{33}^{c} = \frac{K_p}{1 + \frac{a_k K_p}{h.K_m}} \qquad \beta_{33} = \left(1 - \alpha\right) - \frac{K_m}{K_p} \tag{8.6}$$

This leads to

$$K_{eff}^{*} = K_m \frac{3 + 2f\left(\dfrac{K_p - K_m}{K_m}\right)}{3 - f\left\{(1-\alpha) - \dfrac{K_m}{K_p}\right\}} \tag{8.7}$$

Finally Defining $\alpha = \dfrac{R_{BD}K_m}{h}$ and assuming randomly oriented fillers and incorporating TBR, we can write for MLG composites

$$K_{eff}^{*} = \frac{K_p\left[3K_m + 2f\left(K_p - K_m\right)\right]}{\left(3-f\right)K_p + fK_m + \left(\dfrac{fR_{BD}K_mK_p}{h}\right)} \tag{8.8}$$

Here R$_{BD}$ is TBR at the graphene/matrix interface, while Kp and Km are thermal conductivity of the filler and matrix materials, respectively. Graphene has large phonon mean-free path λ~775 nm at RT [13], which is comparable to L. To account for the size effects on heat conduction inside MLG, we altered EMA by introducing

$$K_p = \frac{1}{3}c\upsilon\Lambda_{eff} \tag{8.9}$$

Here C is the volumetric specific heat, υ is the phonon group velocity and Λ_{eff} is the effective phonon mean free path (MFP). Using Matthiessen's rule, we can write the effective MFP as

$$\frac{1}{\Lambda_{eff}} = \frac{1}{\Lambda_b} + \frac{1}{L} \tag{8.10}$$

Here Λ_b is the bulk mean free path; L is the size of the flake. We assume perfectly diffusive scattering case (i.e. perfectly diffusive phonon scattering from the edges, so taking specularity parameter as zero). Our modified MG-EMA formulation takes into account the effects of the aspect ratio (ideally, graphene as an oblate spheroid with aspect ratio, $p \rightarrow 0$, while CNTs as a prolate spheroid with $p \rightarrow \alpha$), thickness, volume fraction, interface scattering in the different phase of the nanocomposites and TBR between the phases. The inclusions (i.e graphene, CNTs) are assumed as randomly oriented within base matrix (i.e epoxy). We derived different formulation for effective conductivities (K^*_{eff}) of the composites reinforced by graphene and CNTs.

8.4.2 Simulated Results: Comparison with CNT

To compare the possible enhancement, we simulated thermal conductivity enhancement ratio (K/K_m) for CNTs based composite material and compare with that of MLG reinforced composite materials as shown in Figure 8.5. The figure shows calculated ratio K/K_m vs. f for MLG (L=100 nm) and CNT composites. The TBR values for CNTs (8.3×10^{-8} m^2 K.W^{-1}) and graphene flakes (~3.7×10^{-9} m^{2}K.W^{-1}) were taken from ref. [32, 33]. An ideal graphene flake can be treated as an oblate spheroid with $\alpha = a_3/a_1 \rightarrow 0$, while CNT can be treated as a prolate spheroid with $\alpha \rightarrow \infty$. This difference in α was theoretically predicted to make graphene much better filler than CNTs [29]. It confirms that MLG can produce higher TCE than CNTs even as one varies α and diameter D of CNTs in a wide range. One should note that the thermal conductivity model of the graphene fillers is based on the kinetic theory and only considers the lateral size effect without accounting for other effects such as the substrate scattering**.**

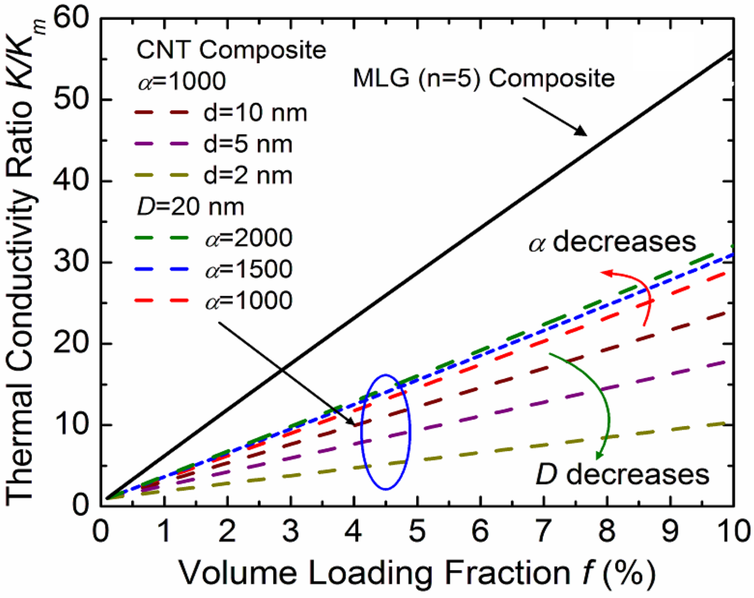

Figure 8.5: Calculated thermal conductivity of graphene-MLG-polymer TIMs. Comparison of thermal conductivity of MGL (n=5) and CNTs based TIMs. Note the dependence of thermal conductivity of CNT composites on the aspect ratio and diameter. Reprinted with permission from K M F Shahil and A. A. Balandin, "Graphene – Multilayer Graphene Nanocomposites as the Highly Efficient Thermal Interface Materials", *Nano Letters*, DOI: 10.1021/nl203906r © 2012, American Chemical Society.

8.4.3 Simulated Results: Thermal Boundary Resistance Extraction

We now use the modified EMA to extract actual thermal boundary resistance (TBR) in our nanocomposite graphene-MLG-epoxy TIMs by fitting calculated K to the experimental data and varying TBR (R_B) value (Figure 8.6). For MLG, we use α=0.01

(≈H/L) and assume Λ=775 nm [3]. The best match with experiment is attained at R_B=3.5×10^{-9} Km^{2}W^{-1}. This value is small and consistent with the molecular dynamics (MD) simulations [33]. Our own calculations indicate that for higher RB, TCE does not increase with f linearly but starts to saturate.

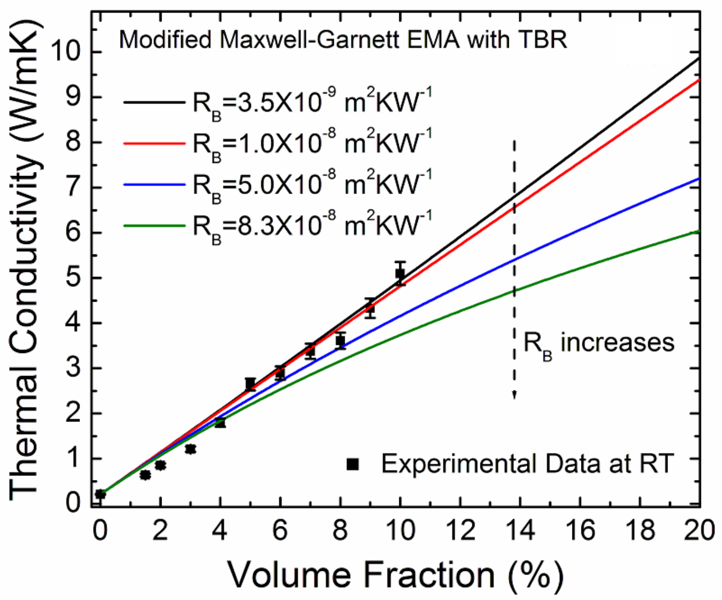

Figure 8.6: Thermal conductivity of MLG-polymer TIMs as a function of loading calculated for different values of TBR at the MLG/matrix interface. Fitting of the theoretical curves to the experimental data was used for extraction of the actual values of TBR. Reprinted with permission from K M F Shahil and A. A. Balandin, "Graphene – Multilayer Graphene Nanocomposites as Highly Efficient Thermal Interface Materials", *Nano Letters*, DOI: 10.1021/nl203906r © 2012, American Chemical Society.

In addition to the geometrical factors, the reduction of TBR at the filler/matrix interface is another key condition for achieving high TCE for graphene-MGL nanocomposite.

We further extended our analysis by simulating TCE as a function of TBR at different loading fractions. In figure 8.7 TCE as a function of TBR at different % vol.

fraction is shown. For comparison various reported TBR value of other nanocomposite filler material is shown in the same figure. As can be evidenced from the figure, our extracted TBR value is almost same for different % vol. fraction. That indicates the homogeneity of the MLG filler material with the base matrix.

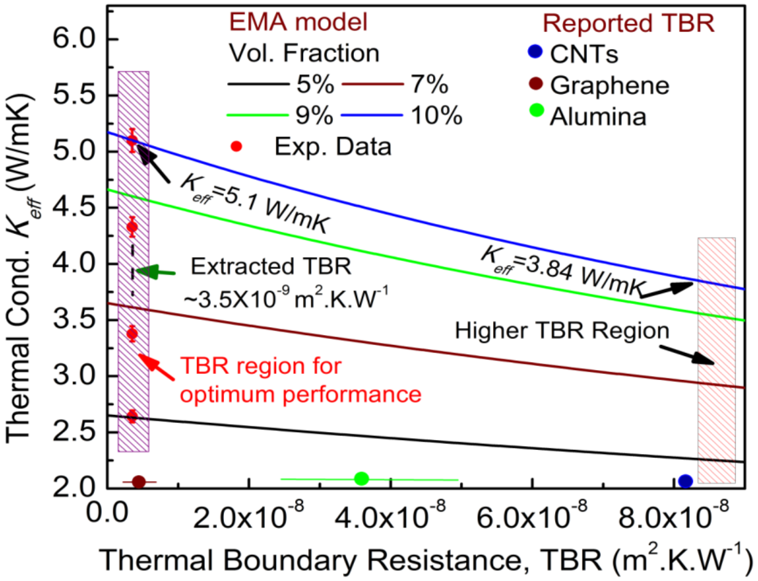

Figure 8.7: Thermal conductivity of MLG-polymer TIMs as a function of TBR calculated for different loading fraction at the MLG/matrix interface. Fitting of the theoretical curves to the experimental data was used for extraction of the actual values of TBR.

Recent ab initio density function theory (DFT) and MD study [34] suggested a possibility of extraordinary K enhancement in ordered graphene composites (K/Km≈360 at f≈5%) due to graphene’s planar geometry and strong coupling of the functionalized graphene to the organic molecules with the corresponding decrease in Kapitza resistance. This implies that certain phonon modes excited in graphene and couple well to those in organic molecules and the mismatch in the phonon DOS between graphene – matrix is smaller than between CNT/matrix. Our experimental results are in line with these DFT and MD predictions [33-34].

Several researchers reported TBR across graphene and FLG on substrates measured by several different techniques, including electrical 3-omega, Raman-electrical, and optical pump-and-probe methods [35 – 46]. The RT TBR of 5X10^{-8} to 4.7X10^{-9} (Km2/W) was found in most of cases (see Table 8.2). The studies are in agreement that the cross-plane conductance G or thermal boundary resistance (TBR) do not reveal a strong dependence on the thickness of FGL or nature of the dielectric or metal substrate. TBR decreases with T following a typical trend for Kapitza resistance.

A first-principle calculation [40] of heat transfer between graphene and SiO_2, which treated the graphene-substrate coupling as a week van-der-Waals-type interaction, determined the TBR of ~4×10^{-8} (Km^2/W), which is close to experimental data. Konatham et al [33] reported TBR of graphene/Oil interface as 3.7×10^{-9} $m^2K.W^{-1}$. This means that graphene thermal coupling to other materials can depend strongly on the surface roughness, presence or absence of suspended regions in graphene layers, and methods of graphene preparation. Low TBR of graphene with many materials suggests that graphene can find applications in thermal interface materials (TIMs).

Table 8.2: Thermal Boundary Resistance of the nanocomposite – Substrate Interfaces

Interface	**Thermal Resistance (Km^2W^{-1})**	**Method**	**Reference**
CNT/D_2O	8.3×10^{-8}	Picosecond transient absorption	Huxtable et al. [41]
Vertically aligned (VA)-MWCNT arrays	$8\text{-}18\times10^{-6}$	photoacoustic technique	Amama et al [42]
VA-Carbon nanofiber-Cu	0.25×10^{-4}	ASTM D5470	Ngo et al. [43]
VA-Double wall Nanotube (CNT-CNT interface)	3.8×10^{-4}	Infrared	Hu et al [44]
Alumina/ Polymer	2.5×10^{-8} – 5×10^{-8}	3ω method	Putnam et al. [45]
Graphene/SiO_2	$\sim4\times10^{-8}$	Raman/Electrical	Freitag et al. [35]
Graphene/SiO_2	$\sim(0.6\text{-}12)\times10^{-8}$	Electrical	Chen et al. [36]
Graphene/SiO_2	$\sim2\times10^{-8}$	Pump-Probe	Mak et al. [37]
Au/Ti/graphene/SiO_2	$\sim4\times10^{-8}$	Raman/Electrical	Koh et al. [38]
Bulk Graphite/Metal	$\sim(1-3)\times10^{-8}$	Reflectance	Schmidt et al.[39]
Graphene/a-SiO_2	$\sim4\times10^{-8}$	Theory	Persson et al. [40]
Graphene/Oil	$\sim(0.4\text{-}4)\times10^{-8}$	Theory	Konatham et al. [33]
Graphene/Epoxy	$\sim3.5\times10^{-9}$	LF & Theory	Shahil & Balandin [54]

8.5 Further Insight: Electrical Conductivity, Bond Line Thickness and Percolation Threshold

It follows from our analysis that graphene's geometry ($\alpha \rightarrow 0$ in graphene as opposed to $\alpha \rightarrow \infty$ in CNTs) and lower Kapitza resistance are the key factors in achieving outstanding TCE. The role of the percolation threshold is not clear yet. Theory suggests that $f_T \sim 1/\alpha$ [11], which explain the low electrical percolation f_T for CNTs. This can also indicate that for MLG, f_T should be much larger and heat conduction is assisted, instead, by better graphene and MLG thermal coupling to the matrix. The latter conclusion is supported by the extracted value of R_B and theoretical estimates of Kapitza resistance. These considerations do not exclude attachments of graphene and MLG flakes to each other with good thermal links without forming a completely percolated network. In the examined f range our TIM samples remained electrically insulating with the measured electrical resistivity of $\rho \approx 1.4 \times 10^9$ Ω-cm. Often, the large TCE factors are accompanied by increasing electrical conductivity σ, i.e. decreasing ρ (see references in Table 8.1).

In our case, we observed a record-high TEC without a substantial change in ρ in the examined f range. The increase of TEC without decreasing ρ was reported in a few other studies. For example, a substantial enhancement of K in the composites with CNTs at 1 wt. % loading was reported in Ref. [25]. The electrical conductivity σ of the composites remained low 10^{-11} – 10^{-9} Scm^{-1} in these samples. The low σ of 10^{-15} – 10^{-9} Scm^{-1} in the SWNT/PS composites with enhanced K was also reported [46]. Moreover, there were studies where the increasing K was accompanied by the decreasing σ in the composite with the same filler fraction [47]. The increase in K without substantial change in σ, observed in our experiments, can be explained by the following. The strong increase in the electrical conductivity in the composite with the electrically insulating matrix requires formation of the percolation network. In our case, we have enhancement of K owing to the present of graphene-MLG fillers, perhaps with partial ordering, while the complete percolation network is not formed. The heat can be conducted through the matrix while the electrical current cannot. The narrow layers of the epoxy matrix may not present a substantial thermal resistance while blocking the electric current. According to the theory [11, 48], an increase in the thickness of the polymer layer from zero to 10 nm does not affect significantly the heat transport while such an increase in the width of the tunneling barrier for the electrons would effectively eliminate the electrical transport.

From the extensive trial-and-error study, we established that it is essential to have both graphene and MGL in the nanocomposite, i.e. to have the graphene-MLG mixture, for achieving maximum TEC. The single-layer or bilayer graphene have greater flexibility to form the thermal links while K_p in MGL (n>3) is subject to less degradation due to phonon – boundary scattering [13]. The TIM performance, defined by R_{TIM}, depends not only on K but also on BLT [6-7, 49]. We estimated that our samples have $BLT \leq 5$ μm at relevant P. BLT evolution with f follows the equations $BLT \sim \tau_y/P$, with the yield stress given as $\tau_y = A[1/((f/f_m)^{1/3} - 1)^2)$, where A is a constant and f_m *i*s the maximum filler particle volume fraction [5]. Using an approximate BLT and measured TCE of 2300%, we conservatively estimate that R_{TIM} of the nanocomposite graphene-MLG TIMs should be, at least, on the order of magnitude smaller than that of conventional or CNT based TIMs. The achieved TCE at *f*=10% is higher than that in graphite composites [16], GnP – CNT epoxy composites [50-51], graphite nanocomposites [51], or chemically functionalized graphite composites [52] at the same or even higher carbon loading.

8.6 Industry Standard Testing Protocol Verifying the Effectiveness of Graphene Based TIMs

In order to evaluate the effectiveness of graphene-MLG-based TIMs in the practical setting of the two proximate surfaces and TIM between them, we measured the thermal conductivity across the thermal contact. We prepared sandwiches of the two mating surfaces made of aluminum with the TIM in between two surfaces. First, we started with a commercial thermal grease as the TIM material which has Al and ZnO_2 particles as the filler materials [53]. The thermal conductivity of the stacked metal-grease-metal sandwiches was measured using the same laser flash technique. The thermal conductivity of the thermal grease determined in our experiments was ~5.8 W/mK, which compares well with the value provided by the vendor. As the next step, we modified the grease by adding a small quantity (*f*=2 vol. %) of our mixture of graphene-MLG, and prepared several sandwiches of the metal-TIM-metal. The thermal conductivity of the total structure was measured again following the same procedure. The extracted thermal conductivity of our graphene-MLG-grease TIM was found to be ~14 W/mK at RT. This corresponds to K/K_m ratio of ~2.4, i.e. TCE factor of ~1.4, at the very small 2% loading fraction.

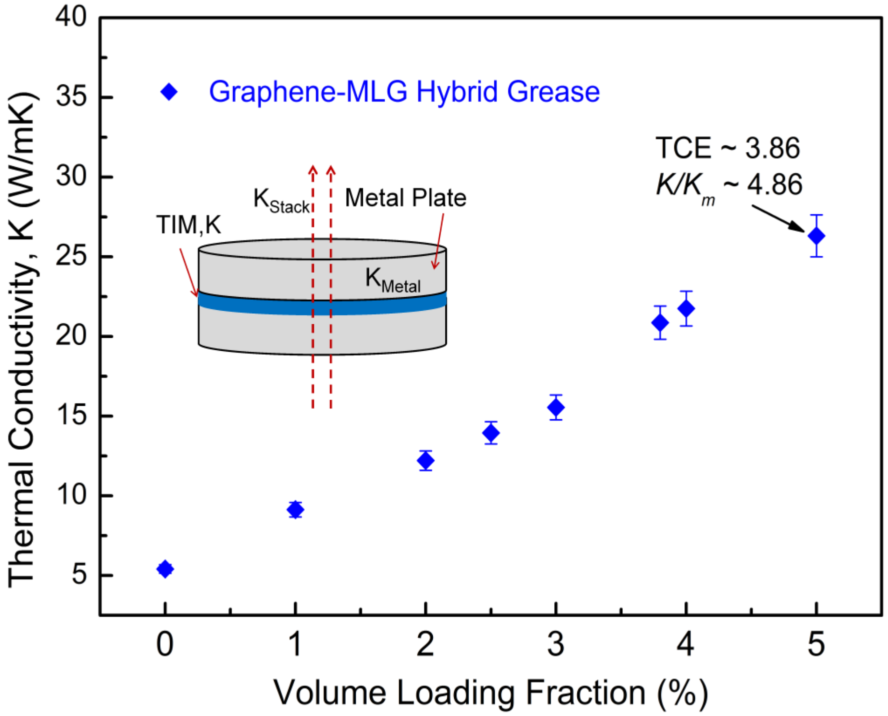

Figure 8.8: Thermal conductivity of graphene-MLG hybrid grease TIMs extracted following an industry standard testing protocol.

We further extended our analysis by preparing the two mating surfaces made of Tin (*Stannum*, Sn) with the TIM in between two surfaces. First, we measured the intrinsic K of Tin as ~65 W/mK. Then we measured the total thermal conductivity (i.e. $K_{stacked}$) of stacked Metal-TIMs-Metal sandwiches with LASER flash instrument. Finally the thermal conductivity of graphene-MLG-grease TIMs (K) was extracted. The extracted K at varying % vol. fraction of graphene-MLG filler is show in figure 8.8. The thermal conductivity of TIM at 5% vol. fraction reaches a value of 26.31 W/mK from a base value of ~5.4 W/mK. This corresponds to K/K_m ratio of ~5. For comparison, in the case of our graphene-MLG-epoxy composite the TCE factor is ~3 at 2 % loading, which corresponds to K/K_m~4 (see Figure 8.3). Although the TCE factor in the tested commercial grease with graphene is smaller than that in the graphene-epoxy composite, it is still significant. It is reasonable to assume that in the commercial grease the TCE factor is smaller than in the graphene-MLG-epoxy nanocomposites owing to the presence of other filler particles (Al and ZnO_2) with the relatively low intrinsic K. A different graphene – matrix coupling can also affect the K value. In the graphene-epoxy composites we also start with the much smaller matrix thermal conductivity K_m. A hybrid mixture of graphene-MLG and Al and ZnO_2 can be efficient filler owing to a complex interactions among different filler particles [9].

It is important to note that by using low (~2-5 %) loading fraction, we kept the viscosity and other important mechanical characteristics, such as conformity and spreadability, of the original thermal grease unaffected. Conformability allows TIM to fill the microscopic valleys on the surface of the mating surfaces, thus displacing air, which is thermally insulating. The spreadability allows one to minimize the TIM thickness: the larger thickness would result in the higher thermal resistance. Implementing this industry testing protocol with the commercial thermal grease, we have demonstrated that graphene-MLG nanocomposite prepared under the optimum conditions are promising as the next generation TIMs.

8.7 Three Dimensional Thermal Simulations

As discussed earlier, the thermal problem for chip cooling is about maintaining the temperature of the "hot spot" below a certain design point. So to investigate how enhanced thermal conductivity of TIM could reduce the hot spot's temperature, we carried out 3D thermal simulation [56] for real packaging structure. The thermal simulations were carried out with the help of the finite element method using COMSOL software. We considered 3-D model of heat conduction and numerically solved the Fourier's law

$$-\nabla \cdot (K \nabla T) = Q, \tag{8.11}$$

Where Q is the heat source, which is defined as the heat energy generated within a unit volume per unit time, T is the absolute temperature and K is the thermal conductivity. The internal boundaries between the components of the circuit were assumed to be thermally continuous. The bottom surface of the heat sink was kept at a constant temperature T_0 = 300 K. Other surfaces were modeled as insulated from environment, i.e. the temperature gradients across these surfaces were set to zeros. In our model we considered several hot spots on a background of uniform heat flux applied to the surface of a silicon chip. The hot spots are each 1 x 1 mm^2 and separated by 3 mm, center to center. The power applied to each hot spot is equal to 4 W. There is a uniform flux applied to the remainder of the chip surface and the total power is 120 W. We studied two types of design criteria:

Design-I is for laptop application which uses single TIM material (Figure 8.9).

The simulation includes the three components in the major heat flow path i.e. Chip => TIM => Heat sink. The component dimensions and the values of thermal conductivity are presented in Table 8.3.

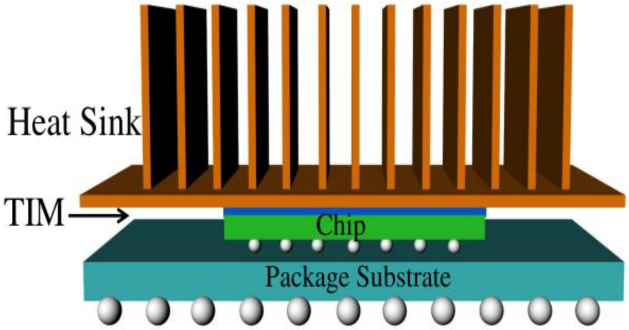

Figure 8.9: Schematic illustration of thermal architecture used for laptop applications.

In the simulation, we considered TIMs as our developed LPE graphene reinforced epoxy composite. Experimentally we extracted that thermal conductivity of this material is within the range of 0.21-5.1 W/mK (see Figure 8.3) as the volume fraction of graphene changes. Figure 8.10 shows the simulated temperature profile of Design-I. The Thermal conductivity of TIM is taken as 5.1 W/mK at room temperature with experimentally determined temperature-dependency.

Table 8.3: Dimensions and thermal conductivity of different components of Design-I.

Layers	**Component**	**Length (mm)**	**Width (mm)**	**Thickness (mm)**	***K* (W/mK)**
1	Chip	20	20	0.6	155
2	TIM	20	20	0.1	0.21-5.1
5	Heat Sink	100	100	5.0	400

The maximum temperature of hot spots as shown in the figure 8.10 is 321.6 K. Surface temperature profile of chip is shown in Figure 8.10.

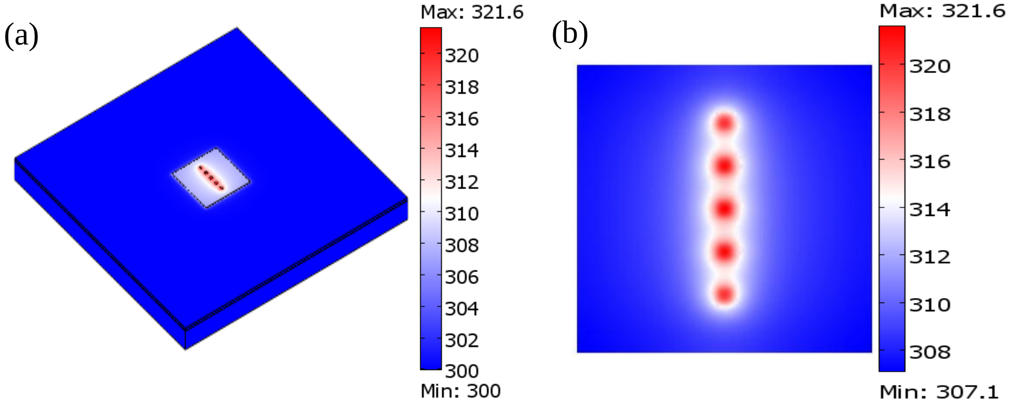

Figure 8.10: (a) Temperature distribution across the silicon chip with five hot spots. The thermal conductivity of TIM is assumed to be 5.1 Wm-1K-1 at room temperature and this value was temperature-dependent. (b) Surface temperature profile/surface plot.

We simulated our model taking different experimentally extracted thermal conductivity value for TIM and the maximum temperature profile is plotted in Figure 8.11. The maximum temperature rise continues to decrease as the volume fraction of graphene increases. For a given parameters of the structure and a number of hot spots the maximum temperature rise in the chip relative to the ambient temperature is reduced by ~49% when graphene is introduced into the epoxy with a volume fraction of 10%.

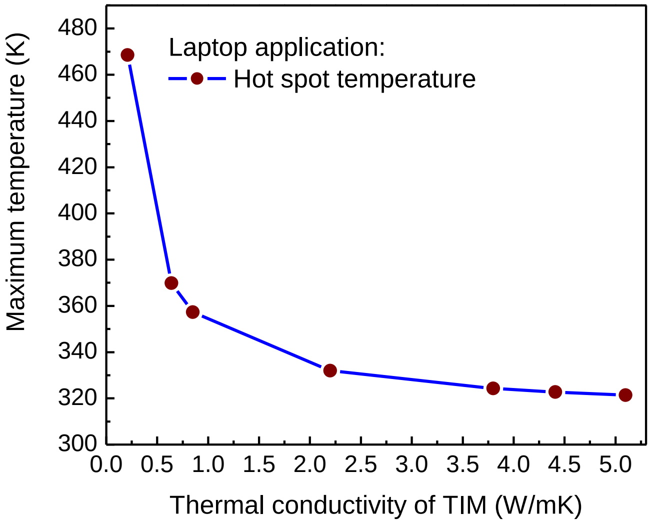

Figure 8.11: Maximum temperature in the silicon chip (Design-I) as a function of the thermal conductivity of TIM.

Design-II is for desktop and server applications, uses both TIM1 and TIM2 (Figure 8.12). The simulation include the five components in the major heat flow path i.e. Chip => TIM1 => Heat Spreader => TIM2 => Heat sink. The component dimensions and the values of thermal conductivity are presented in Table 8.4.

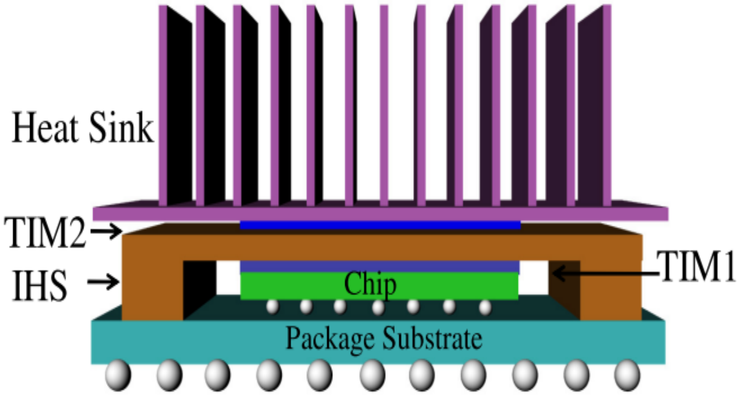

Figure 8.12: Schematic diagram of the structure used as Design-II typically used in desktop and server applications.

We consider TIM2 as commercially used thermal interface material with thermal conductivity of 1-5 W/mK and TIM1 as Graphen reinforced epoxy composite.

Table 8.4: Dimensions and Thermal conductivity of different components of Design-II

Layers	**Component**	**Length (mm)**	**Width (mm)**	**Thickness (mm)**	***K* (W/mK)**
1	Chip	20	20	0.6	155
2	TIM1	20	20	0.1	0.21-5.1
3	Heat Spreader	50	50	2.0	400
4	TIM2	50	50	0.1	1,3
5	Heat Sink	100	100	5.0	400

Figure 8.13 shows the temperature profile for Design-II. The value of thermal conductivity of TIM2 was taken as 3 $Wm^{-1}K^{-1}$ and TIM1 as 5.1 W/mK.

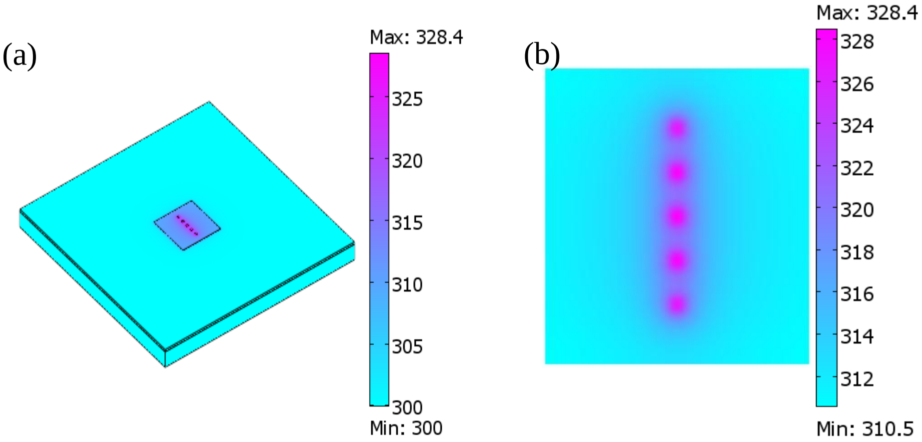

Figure 8.13: (a) Temperature distribution across the silicon chip with five hot spots. The thermal conductivity of TIM1 is assumed to be 5.1 $Wm^{-1}K^{-1}$ at RT and this value was temperature-dependent. The thermal conductivity of TIM2 is 3 $Wm^{-1}K^{-1}$. (b) Surface temperature profile/surface plot showing the hot spot temperature

Surface temperature profile is also shown in Figure 8.13 (b). We simulated maximum temperature of the hot spot as shown in Figure 8.14 with different thermal conductivity of TIM1.

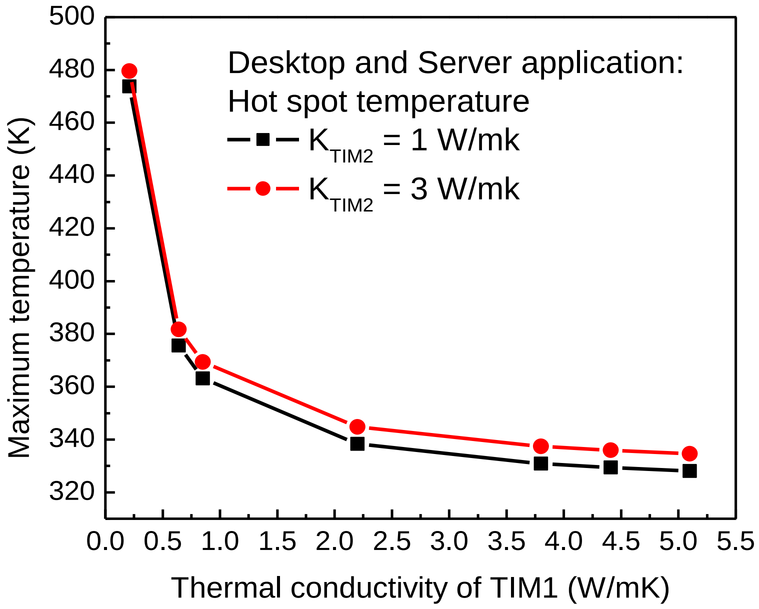

Figure 8.14: Maximum temperature in the silicon chip (Design-II) as a function of the thermal conductivity of TIM1 and TIM2.

Figure 8.14 shows the simulated maximum temperature for Design-II as the function of the values of the thermal conductivity of TIM1 and TIM2. It shows the trend very similar to that observed in the case of the Design-I for a particular TIM2 material. The maximum temperature decreases with the increase of the value of thermal conductivity of TIM2 for a certain TIM1 material.

8.8 Summary

In conclusion, we synthesized graphene-MLG nanocomposite polymer TIMs and demonstrated the extremely high TCE factors at low filler loadings [54, 55]. The TIM testing has been conducted in the industry-type settings ensuring that all other TIM characteristics are in acceptable range for TIMs' practical applications. The TCE of 2300% at f=10% loading is higher than anything reported to-date. We explained the unusual enhancement by (i) high intrinsic K_i of graphene and MLG, (ii) low Kapitza resistance at the graphene/matrix interface; (iii) geometrical shape of graphene/MLG flakes ($a \rightarrow 0$); (iv) high flexibility if MLG (n<5); and (v) optimum mix of graphene and MGL with different thickness and lateral size. Additional benefits of the graphene-based composites, which come at now additional expense, are their low coefficient of thermal expansion and increased mechanical strength. We have also demonstrated a possibility of achieving K~14 W/mK in the commercial thermal grease via addition of only f=2% of the optimized graphene-MLG nanocomposite mixture. The graphene-based TIMs have thermal boundary resistance (TBR) reduced by orders-of-magnitude and be can produced inexpensively on an industrial scale, thus, allowing for the first graphene application, which consumes this material in large quantities. The computer simulations of thermal properties of TIM composites carried out using the modified effective medium approximation which shows that graphene can outperform CNT due to low TBR. Finally, 3D thermal simulation studies are carried out with the finite-element method (FEM) with in silicon chip structure. For a given parameters of the structure and a number of hot spots, the maximum temperature rise in the chip relative to the ambient temperature is reduced by ~43.33% when graphene is introduced into the epoxy with a volume fraction of 10%.

References

[1] A. Kearney, L. Li and S. Sanford, *IEEE SEMI-THERM Symposium*, **25** 293, San jose, CA, USA, March (2009).

[2] T. Ramanathan, A. A. Abdala, S. Stankovich, D. A. Dikin, M. Herrera-Alonso, R. D. Piner, D. H. Adamson, H. C. Schniepp, X. Chen, R. S. Ruoff, S. T. Nguyen, I. A. Aksay, R. K. Prud'homme and L. C. Brinson, *Nat. Nanotechnol*. **3**, 327 (2008).

[3] I. Calizo, I. Bejenari, M. Rahman, G. Liu & A. A. Balandin, *J. Appl. Phys.* **106**, 043509 (2009).

[4] I. Calizo, A. A. Balandin, W. Bao, F. Miao and C. N. Lau, *Nano Letters* 7, 9, 2645 (2007); I. Calizo, F. Miao, W. Bao, C.N. Lau and A.A. Balandin, *Appl. Phys. Lett*., **91**, 071913 (2007).

[5] S. V. Garimella, A. S. Fleischer, J. Y. Murthy, A. Keshavarzi, R .Prasher, C. Patel, S. H. Bhavnani, R. Venkatasubramanian, R. Mahajan, Y. Joshi, B. Sammakia, B. A. Myers, L. Chorosinski, M. Baelmans, P. Sathyamurthy and P. E. Raad, *IEEE Transactions on Components and Packaging Technologies* **31**, 801 – 815 (2008).

[6] R. Prasher, *Proceedings of IEEE* **94**, 1571 – 1585 (2006).

[7] F. Sarvar, D. C. Whalley and P. P. Conway, *Proceeds. Electronics System Integration Technology Conference* (IEEE 1-4244-0553) **2**, 1292-1302 (2006).

[8] R. S. Prasher, J. Y. Chang, I. Sauciuc, S. Narasimhan, D. Chau, G. Chrysler, A. Myers, S. Prstic and C. Hu, *Intel Technology Journal* **9**, 285 – 296 (2005).

[9] J. Felba, Thermally conductive nanocomposites, in *Nano-Bio-Electronic, Photonic and MEMS Packaging* (Springer Science, 2010; DOI 10.1007/978), Editors C.P. Wong, K.-S. Moon and Y. Li, 277 – 314 (2010).

[10] P. Bonnet, D. Sireude, B. Garnier and O. Chauvet, *Appl. Phys. Lett.* **91**, 201910 (2007).

[11] N. Shenogina, S. Shenogin, L. Xue and P. Keblinski, *Appl. Phys. Lett.* **87**, 133106 (2005).

[12] S. Stankovich, D. A. Dikin, G H. B. Dommett, K. M. Kohlhaas, E. J. Zimney, E. A. Stach, R. D. Piner, S. T. Nguyen, and R. S. Ruoff, *Nature* **442**, 282-286 (2006).

[13] A. A. Balandin, *Nature Mat.* **10**, 569 - 581 (2011).

[14] A. Yu, M. E. Itkis, E. Bekyarova and R. C. Haddon, *Appl. Phys. Lett.* **89**, 133102 (2006).

[15] S. U. S. Choi, Z. G. Zhang, W. Yu, F. E. Lockwood and E. A. Grulke, *Appl. Phys. Lett.* **79**, 2252 (2001).

[16] B. Debelak and K. Lafdi, *Carbon,* **45**, 1727 (2007).

[17] M. T. Hung, O. Choi, Y. S. Ju and H. T. Hahn, *Appl. Phys. Lett*. **89**, 023117(2006).

[18] M. J. Biercuk, M. C. Llaguno, M. Radosavljevic, J. K. Hyun, A. T. Johnson and E. J. Fischer, *Appl. Phys. Lett*. **80**, 2767 (2002).

[19] C. H. Liu, H. Huang, Y. Wu and S. S. Fan, *Appl. Phys. Lett*. **84**, 4248 (2004).

[20] A. Yu, P. Ramesh, M. E. Itkis, E. Bekyarova, and R. C. Haddon, *J. Phys. Chem. Lett*. **111**, 7565 (2007).

[21] W. Yu, H. Xie and W. Chen, *J. Appl. Phys*. **107**, 094317 (2010).

[22] S. Nikkeshi, M. Kudo and T. Masuko, *J. Appl. Pol. Science* **69**, 2593 (1998).

[23] M. Ohashi, S. Kawakami, Y. Yokogawa and G. C. Lai, *J. Amer. Ceramic Soc*. **88**, 2615 (2005).

[24] M. J. Hodgin and R. H. Estes, *Proceedings of the National Electronic Packaging and Production Conference* **1**, 359 (1999).

[25] M. B. Jakubinek, M. A. White, M. Mu and K. I. Winey, *Appl. Phys. Lett*. **96**, 083105 (2010).

[26] L. Rayleigh, *Philos. Mag.* **34**, 481 (1892).

[27] J. C. Maxwell, A Treatise on Electricity and Magnetism, Clarendon, Oxford, Vol. 1, (1904)

[28] C.W. Nan, R. Birringer, D. R. Clarke and H. Gleiter, *J. Appl. Phys.* **81**, 6692 (1997).

[29] S. H. Xie, Y. Y. Liu, and J. Y. Li, *Appl. Phys. Lett.* **92**, 243121 (2008).

[30] D. P. H. Hasselman and L. F. Johnson, *J. Compos. Mater.* **21**, 508 (1987).

[31] A. Minnicha and G. Chen, *Appl. Phys. Lett.* **91**, 073105 (2007).

[32] S. Huxtable, D. G. Cahill, S. Shenogin, L. Xue, R. Ozisik, P. Barone, M. Usrey, M. S. Strano, G. Siddons, M. Shim, and P. Keblinski, *Nat. Mater.* **2**, 731 (2003).

[33] D. Konatham and A. Striolo, *Appl. Phys. Lett*. **95**, 163105 (2009).

[34] D. Konatham, K. N. D. Bui, D. V. Papavassiliou &, A. Striolo, *Molecular Physics* **109**, 1, 97 – 111 (2011).

[35] M. Freitag, M. Steiner, Y. Martin, V. Perebeinos, Z. Chen, J. C. Tsang and P. Avouris, *Nano Lett.* **9**, 1883 – 1888 (2009).

[36] Z. Chen, W. Jang, W. Bao, C. N. Lau and C. Dames, *Appl. Phys. Lett.* **95**, 161910-3 (2009).

[37] K. F. Mak, C. H. Liu and T. F. Heinz, Thermal conductance at the graphene-SiO_2 interface measured by optical pump-probe spectroscopy. arXiv:1009.0231, 1-10 (2010).

[38] Y. K. Koh, M. H. Bae, D. G. Cahill and E. Pop, *Nano Lett.* **10**, 4363-4368 (2010).

[39] A. J. Schmidt, K. C. Collins, A. J. Minnich and G. Chen, *J. Appl. Phys.* **107**, 104907-5 (2010).

[40] B. N. J. Persson and H. Ueba, *Europhysics Lett.* **91**, 56001-5 (2010).

[41] S. Huxtable, D. G. Cahill, S. Shenogin, L. Xue, R. Ozisik, P. Barone, M. Usrey, M. S. Strano, G. Siddons, M. Shim and P. Keblinski, *Nat. Mater.* **2**, 731 - 734 (2003).

[42] P. B Amama, B. A Cola, T. D Sands, X. Xu and T. S Fishe, *Nanotechnology* **18**(38), 385303 (2007).

[43] Q. Ngo, B. A. Cruden, A. M. Cassell, G. Sims, M. Meyyappan, J. Li, and C. Y. Yang, *Nano Lett.* **4**(12), 2403-2407 (2004).

[44] X. J. Hu, M. A. Panzer and K.E. Goodson, *Journal of Heat Transfer* **129** (1), 91(2007).

[45] S. A. Putnam, D. G. Cahill, B. J. Ash, and L. S. Schadler, *J. Appl. Phys.* **94**, 10, 6785–6788 (2003).

[46] M. N. Tchoul, W.T. Ford, M. L. P. Ha, I. C. Sumarriva, B. P. Grady, G. Lolli, D. E. Resasco and S. Arepalli, *Chem. Mater*., **20**, 3120 (2008).

[47] A. Yu, P. Ramesh, X. Sun, E. Bekyarova, M. E. Itkis, & R. C. Haddon, *Adv. Mater*. **20**, 4740 (2008).

[48] S. Shenogin, L. P. Xue, R. Ozisik, P. Keblinski, and D. G. Cahill, *J. Appl. Phys.* **95**, 8136 (2004).

[49] J. Liu, B. Michel, M. Rencz, C. Tantolin, C. Sarno, R. Miessner, K.V. Schuett, X. T. S. Demoustier, A. Ziaei, *EDA Publishing/Therminic* (2008).

[50] C. Lin and D. D. L. Chung, *Carbon* **47**, 295 (2009).

[51] H. Fukushima, L.T. Drzal, B. P. Rook and M. J. Rich, *Thermal Analysis and Calorimetry* **85**, 235 (2006).

[52] S. Gangui, A. K. Roy and D. P. Anderson, *Carbon* **46**, 806 (2008).

[53] S. Narumanchi, M. Mihalic, K. Kelly and G. Eesley, *Itherm-2008,* NREL/CP-540-42972, Florida, USA, May (2008).

[54] K. M. F. Shahil and A. A. Balandin, *Nano Letters, DOI: 10.1021/nl203906r* (2012).

[55] K. M. F. Shahil, V. Goyal, and A. A. Balandin, *ECS Trans.* **35**, 193–195 (2011).

[56] K. M. F. Shahil, S. Subrina and A. A. Balandin, (in preparation) (2012)

Chapter 9

Conclusions

9.1 Summary of Dissertation

In conclusion, properties and applications of two representative nanostructured 2D materials are presented in this study. In the first part, we presented results of the detail Raman studies of the few-quintuple-thick films of Bi_2Te_3, Bi_2Se_3 and Sb_2Te_3. The films were prepared by the "graphene-like" mechanical exfoliation from bulk crystals. We have shown how resonant Raman scattering by LO phonons can be used to analyze FQL Bi_2Te_3 and Bi_2Se_3 films. Tuning the incident photon energy into resonance with appropriate band gap energy allows the vibrational properties of that particular layer to be probed with a high degree of selectivity. The activation of non-Raman active IR mode found in relatively thin Bi_2Te_3 film is informative and could be used to identify few-quintuple films of high quality. The obtained results are important for further development of the topological insulator field. In the second part detailed experimental demonstration of thermal conductivity enhancement with Graphene based TIMs is presented. We synthesized graphene-MLG hybrid polymer TIMs and demonstrated a possibility of achieving extremely high TCE factors at low filler loadings while keeping all other TIM characteristics in acceptable range for practical applications. The TCE of 2300% at f=10% loading is higher than anything reported to-date. We explained the unusual enhancement by (i) high intrinsic Ki of graphene and MLG, (ii) low Kapitza resistance at the graphene/matrix interface; (iii) geometrical shape of graphene/MLG flakes (a→0); (iv) high flexibility if MLG (n<5); and (v) optimum mix of graphene and MGL with different thickness and lateral size. It is expected that by starting with the matrix, which has higher Km than the epoxy used in this study, one can get K of TIMs larger than ~30 W/mK. Additional benefits of the graphene-based composites, which come at now additional expense, are their low coefficient of thermal expansion and increased mechanical strength.

9.2 Peer-reviewed Journal Papers Published from the Dissertation Research

1. K. M. F. Shahil and A. A. Balandin, "Graphene – Multilayer Graphene Nanocomposites as the Highly Efficient Thermal Interface Materials", *Nano Letters*, Nano Lett. **12**, 861 − 867 (2012).

2. K. M. F. Shahil, M. Z. Hossain, V. Goyal and A. A. Balandin, "Micro-Raman Spectroscopy of Mechanically Exfoliated Few-Quintuple Layers of Bi_2Te_3, Bi_2Se_3 and Sb_2Te_3 Materials" *Journal of Applied Physics (JAP) . (Accepted)*, (2012).

3. K. M. F. Shahil, M. Z. Hossain, D. Teweldebrhan and A. A. Balandin, "Crystal Symmetry Breaking in Few-Quintuple Bi_2Te_3 Films: Applications in Nanometrology of Topological Insulators" *Applied Physics let. (APL)* **96**, 16, (2010).

4. K. M. F. Shahil, Vivek Goyal and A. A. Balandin, "Thermal Properties of Graphene: Applications in Thermal Interface Materials", *ECS Transactions (ECST)* **35** (3) 193-199 (2011).

5. M. Z. Hossain, S L. Rumyantsev, K. M. F. Shahil, D. Teweldebrhan, M. Shur and A. A. Balandin, "Low-Frequency Current Fluctuations in "Graphene-Like" Exfoliated Thin-Films of Bismuth Selenide Topological Insulators" *ACS Nano* **5**, 2657 (2011).

6. M. Z. Hossain, S. L. Rumyantsev, D. Teweldebrhan, K. M. F. Shahil, M. Shur and A. A. Balandin, "1/f Noise in Conducting Channels of Topological Insulator Materials", *Physica Status Solidi A* **1**, 144, 2010.

7. K. M. F. Shahil, S. Subrina and A. A. Balandin, *IEEE Transactions on Nanotechnology* (manuscript in preparation) (2012).

9.3 Conference Proceedings/Presentation from the Dissertation Research

8. K. M. F. Shahil, M. Z. Hossain, D. Teweldebrhan and A. A. Balandin, "Crystal Symmetry Breaking in Few-Quintuple Layers of Bi_2Te_3, Bi_2Se_3 and Sb_2Te_3: Applications in Nanometrology of Topological Insulators", *International Symposium on Advanced Nanodevices and Nanotechnology (ISANN 2011)*, Kaanapali, Hawaii, December (2011).
   (*Oral Presentation)

9. K. M. F. Shahil and A. A. Balandin, "Graphene-Based Thermal Interface Materials", *IEEE Int. conference on nanotechnology (IEEE-NANO 2011)* **11,** Portland, Oregon, USA, August (2011)
   (*Paper and Oral Presentation)

10. M. Z. Hossain, K. M. F. Shahil, D. Teweldebrhan, A. A. Balandin, S. L. Rumyantsev and M. Shur, "Low-Frequency 1/f Noise in Bismuth Selenide Topological Insulators", *International Conference on Noise and Fluctuations (ICNF 2011)* **21**, Toronto, Canada, June (2011).
    (*Oral Presentation)

11. K. M. F. Shahil, S. Subrina and A. A. Balandin "Graphene Thermal Interface Materials with Strongly Enhanced Heat conduction Properties," *Graphene: The Road to Applications, Nature conference* **1**, Cambridge, MA, USA, May (2011).
    (Poster presentation)

12. M. Z. Hossain, S. L. Rumayantsev, K. M. F. Shahil, D. Teweldebrhan, M. Shur and A. A. Balandin, "Low-Frequency Current Fluctuations in "Graphene-Like"Exfoliated Thin Films of Topological Insulators", *The FENA/MSD Annual Review,* Boston, MA, USA, May (2011).
    (*Best poster award)

13. K. M. F. Shahil, M. Z. Hossain, D. Teweldebrhan and A. A. Balandin “Crystal Symmetry Breaking in Bi_2Te_3, Bi_2Se_3 and Related Thin Films: Applications in Raman Nanometrology of Topological Insulators,” *MRS Spring meeting*, Symposium Y, San Francisco, USA, April (2011).
(*Oral Presentation)

14. V. Goyal, D. Teweldebrhan, K. M. F. Shahil, M. Z. Hossain and A.A. Balandin, “Mechanically-Exfoliated Stacks of Thin Films of Bi_2Te_3 Topological Insulators with Enhanced Thermoelectric Performance”, *Conference on the Physics and Chemistry of Surfaces and Interfaces* **38**, San Diego, California, USA, January (2011).
(*Oral presentation & Poster)

15. K. M. F. Shahil, M. Z. Hossain, D. Teweldebrhan and A. A. Balandin, “Spectroscopic Raman Nanometrology of the Atomically-Thin Crystalline Bi_2Te_3 and Bi_2Se_3 Films”, *TECHCON*, Austin, TX, USA, September (2010).
(*Oral presentation & Poster)

16. D. Teweldebrhan, V. Goyal, M. Z. Hossain, K. M. F. Shahil, M. Rahman and A. Balandin, “Graphene-Like” Exfoliation of Quasi-2D Crystals of Bismuth Telluride: Applications in Thermoelectrics and Topological Insulators” *TECHCON*, Austin, TX. USA September (2010).
(*Oral presentation & Poster)

17. M. Rahman, I. Bejenari, D. Kotchetkov, V. Goyal, M. Z. Hossain, C. Nolen, K. M. F. Shahil and A. A. Balandin “Mobility in Silicon and Poly-Silicon Channels Embedded within Acoustically Hard Polycrystalline Diamond Barriers” *FENA Annual Review* **5**, Los Angeles, CA, March (2009).
(*Poster)

9.4 Invited Talk/Presentation

18. K. M. F. Shahil, M. Z. Hossain and Alexander Balandin, “Micro-Raman and Low-Frequency Noise Spectroscopy of Mechanically Exfoliated Thin Films of Topological Insulators of Bi_2Te_3 Family”, *Material Research Society (MRS) Fall Meeting & Exhibit*, Boston, MA. USA. Nov. (2011).
(*Presented Talk on behalf of Prof. A. Balandin)

19. K. M. F. Shahil and A. A. Balandin “*Phonon Transport in Graphene and Topological Insulator Thin Films*”, Material Research Society (MRS) Fall Meeting & Exhibit, Boston, MA. USA. Nov. (2011).
(*Presented Talk on behalf of Prof. A. Balandin)

20. K. M. F. Shahil, S. Subrina and A. A. Balandin, “Graphene Based Thermal Interface Materials for the Next Generation Electronics”, *International Nanotechnology Conference on Communication and Cooperation (INC)* **7**, Albany, New York, USA May (2011).
(*Invited poster)